ESIC
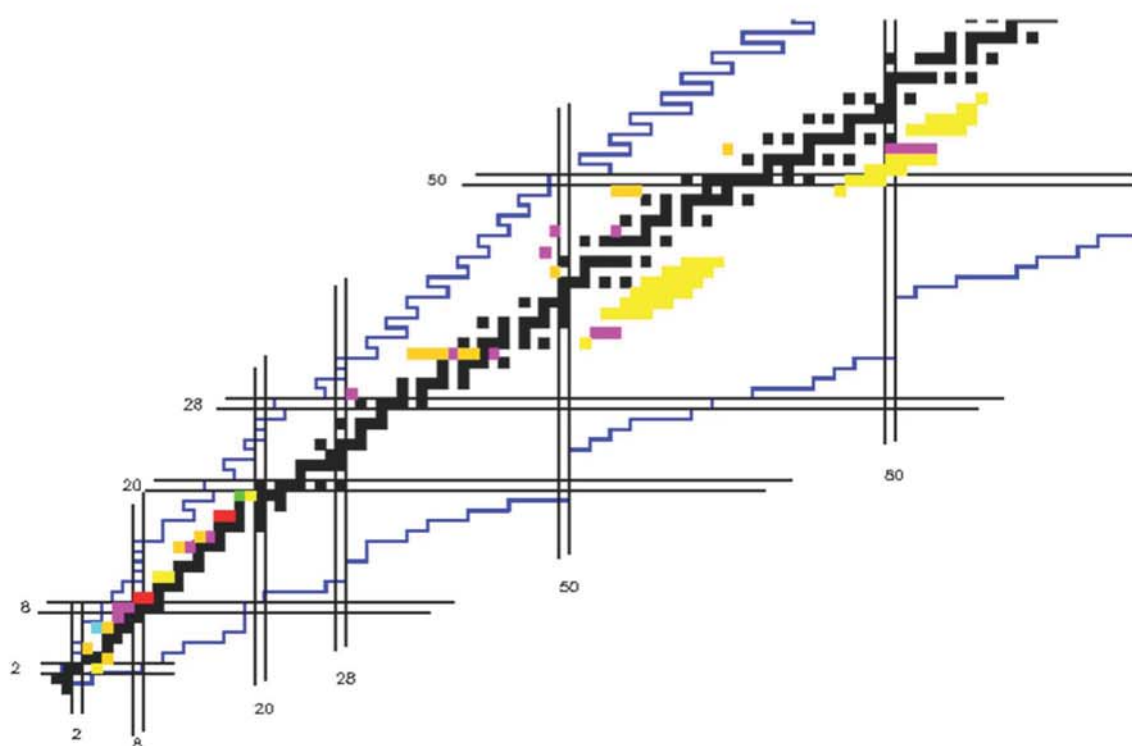
Annual Report
2011

Elements Synthesis in Cosmos

创新研究群体

esic.ciae.ac.cn

CONTENTS

Determination of the astrophysical S(E) factors or rates for radiative capture reaction with one nucleon transfer reaction

LI ZhiHong (李志宏), GUO Bing (郭冰), LI YunJu (李云居), SU Jun (苏俊), LI ErTao (李二涛), BAI XiXiang (白希祥), WANG YouBao (王友宝), ZENG Sheng (曾晟), WANG BaoXiang (王宝祥), YAN ShengQuan (颜胜权), LI ZhiChang (李志常), LIU JianCheng (刘建成), LIAN Gang (连钢), JIN SunJun (金孙均), LIU Xin (刘鑫) & LIU WeiPing (柳卫平)

China Institute of Atomic Energy, Beijing 102413, China

(To be submitted)

The radiative capture reactions plays an important role in nuclear astrophysics. We have indirectly measured the astrophysical S(E) factors for some proton capture reactions and the reaction rates for several neutron capture reactions with one nucleon transfer reactions at HI-13 tandem accelerator in recent years. Some of them are compiled into NNDC EXFOR database and JINA REACLIB project, and used in the network calculations of Big Bang nucleosynthesis and type-I X-ray bursts.

Keywords: Nucleosynthesis, transfer reaction, spectroscopic factor, radiative capture.

PACS: 26.30.+k, 25.70.Hi, 21.10.Jx, 25.40.Lw

1 Introduction

The main aim on the field of nuclear astrophysics is to understand the production of energy and the synthesis of elements in stars and during stellar events [1]. The abundances of the elements and isotopes provide important information about the astrophysical environments where they were created. In the laboratory, we can measure the nuclear reactions responsible for producing a particular atomic nucleus within a certain stellar environment. This information, combined with astronomical observations, allows us to describe the first epoch of nucleosynthesis during the big bang, the major burning stages in the life of a star, the evolution of stellar populations, and the evolution of the Galaxy as a whole.

Researches in nuclear astrophysics are complicated since the nuclear reaction network during the explosive phase contains about thousands of isotopes. The determination of reaction rates and the half life of unstable isotopes is the fundamental work in the study of nuclear astrophysics. On the aspect of the nuclear reactions, the radiative capture reactions play a crucial role in many cosmic phenomena [2, 3, 4], e.g. primordial nucleosynthesis, galactic evolution, star and planet formation etc. In many case, it is very difficult to measure the cross section directly since the low interaction energy of astrophysical interests, and the low intensity of the radioactive ion beams. The direct measurement of the neutron capture reactions on the short-lived target is impossible because no neutron target exists, and the half-life of short-lived nucleus is too short to serve as a target. Therefore, a number of indirect methods are being explored by experimental nuclear physicists to avoid difficulties of direct measurements of radiative capture cross sections. A practicable method is to extract the radiative capture cross section using the direct capture model and the spectroscopic factor, which can be deduced from the angular distribution of one nucleon transfer reaction.

The angular distribution of $^{13}C(^7Li,^8Li)^{12}C$ is measured and used to extract the ^8Li neutron spectroscopic factor with Distorted-Wave Born Approximation (DWBA) analysis. The $^7Li(n,\gamma)^8Li$ cross sections are then deduced and compared with the experimental data to demonstrate the feasibility of the indirect method. The indirect measurement of several nucleon capture reactions on the radioactive targets are reviewed in the present article.

2 Indirect methods of determining the radiative capture reactions

The direct capture cross section for the desired reaction, $A(a,\gamma)B$, is determined by the traditional direct capture model [2, 5]. The cross section for the $E1$ transition can be computed by

$$\sigma_{a,\gamma} = \frac{16\pi}{9}\left(\frac{E_\gamma}{\hbar c}\right)^3 \frac{e_{eff}^2}{k^2} \frac{(2J_B+1)}{(2J_A+1)(2J_a+1)} \frac{S_B}{\hbar v} \times \left| \int_0^\infty rdr\phi_i(kr)W_f(2\kappa r) \right|^2, \quad (1)$$

where $\phi_i(kr)$ is the scattering function associated with the $a + A$ channel, $W_f(2\kappa r)$ is the single particle wave function

of particle a in the bound state. The cross section can be calculated once the spectroscopic factor S_B is determined. This can be accomplished by measuring the cross section for a peripheral transfer reaction $A(c, b)B$, with $c = a + b$ and $B = a + A$. The spectroscopic factor can be extracted by

$$\left(\frac{d\sigma}{d\Omega}(\theta)\right)_{EXP} = S_c S_B \left(\frac{d\sigma}{d\Omega}(\theta)\right)_{DWBA}, \quad (2)$$

where $(\frac{d\sigma}{d\Omega})_{EXP}$ and $(\frac{d\sigma}{d\Omega})_{DWBA}$ are the experimental and calculated differential cross section of the $A(c, b)B$ transfer reaction, respectively.

The astrophysical $S(E)$ factor for the $A(a, \gamma)B$ reaction can be calculated with

$$S(E) = E\sigma(E)\exp(2\pi\eta), \quad (3)$$

where η is the Sommerfeld parameter given by

$$\eta = \frac{Z_a Z_A e^2}{\hbar v}. \quad (4)$$

The reaction rate is expressed in terms of the astrophysical $S(E)$ factor as

$$\langle \sigma v \rangle = \frac{(8/\pi)^{1/2}}{\mu^{1/2}(kT)^{3/2}} \int S(E)\exp\left(-\frac{E}{kT} - 2\pi\eta\right)dE. \quad (5)$$

The spectroscopic factors for mirror pairs are equal to each other. If one is extracted, the other one is also known. The relationship of the nuclear asymptotic normalization coefficient (ANC) for the mirror systems has been established [6] as

$$C_p = \left|\frac{F_l(ik_pR_N)}{k_pR_N j_l(ik_nR_N)}\right| C_n, \quad (6)$$

where F_l and j_l are the regular Coulomb wave function and the Bessel function, respectively. k_p and k_n are the wave numbers of proton and neutron determined with their separation energies. Usually, the radius R_N is calculated with $1.3A^{1/3}$. The nuclear ANC is related to the spectroscopic factor by

$$C_{lj} = \sqrt{S_{lj}} b_{lj}, \quad (7)$$

where b_{lj} represent the single particle ANC which can be calculated with optical potential models. Once the spectroscopic factor or ANC is extracted with one nucleon transfer reaction, the cross sections for the proton or neutron capture reactions, (p, γ) or (n, γ), can then be computed with the radiative capture model.

3   An example for the ^{7}Li$(n, \gamma)^8$Li reaction

We have measured the angular distributions of ^{13}C(^{7}Li, ^{8}Li)^{12}C one neutron transfer reaction and ^{13}C + ^{7}Li and ^{12}C + ^{7}Li elastic scattering. The optical potential parameters are derived by fitting the angular distributions of the elastic scattering reactions. The fitted plot for ^{13}C + ^{7}Li differential cross section is shown in Fig. 1. The derived potential

parameters are then used in the angular distribution calculation of one nucleon transfer reaction. The experimental data and the normalized calculation results are shown in Fig. 2. The ratio of the contributions by the $1p_{1/2}$ and $1p_{3/2}$ orbits was determined to be 0.10(3) and the neutron spectroscopic factor of ^{8}Li was extracted to be 0.55 ± 0.06. The spectroscopic factor was then used to deduce the cross section of the ^{7}Li$(n, \gamma)^8$Li reaction. As can be seen in Fig. 3, our indirect measurement is in good agreement with the direct experimental data [7, 8].

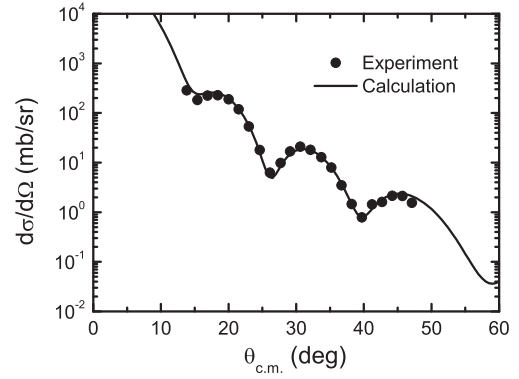Figure 1: The differential cross sections of ^{13}C(^{7}Li, ^{7}Li)^{13}C elastic scattering.
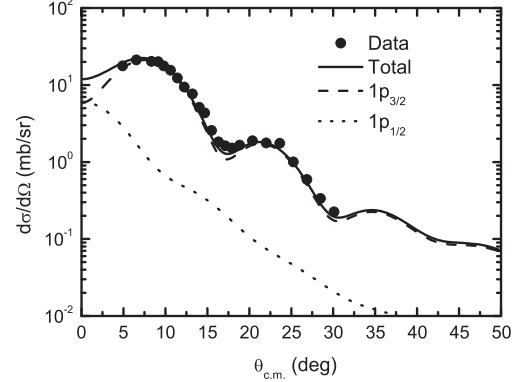
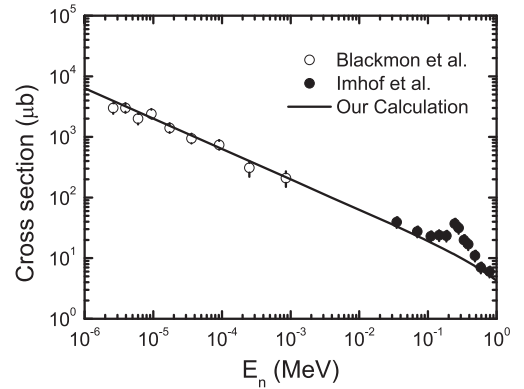Figure 2: The angular distribution of ^{13}C(^{7}Li, ^{8}Li)^{12}C reaction.

Figure 3: The cross section of ^{7}Li$(n, \gamma)^8$Li reaction as a function

of incident neutron energy. The experimental data are taken from Refs. [7] and [8].

^{8}Li and ^{8}B are mirror pairs, thus the proton spectroscopic factor of ^{8}B $= ^7$Be $\otimes p$ is equal to the neutron spectroscopic factor of ^{8}Li $= ^7$Li $\otimes n$. The astrophysical $S(E)$ factors of ^{7}Be$(p, \gamma)^8$B can be deduced with the extracted spectroscopic factor. One can see from Fig. 4 that the experimental data [9] are well reproduced with the indirect method.
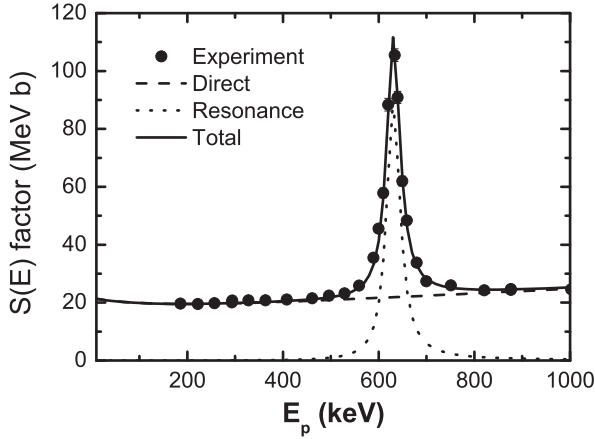

Figure 4: The astrophysical $S(E)$ factor of ^{7}Be$(p, \gamma)^8$B reaction.

4   Other indirect measurements

The ^{8}Li$(n, \gamma)^9$Li reaction plays an important role in both the r-process nucleosynthesis and the inhomogeneous big bang models. Its direct capture rates can be extracted from the ^{8}Li$(d, p)^9$Li reaction, indirectly. We have measured the angular distribution of the ^{8}Li$(d, p)^9$Li$_{g.s.}$ reaction at $E_{c.m.} = 7.8$ MeV in inverse kinematics using coincidence detection of ^{9}Li and the recoil proton. Based on DWBA analysis, the ^{8}Li$(d, p)^9$Li$_{g.s.}$ cross section is determined to be 7.9 ± 2.0 mb. The single particle spectroscopic factor $S_{1,3/2}$ for the ground state of ^{9}Li $= ^8$Li $\otimes$ n is derived to be 0.68 ± 0.14, and then used to calculate the direct capture cross sections for the ^{8}Li$(n, \gamma)^9$Li$_{g.s.}$ reaction at energies of astrophysical interest. The astrophysical ^{8}Li$(n, \gamma)^9$Li$_{g.s.}$ reaction rate for the direct capture is found to be 3970 ± 950 $cm^3 mole^{-1} s^{-1}$ at $T_9 = 1$ [10]. The results have been confirmed by Guimarães et al. [11] from the measurement of the ^{9}Be$(^8$Li,^{9}Li$)^8$Be neutron transfer reaction. According to charge symmetry, (ANC)^2 for ^{9}C $= ^8$B $\otimes p$ is extracted to be 1.14 ± 0.29 fm^{-1}. We have deduced the astrophysical S-factors and reaction rates for direct capture in ^{8}B$(p, \gamma)^9$C at energies of astrophysical relevance [12]. The reaction may play an important role in the evolution of massive stars with very low metallicities.

The squares of the neutron ANC for ^{12}B $= ^{11}$B $\otimes n$ are extracted to be 1.20 ± 0.26, 0.354 ± 0.107 and 1.98 ± 0.35 fm^{-1} from the angular distributions of the ^{11}B$(d, p)^{12}$B reaction leading to the ground, first and second excited states

of ^{12}B respectively, using the Johnson-Soper approach. According to charge symmetry of strong interaction, the square of proton ANC for ^{12}N $= ^{11}$C $\otimes p$ is determined to be 1.63 ± 0.35 fm^{-1} and then utilized to calculate the astrophysical $S(E)$ factor and the rates of the direct capture contribution in the ^{11}C$(p, \gamma)^{12}$N reaction. The astrophysical $S(0)$ factor for the direct capture is derived to be 0.088 ± 0.019 keV b [13]. This result is in agreement with our previous work from the ^{2}H$(^{11}$C, ^{12}N$)n$ proton transfer reaction reaction [14]. An evaluated S(0) of 0.092 ± 0.009 keV b is then given by using the present and pre-existing experimental results. In addition, the proton widths of the first and second excited states of ^{12}N are derived to be 0.91 ± 0.29 and 99 ± 20 keV from the neutron ANCs of ^{12}B and used to compute the contribution from the first two resonances of ^{12}N, respectively. The contribution from the interference effect between the direct capture and the second resonance is then computed. Our result shows that the direct capture dominates the ^{11}C$(p, \gamma)^{12}$N reaction at the temperature range below $T_9 = 0.35$. The ^{11}C$(p, \gamma)^{12}$N reaction is one of the key reactions in the hot pp chains, which is believed to play an crucial role in the evolution of Pop Ⅲ stars.

The astrophysical reaction rates for the ^{12}N$(p, \gamma)^{13}$O direct capture reaction have been estimated at the stellar energies [15] with the spectroscopic factor and ANC of ^{13}O ground state extracted from one proton removal cross section [16]. The result shows that the ^{12}N$(p, \gamma)^{13}$O reaction may play an important role in X-ray bursts. The deduced ^{12}N$(p, \gamma)^{13}$O astrophysical $S(E)$ factor at zero energy is 0.31 keV b, which is about two orders of magnitude less than the only theoretical one (4.0×10^{-2} MeV b) by Wiescher et al. [17]. Our result is confirmed at a later time by Banu et al. [18] from the angular distribution measurement of the ^{14}N$(^{12}$N, ^{13}O$)^{13}$C proton transfer reaction.

^{13}N$(p, \gamma)^{14}$O is one of the key reactions in the hot CNO cycle which occurs at stellar temperatures around $T_9 \geqslant 0.1$. The angular distribution of the ^{13}N$(d, n)^{14}$O reaction at $E_{c.m.} = 8.9$ MeV has been measured in inverse kinematics. Based on the DWBA analysis, the nuclear ANC, $C_{1,1/2}^{14O}$, for the ground state of ^{14}O $= ^{13}$N $\otimes p$ is derived to be 5.42 ± 0.48 fm$^{-1/2}$. The ^{13}N$(p, \gamma)^{14}$O reaction is analyzed with the R-matrix approach, its astrophysical $S(E)$ factors and reaction rates at energies of astrophysical relevance are then determined with the ANC [19]. A similar result is deduced with the mirror system by analyzing the ^{13}C$(d, p)^{14}$C angular distribution [20]. The reaction rates are recommended by JINA REACLIB project [21] and used in the study of cold and hot CNO cycles [22].

The squares of neutron ANC for ^{27}Mg $= ^{26}$Mg $\otimes n$ are extracted to be 44.0 ± 5.3, 3.40 ± 0.32 and 0.90 ± 0.08 fm^{-1} from the angular distributions of the ^{26}Mg$(d, p)^{27}$Mg reaction leading to the ground, first, and second excited states of ^{27}Mg, respectively, based on DWBA analysis. According to charge symmetry of mirror nuclei, the square of proton ANC for ^{27}P $= ^{26}$Si $\otimes p$ is determined to be 1840 ± 240 fm^{-1} and

then utilized to calculate the astrophysical $S(E)$ factor and rate for the direct capture into the ^{27}P ground state. In addition, the proton widths for the first and second excited states in ^{27}P are derived to be $(1.30 \pm 0.12) \times 10^8$ and $(1.79 \pm 0.15) \times 10^5$ MeV from the neutron ANCs and used to compute the contribution of the resonant captures. Furthermore, we have also presented the total astrophysical ^{26}Si$(p, \gamma)^{27}$P reaction rates [23]. The rates are applied in the network calculations of type-I X-ray bursts [21].

5 Summary

The determination of the radiative capture reactions plays a very important role in the study of nuclear astrophysics. We have deduced the reaction rates of several radiative capture reactions with the indirect measurement approach, such as ^{7}Li$(n, \gamma)^8$Li, ^{7}Be$(p, \gamma)^8$B, ^{8}Li$(n, \gamma)^9$Li, ^{8}B$(p, \gamma)^9$C, ^{11}C$(p, \gamma)^{12}$N, ^{13}N$(p, \gamma)^{14}$O, ^{26}Si$(p, \gamma)^{27}$P and so on. These reactions are of importance in big bang nucleosynthesis and stellar evolution. Some of the experimental data have been compiled into NNDC EXFOR database and JINA REACLIB project, and used in the network calculations of type-I X-ray bursts. The calculation results suggest that the previously found small discrepancies between model calculations and observations may be solved with a better understanding of the nuclear input.

More radiative capture reactions, such as ^{6}He$(p, \gamma)^7$Li, ^{8}Li$(p, \gamma)^9$Be, ^{13}C$(p, \gamma)^{14}$N, ^{132}Sn$(n, \gamma)^{133}$Sn, will be determined in the near future. They are very important to investigate the inhomogeneous BBN model, CNO cycle of stellar evolution and nucleosynthesis of r-process.

References

[1]. F. Käppeler, F. -K. Thielemann, M. Wiescher. Annual Review of Nuclear and Particle Science, **48** (1998) 175–251.

[2]. C. Rolfs, Nucl. Phys. A, **217** (1973) 29–70.

[3]. B. C. Diven, J. Terrell and A. Hemmendinger, Phys. Rev. **120** (1960) 556–569.

[4]. A. M. Lane, Nucl. Phys. **11** (1959) 625–645.

[5]. R. F. Christy and I. Duck, Nucl. Phys. A **24** (1961) 89–91.

[6]. N. K. Timofeyuk, R. C. Johnson, A. M. Mukhamedzhanov, Phys. Rev. Lett. **91** (2003) 232501.

[7]. J. C. Blackmon, A. E. Champagne, J. K. Dickens et al. Phys Rev C, **54** (1996) 383–388.

[8]. W. L. Imhof, R. G. Johnson, F. J. Vaughn et al. Phys Rev, **114** (1959) 1037–1039.

[9]. A. R. Junghans, K. A. Snover, E. C. Mohrmann et al. Phys. Rev. C **81** (2010) 012801(R).

[10]. Z. H. Li, W. P. Liu, X. X. Bai et al. Phys. Rev. C **71** (2005) 052801(R).

[11]. V. Guimarães, R. Lichtenthäler, O. Camargo et al. Phys. Rev. C **75** (2007) 054602.

[12]. B. Guo, Z. H. Li, W. P. Liu et al. Nucl. Phys. A **761** (2005) 162–172.

[13]. B. Guo, Z. H. Li, W. P. Liu et al. J. Phys. G: Nucl. Part. Phys. **34** (2007) 103–114.

[14]. W. P. Liu, Z. H. Li, X. X. Bai et al. Nucl. Phys. A **728** (2003) 275–284.

[15]. Z. H. Li, Chin. Phys. Lett. **23** (2006) 3219–3221.

[16]. R. E. Warner, F. Carstoiu, J. A. Brown et al. Phys. Rev. C **74** (2006) 014605.

[17]. M. Wiescher, J. Gorres, S. Graff et al. Astrophys. J. **343** (1989) 353–364.

[18]. A. Banu, T. Al-Abdullah, C. Fu et al. Phys. Rev. C **79** (2009) 025805.

[19]. Z. H. Li, B. Guo, S. Q. Yan et al. Phys. Rev. C **74** (2006) 035801.

[20]. B. Guo and Z. H. Li, Chin. Phys. Lett. **24** (2007) 65–68.

[21]. R. H. Cyburt, A. M. Amthor, R. Ferguson, et al. The Astrophysical Journal Supplement Series, **189** (2010) 240–252.

[22]. M. Wiescher, J. Görres, E. Uberseder et al. Annu. Rev. Nucl. Part. Sci. **60** (2010) 381–404.

[23]. B. Guo, Z. H. Li, X. X. Bai et al. Phys. Rev. C **73** (2006) 048801.

Study of the primordial Lithium abundance

LI ZhiHong (李志宏)[1], LI ErTao (李二涛)[1], SU Jun (苏俊)[1], LI YunJu (李云居)[1], BAI XiXiang (白希祥)[1],
GUO Bing (郭冰)[1], WANG YouBao (王友宝)[1], CHEN YongShou (陈永寿)[1], HOU SuQing (侯素青)[1],
ZENG Sheng (曾晟)[1], LIAN Gang (连钢)[1], SHI JianRong (施建荣)[2] & LIU WeiPing (柳卫平)[1]

[1]*China Institute of Atomic Energy, Beijing 102413, China;*
[2]*National Astronomical Observatories, Chinese Academy of Sciences, Beijing 100012, China*

Lithium isotopes have attracted an intense interest because the abundances of both ^{6}Li and ^{7}Li from big bang nucleosynthesis (BBN) is one of the puzzles in nuclear astrophysics. Many investigations of both astrophysical observation and nucleosynthesis calculation have been carried out to solve the puzzle, but it is not solved yet. Several nuclear reactions involving lithium have been indirectly measured at China institute of atomic energy, Beijing. The Standard BBN (SBBN) network calculations are then performed to investigate the primordial Lithium abundance. The result shows that these nuclear reactions have minimal effect on the SBBN abundances of ^{6}Li and ^{7}Li.

Keywords: Big Bang Nucleosynthesis, element abundance, nuclear reaction network

PACS: 26.35.+c, 97.10.Tk, 95.30.Cq

1 Introduction

Since the pioneering work of Spite M and Spite F [1], the lithium abundance in the metal-poor halo stars was confirmed as a plateau, independent of metallicity and effective temperature. Up to now, the most widely accepted interpretation is that the lithium observed in metal-poor stars has been produced in the big bang nucleosynthesis (BBN). According to the standard Big Bang (SBBN) model, the relative abundances of the light elements (^{1}H, ^{2}H, ^{3}He, ^{4}He, ^{6}Li, and ^{7}Li) depend on only one parameter, namely, the baryon-to-photon ratio η. Using the precisely determined η from cosmic microwave background fluctuations, the lithium-to-hydrogen ratio is predicted to be ^{7}Li/H = $(4.15 \pm 0.5) \times 10^{-10}$ [2], which is higher than observed in metal poor halo stars by roughly a factor of three. Even worsely, the recent claims of detection of isotope-shifted litium absorption lines in a subset of the stars point to a ^{6}Li abundance some three orders of magnitude larger than that expected in SBBN [3].

Where is the tremendous difference of lithium abundances between observation and SBBN model from? Is the lithium problem one of the very few hints that there may be a problem with the big bang model? Are there dissenting views on the interpretation of the stellar spectra? The lithium abundance problems immediately catch the high attention of astronomers, astrophysicists and scientists in the field of nuclear physics. They try to solve the problems in different ways. At the present, the lithium problem is more serious than ever, since the improved observations of stars suggest they contain even less ^{7}Li than previously thought [4].

Although the hot SBBN model code contains most of the nuclear reactions that could be relevant to BBN [5], some reactions on short-lived nuclei are not well studied, and in some cases have not been included. Only when all the reactions involving lithium are taken into account correctly, can the BBN code give the reasonable primordial lithium abundance. It seems appropriate to reexamine the BBN reaction network in order to be sure that all possible reactions are included, and to study the potential effects of those reactions for which data do not considered previously.

Based on above consideration, series of lithium involved reactions, such as ^{6}Li$(n, \gamma)^7$Li, ^{7}Li$(n, \gamma)^8$Li, ^{8}Li$(n, \gamma)^9$Li, ^{6}Li$(p, \gamma)^7$Be, ^{6}He$(p, \gamma)^7$Li, ^{6}He$(p, n)^6$Li, ^{6}He$(d, n)^7$Li, ^{8}Li$(p, \gamma)^9$Be, ^{8}Li$(p, d)^7$Li, ^{8}Li$(p, t)^6$Li, ^{8}Li$(d, p)^9$Li and ^{8}Li$(d, n)^9$Be, were measured at HI-13 tandem accelerator, Beijing. The rates of these nuclear reactions were deduced and then used in the BBN network calculations.

2 Experiments

Figure 1 shows the reaction network used in the present work. The reactions labeled with the dashed line are newly included in the calculations, they may destroy more ^{7}Li and increase the abundance of ^{6}Li. The experiments of these reactions are described as below.

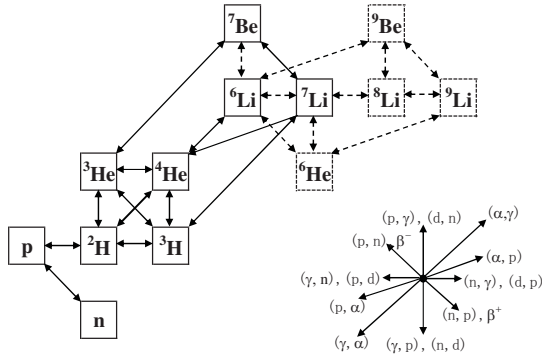**Figure 1**   Reaction network for BBN, as modified from Ref. [6].

2.1 ^{6}Li$(n, \gamma)^7$Li and ^{6}Li$(p, \gamma)^7$Be

The only existing direct measurement of the ^{6}Li$(n, \gamma)^7$Li reaction is not consistent with the values used in some previous reaction network calculations [7,8], thus an independent measurement is needful for clarifying this discrepancy. We measured the angular distributions of the ^{7}Li$(^6$Li,^{6}Li)^{7}Li elastic scattering and ^{7}Li$(^6$Li,^{7}Li$_{g.s.})^6$Li, ^{7}Li$(^6$Li,^{7}Li$_{0.48})^6$Li transfer reactions at $E_{c.m.}$ = 23.7 MeV [9]. The angular distribution for ^{7}Li ground state is shown in Fig. 2.

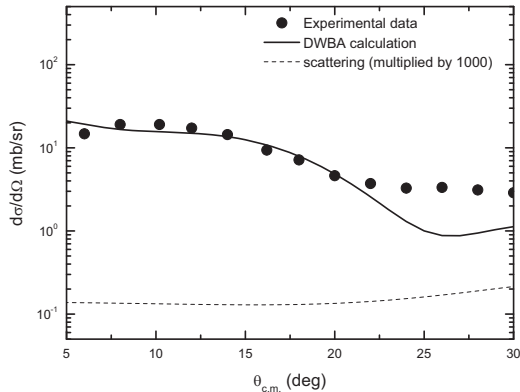**Figure 2**   Angular distribution of ^{7}Li$(^6$Li,^{7}Li$_{g.s.})^6$Li at $E_{c.m.}$ = 23.7 MeV.

By comparing the experimental result with the distorted-wave Born approximation (DWBA) calculation, the neutron spectroscopic factors for the ground and first exited states in ^{7}Li were determined to be 0.78 ± 0.04 and 1.02 ± 0.07, respectively. The results were used to calculate the cross sections of ^{6}Li$(n, \gamma)^7$Li direct capture reaction. The rates were derived to be $(8.1 ± 0.6) \times 10^3 \ cm^3 mol^{-1} s^{-1}$ at the energies of astrophysical interests. Our result is higher by a factor of 1.6 than the value adopted in previous reaction network calculations.

According to charge symmetry, the astrophysical ^{6}Li$(p, \gamma)^7$Be S-factors were derived with the deduced spectroscopic factor. The result indicates that the contributions of ground and first exited states in ^{7}Be are about 63% and 37%, respectively. The calculated astrophysical ^{6}Li$(p, \gamma)^7$Be S(E) factors are in good agreement with the measured total S(E) factors [9].

2.2 ^{6}He$(d, n)^7$Li and ^{6}He$(p, \gamma)^7$Li

The angular distribution of the ^{6}He$(d, n)^7$Li reaction, shown in Fig. 3, was measured with a ^{6}He beam of 36.4 MeV for the first time [10]. The proton spectroscopic factor of ^{7}Li was extracted to be 0.42 ± 0.06 by the normalization of the calculated differential cross sections with the distorted-wave Born approximation to the experimental data [10,11]. The ^{6}He$(p, \gamma)^7$Li cross section as a function of $E_{c.m.}$ was deduced with the extracted ^{7}Li proton spectroscopic factor, as shown in Fig. 4.
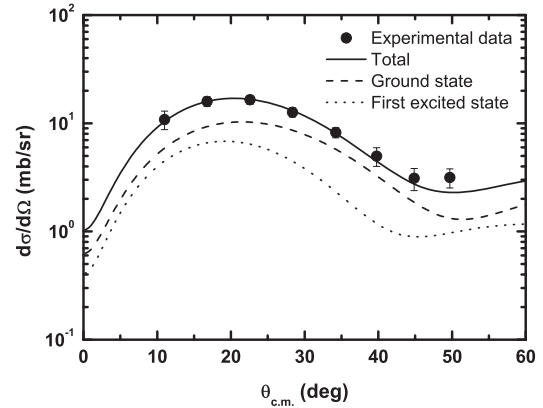
Figure 3   Angular distribution of ^{6}He$(d, n)^7$Li reaction.
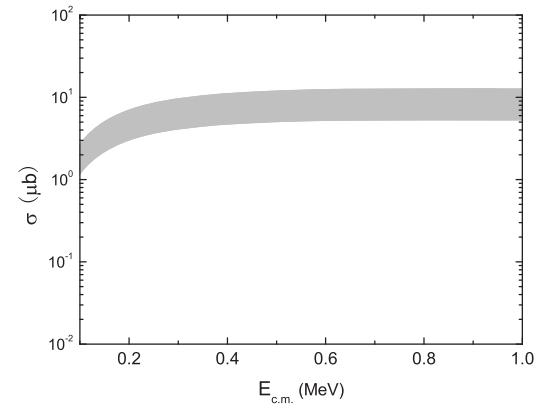
Figure 4   Cross sections of ^{6}He$(p, \gamma)^7$Li reaction at $E_{c.m.}$ < 1.0 MeV.

2.3 ^{6}He$(p, n)^6$Li reaction

The ^{6}He$(p, n)^6$Li reaction is supposed to be a way to increase the primordial ^{6}Li abundance. The angular distributions of ^{6}He$(p, n)^6$Li reaction leading to the ground and 3.563 MeV 0^+ states of ^{6}Li have been measured using the ^{6}He radioactive beam at energy of 4.17 AMeV [12]. The experiment reveals the proton-neutron halo structure of the secondary excited state of ^{6}Li, which was predicted by Arai et al. [13]. The dependence of the cross section as a function of energy in center of mass frame is calculated with the nuclear reaction code Talys [14] to obtain its reaction rates in the energies of astrophysical interest. Figure 5 shows the normalized cross sections with our experimetal data. The errors are from the statistics and theorotical calculations.
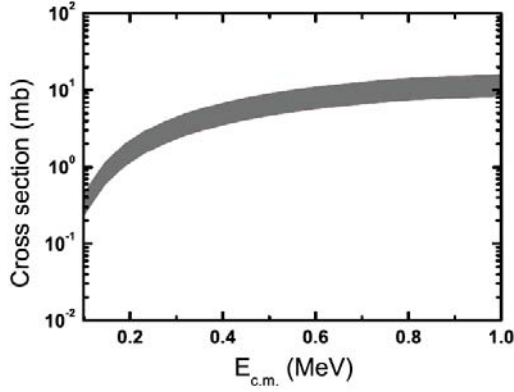
Figure 5 Cross section as a function of $E_{c.m.}$ for the ^{6}He$(p, n)^6$Li reaction.

Figure 7 The cross section of ^{7}Li$(n, \gamma)^8$Li reaction as a function of incident neutron energy. The experimental data are from Refs. [15] and [16].

2.5 ^{8}Li$(d, p)^9$Li and ^{8}Li$(n, \gamma)^9$Li

Figure 8 shows the angular distribution of the ^{8}Li$(d, p)^9$Li reaction, which was measured at $E_{c.m.}$ = 7.8 MeV in inverse kinematics using coincidence detection of ^{9}Li and the recoil proton [17]. Based on DWBA analysis, the ^{8}Li$(d, p)^9$Li cross section was determined to be 7.9 ± 2.0 mb. The cross sections in the energy range of Gamow window can then be deduced via code Talys with the normalized results of the experimental cross section.

Figure 6 Angular distribution of ^{13}C$(^7$Li, ^{8}Li$)^{12}$C reaction. The dashed and dotted lines represent the contributions of $1p_{1/2}$ and $1p_{3/2}$ orbits, respectively.
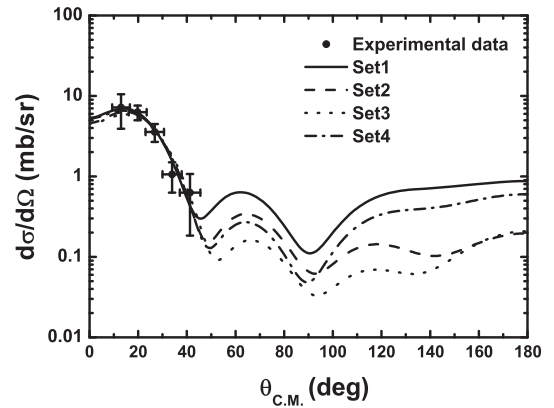
Figure 8 Angular distribution of ^{8}Li$(d, p)^9$Li reaction.

2.4 ^{7}Li$(n, \gamma)^8$Li reaction

We have measured the angular distribution of ^{13}C$(^7$Li,^{8}Li$)^{12}$C one neutron transfer reaction and ^{13}C + ^{7}Li and ^{12}C + ^{7}Li elastic scatterings. The optical potential parameters were derived from the elastic scattering reactions and then used in calculation of transfer angular distribution. The experimental data and the normalized calculation results are shown in Fig. 6. The ratio of the contributions by the $1p_{1/2}$ and $1p_{3/2}$ orbits was determined to be 0.10(3) and the neutron spectroscopic factor of ^{8}Li was extracted to be 0.55 ± 0.06. The spectroscopic factor was then used to deduce the cross section of the ^{7}Li$(n, \gamma)^8$Li reaction. As can be seen in Fig. 7, our indirect measurement is in good agreement with the direct experimental data [15,16].

The single particle spectroscopic factor $S_{1,3/2}$ for ^{9}Li = ^{8}Li $\otimes n$ was derived to be 0.68 ± 0.14, which was then used to calculate the direct capture cross sections for the ^{8}Li$(n, \gamma)^9$Li reaction at energies of astrophysical interest. The result was displayed in Fig. 9. The astrophysical ^{8}Li$(n, \gamma)^9$Li reaction rate for the direct capture was found to be 3970 ± 950 cm^3 mole^{-1}s^{-1} at T_9 = 1. This presents the first experimental constraint for the ^{8}Li$(n, \gamma)^9$Li reaction rates of astrophysical relevance.
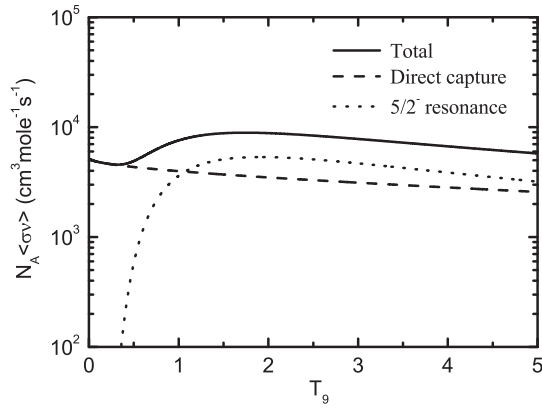
Figure 9 Cross section of $^8\mathrm{Li}(n, \gamma)^9\mathrm{Li}$ reaction.

2.6 $^8\mathbf{Li}(d, n)^9\mathbf{Be}$ and $^8\mathbf{Li}(p, \gamma)^9\mathbf{Be}$

The $^8\mathrm{Li}(d, n)^9\mathrm{Be}$ angular distribution shown in Fig. 10 was measured firstly in inverse kinematics using a ΔE - E_r counter telescope which composed with a 19.3-μm-thick silicon detector and a 300-μm-thick three-ring silicon detector in 2004. The cross section of this reaction was determined to be 9.0 ± 3.4 mb, and the astrophysical S-factor was derived to be 272 ± 103 keV b [18]. The spectroscopic factors of $^9\mathrm{Be}=^8\mathrm{Li} + p$ was found to be 0.64 ± 0.21 with the standard bound state potential parameters (radius r_0 = 1.25 fm, diffuseness a = 0.65 fm) [19]. The energy dependence of direct capture cross section for the $^8\mathrm{Li}(p, \gamma)^9\mathrm{Be}$ reaction was then calculated with the spectroscopic factor and the optical potential model.
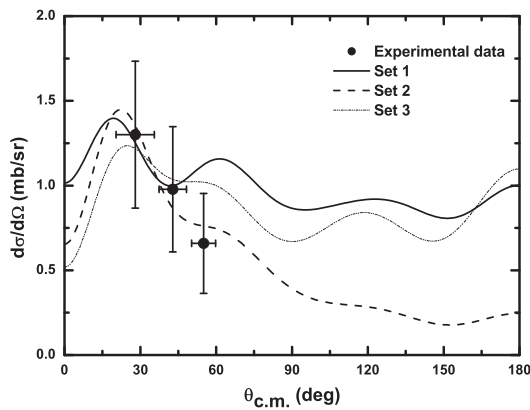
Figure 10 Angular distribution of $^8\mathrm{Li}(d, n)^9\mathrm{Be}$ reaction.

In 2008, a joint group of the scientists from America, Brazil, Mexico measured the angular distribution of $^9\mathrm{Be}(^8\mathrm{Li}, ^9\mathrm{Be})^8\mathrm{Li}$ elastic transfer reaction, and deduced the proton spectroscopic factor of $^9\mathrm{Be}$ to be 1.50 ± 0.28 [20]. Their value is larger than ours by a factor of 2. To clarify this dispersion, we measured the angular distribution of $^{13}\mathrm{C}(^9\mathrm{Be}, ^8\mathrm{Li})^{14}\mathrm{N}$ at HI-13 tandem accelerator in this year. The experimental data was plotted in Fig. 11 and the proton spectroscopic factor of $^9\mathrm{Be}$ was extracted to be 0.72 ± 0.15. The

result proved the correctness of the $^9\mathrm{Be}$ proton spectroscopic factor extracted from the $^2\mathrm{H}(^8\mathrm{Li}, ^9\mathrm{Be})n$ reaction.
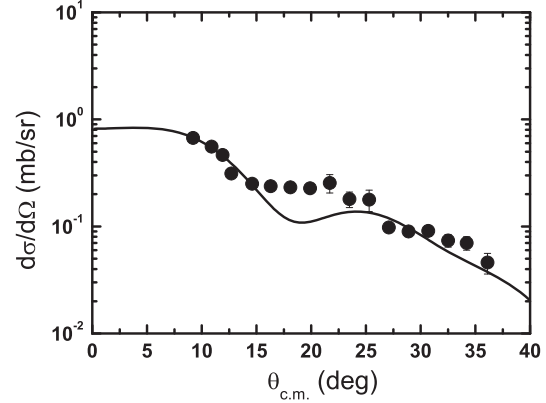
Figure 11 Angular distribution of $^{13}\mathrm{C}(^9\mathrm{Be}, ^8\mathrm{Li})^{14}\mathrm{N}$ reaction.

2.7 $^8\mathbf{Li}(p, d)^7\mathbf{Li}$ and $^8\mathbf{Li}(p, t)^6\mathbf{Li}$

The $^8\mathrm{Li}(p, d)^7\mathrm{Li}$ angular distribution at backward angles, shown in Fig. 12, was measured in inverse kinematics at $E_{\mathrm{c.m.}}$ = 4.0 MeV by using the $^8\mathrm{Li}$ secondary beam for the first time [21]. The ratio of the contributions from $^8\mathrm{Li}(p, d_0)^7\mathrm{Li}$ and $^8\mathrm{Li}(p, d_1)^7\mathrm{Li}^*$ is estimated through energy spectrum of deuteron. The $^8\mathrm{Li}(p, d_0)^7\mathrm{Li}$ component is approximately in agreement with the result deduced from the existing $^7\mathrm{Li}(d, p_0)^8\mathrm{Li}$ reaction data via the principle of detailed balance.
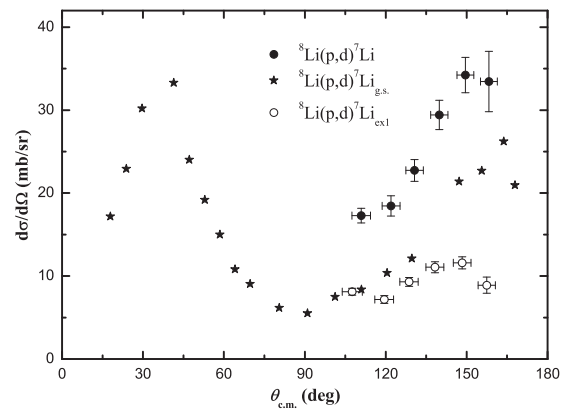
Figure 12 Angular distribution of $^8\mathrm{Li}(p, d)^7\mathrm{Li}$ reaction.

The $^8\mathrm{Li}(p, t)^6\mathrm{Li}$ angular distribution was also extracted from the same experiments, as shown in Fig. 13. The reaction chain of $^7\mathrm{Li}(n, \gamma)^8\mathrm{Li}(p, t)^6\mathrm{Li}$ is thought to be a process for destroying $^7\mathrm{Li}$ and generating $^6\mathrm{Li}$.
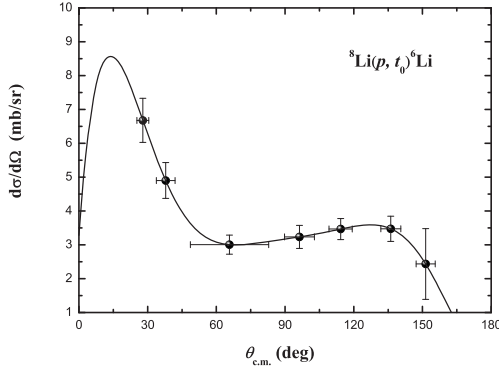
Figure 13 Angular distribution of $^8\text{Li}(p,t)^6\text{Li}$ reaction.

3 Network calculations

With the cross sections of above mentioned reactions, the thermonuclear reaction rates $\langle \sigma v \rangle$ can be calculated by

$$\langle \sigma v \rangle = \left[\frac{8}{\pi \mu}\right]^{1/2} [kT]^{-3/2} \int \sigma(E) E e^{-E/kT} dE, \qquad (1)$$

where μ is the reduced mass of the system, E is the energy in center of mass system, k is the Boltzmann constant, and T is the temperature in Kelvin.

The reaction network calculations have been done with the modification code based on the computational routines of Wagoner [6]. The rate for the abundance change of any nucleus i is determined by the rate equation

$$\frac{dY_i}{dt} = \sum_{i,k,l} N_i\left(-\frac{Y_i^{N_i} Y_j^{N_j}}{N_i! N_j!}[ij]_k + \frac{Y_l^{N_l} Y_k^{N_k}}{N_l! N_k!}[lk]_j\right), \qquad (2)$$

where Y_i is the mass fraction contained in nucleus i, N_m is the number of nuclear m. $[ij]_k$ represents the reaction rate for the reaction between i and j, include the decay rate of nuclear i. The sum in Eq. (2) include all reactions involving nucleus i.
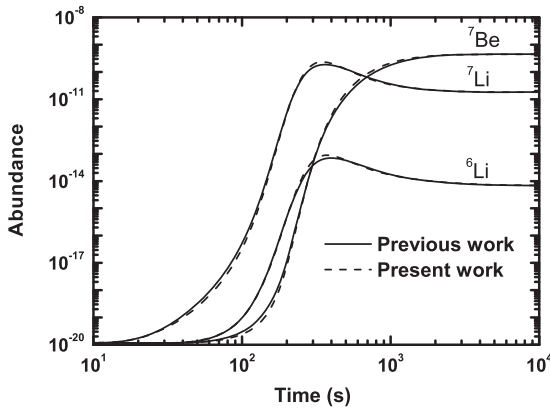
Figure 14 Nuclear abundances as a function of times.

The evolution of the abundances for ^6Li, ^7Li and ^7Be of our calculations is shown in Fig. 14. In general, it was found

that the added reactions slightly changed the lithium abundances at t < 1000 s, but nearly no effect at t > 1000 s. This may be attibuted to the small binding energies of lithium. The detailed study showed that $^6\text{Li}(p,\alpha)^3\text{He}$ could have large effect for destroying ^6Li, leading to the disappearance of the effect of the added reaction. The abundance of ^7Li is sensitive to the $^2\text{H}(p,\gamma)^3\text{He}$, $^3\text{He}(\alpha,\gamma)^7\text{Be}$, and $^7\text{Li}(p,\alpha)^4\text{He}$ reaction rates. Unfortunately, the existing experimental data have large uncertainties. Reducing the uncertainties of these reactions are nesessary to solve ^7Li problem.

4 Conclusion and discussion

We have determined the reaction rates of twelve reactions involving lithium and done the BBN calculations with a expanded network. Unfortunately, the attempts to solve the lithium abundance problem failed. This may result from the large uncertainties of the reaction rates for $^2\text{H}(\alpha,\gamma)^6\text{Li}$, $^2\text{H}(p,\gamma)^3\text{He}$, $^3\text{He}(\alpha,\gamma)^7\text{Be}$ and $^7\text{Li}(p,\alpha)^4\text{He}$. High precision measurements of these reactions would reduce the uncertainty on lithium abundances calculations. In addition, it is of interest to determine some unknown reactions, such as $^7\text{Be}(d,^3\text{He})^6\text{Li}$ and $^4\text{He}(2n,\gamma)^6\text{He}$, they may produce more ^6Li during BBN.

It is very important to investigate the BBN model more carefully. The improvements of the lithium observations in very metal poor stars could also help us to solve the lithium problem.

1 Spite M, Spite F. Lithium abundance at the formation of the Galaxy. Nature, 1982, 297: 483–485

2 Coc A, Vangioni-Flam E, Descouvemont P et al. Update big bang nucleosynthesis compared with Wilkinson Microwave anisotropy probe observations and the abundance of light elements. Astrophys J, 2004, 600: 544–552

3 Asplund M, Lambert D L, Nissen P E et al. Lithium isotopic abundance in metal-poor halo stars. Astrophy J, 2006, 644: 229–259

4 Brooks M. Nine things sent to try us. NewScientist, 2009, 2724: 34–38

5 Smith M S, Kawano L H, and Malaney R A. Spite F. Experimental computational and observational analysis of primordial nucleosynthesis. Astrophys J, 1993, 85: 219–247

6 Wagoner R. Synthesis of the elements within objects exploding from very high temperatures. Astrophys J, 1969, 18: 247–295

7 Malaney R A, Fowler W A. On nuclear reactions and ^9Be production in inhomogeneous cosmologies. Astrophys J, 1989, 345: L5–L8

8 Nollett K M, Lemoine M, Schramm D N. Nuclear reaction rates and primordial ^6Li. Phys Rev C, 1997, 56: 1144–1151

9 Su J, Li Z H, Guo B et al. Neutron spectroscopic factors of 7Li and astrophysical $^6\text{Li}(n,\gamma)^7\text{Li}$ reaction rates. Chin Phys Lett, 2010, 27: 052101

10 Li Z H, Li E T, Guo B et al. First measurement of the $^2\text{Li}(^6\text{He},^7\text{Li})n$ angular distribution and proton spectroscopic factor in ^7Li. Eur Phys J, 2010, 44: 1-5

11 Li Z H, Su J, Guo B et al. ^{2}H(^{6}He,^{7}Li)n, ^{12}C(^{7}Li, ^{6}He)^{13}N reactions and ^{12}C(p, γ)^{13}N astrophysical $S(E)$ factors. Nucl Phys A, 2010, 834: 661-663c

12 Li Z H, Liu W P, Bai X X et al. First observation of neutron-proton halo structure for the 3.563 MeV 0$^+$ state in ^{6}Li via ^{1}H(^{6}He, ^{6}Li)n reaction. Phys Lett B, 2002, 527: 50-54

13 Arai K, Suzuki Y, Varga K. Neutron-proton halo structure of the 3.563-MeV 0$^+$ state in ^{6}Li. Phys Rev C, 1995, 51: 2488-2493

14 Koning A J, Hilaire S, Goriely S. Global and local level density models. Nucl Phys A, 2008, 810: 13–76

15 Blackmon J C, Champagne A E, Dickens J K et al. The ^{7}Li(n, γ_0)^{8}Li cross sections at E_n = 1.5–1340 eV. Phys Rev C, 1996, 54: 383–388

16 Imhof W L, Johnson R G, Vaughn F J et al. Cross sections for the ^{7}Li(n, γ)^{8}Li reaction. Phys Rev, 1959, 114: 1037–1039

17 Li Z H, Liu W P, Bai X X et al. The ^{8}Li(d, p)^{9}Li reaction and the astrophysical ^{8}Li(n, γ)^{9}Li reaction rate. Phys Rev C, 2005, 71: 052801(R)

18 Zeng S, Liu W P, Li Z H et al. Measurement of ^{2}H(^{8}Li,^{9}Be)n reaction relevant to primordial nucleosynthesis. Chin Phys Lett, 2005, 22: 2219–2221

19 Su J, Li Z H, Guo B et al. Astrophysical reaction rates of the ^{8}Li(p, γ)^{9}Be direct capture reaction. Chin Phys Lett, 2006, 23: 55–57

20 Camargo O, Guimarães V, Lichtenthäler et al. The ^{9}Be(^{8}Li, ^{9}Be)^{8}Li elastic-transfer reaction. Phys Rev C, 2008, 78: 034605

21 Li Y J, Li Z H, Guo B et al. Measurement of angular distribution for the ^{8}Li(p, d)^{7}Li reaction. Chin Phys Lett, 2008, 25: 455–457

Astrophysical rates for the ^{6}He(p, γ)^{7}Li reaction

LI ErTao (李二涛)[1], LI ZhiHong (李志宏)[1], SU Jun (苏俊)[1], GUO Bing (郭冰)[1], LI YunJu (李云居)[1],
YAN ShengQuan (颜胜权)[1], BAI XiXiang (白希祥)[1], WANG YouBao (王友宝)[1], WANG BaoXiang (王宝祥)[1],
LIAN Gang (连钢)[1], ZENG Sheng (曾晟)[1], FANG Xiao(方晓)[1], ZHAO Wei-Juan(赵维娟)[2] & LIU WeiPing (柳卫平)[1]

[1]China Institute of Atomic Energy, Beijing 102413, China
[2]Institute of Physical Engineering, Zhengzhou University, Zhengzhou 45005

Angular distribution of the ^{6}He(d, n)^{7}Li reaction at $E_{c.m.}$ = 9.1 MeV is measured in inverse kinematics for the first time. The proton spectroscopic factors for the ground and first excited states of ^{7}Li are derived by using the distorted wave Born approximation analysis. The astrophysical rates of ^{6}He(p, γ)^{7}Li reaction are then deduced and fitted with an expression of REACLIB.

Keywords: transfer reaction, angular distribution, astrophysical reaction rate, spectroscopic factor.

PACS: 21.10.Jx, 25.40.Lw, 26.35.+c

1 Introduction

The standard Big Bang nucleosynthesis (SBBN) model provides a reliable framework for understanding the origin and evolution of the Universe because of the success in explaining the large abundance of ^{4}He with accuracy of one percent. The SBBN model is also success in predicting primordial abundances of ^{2}H and ^{3}He. However, there are clear discrepancies between calculations and observations of lithium abundances since the discovery of a plateau for lithium abundance in mental-poor halo stars by the Spites [1].

According to the SBBN model, the abundances of hydrogen, deuterium, helium and lithium only depend on the baryon to photon ratio η. Using the precise value of η = $(6.14 \pm 0.25) \times 10^{-10}$ determined by Wilkinson Microwave Anisotropy Probe (WMAP) [2], the ^{7}Li to hydrogen ratio in mass fraction is predicted to be (^{7}Li/H)$_p$ = $(4.15\ ^{+0.49}_{-0.45}) \times 10^{-10}$ [3], while the primordial lithium abundance is determined to be (Li/H)$_p$ = $1.23\ ^{+0.68}_{-0.32} \times 10^{-10}$ [4] in metal-poor stars on the Spite plateau, about a factor three lower than calculation. Even more worse, the abundance of ^{6}Li is about three orders of magnitudes higher than that predicted by the SBBN model.

Those differences between calculations and observations are called the lithium problems. In the past few years, some groups attempted to explain the large discrepancies via the studies of both astrophysical observation and nucleosynthesis calculation, yet none of them has been successful up to now. In the SBBN network, ^{6}He may be produced by the ^{4}He($2n, \gamma$)^{6}He reaction [5], and then affects the abundances of ^{6}Li and ^{7}Li through its β^- decay and ^{6}He(p, γ)^{7}Li reaction, respectively.

In this paper, angular distribution of the ^{6}He(d, n)^{7}Li reaction is measured in inverse kinematics at $E_{c.m.}$ = 9.1 MeV for the first time. The proton spectroscopic factors for the $<^7$Li$_{g.s.}|^6$He+$p >$ and $<^7$Li$_{0.48}|^6$He+$p >$ bound systems are derived based on the distorted wave Born approximation (DWBA) analysis. The astrophysical $S(E)$ factors and rates of the ^{6}He(p, γ)^{7}Li which include the contributions of ^{6}He(p, γ)^{7}Li$_{g.s.}$ and ^{6}He(p, γ)^{7}Li$_{0.48}$ reactions are then deduced.

2 Experiment

The experiment is carried out at the secondary beam facility [6, 7, 8] of the HI-13 tandem accelerator, Beijing. The experimental setup is shown in Fig. 1. A 46 MeV ^{7}Li primary beam from the tandem accelerator impinges on a 4.8 cm long deuterium gas cell at pressure of 1.5 atm to yield ^{6}He ions via ^{2}H(^{7}Li, ^{6}He)^{3}He reaction. The front and rear windows of the gas cell are Havar foils with thickness of 1.9 mg/cm^2. After the magnetic separation with a dipole and focalization with a quadruple doublet, a 37.7 MeV ^{6}He secondary beam is delivered and then collimated by two apertures in diameters of 7 mm and 5 mm. During the experiment, the typical intensity of the secondary beam is about 3000 pps and the purity of ^{6}He ions is better than 99%. The main contaminants in the secondary beam are ^{7}Li ions from Rutherford scattering of the primary beam in the gas cell windows and beam tube. In order to eliminate their disturbance to the ^{7}Li events from the ^{6}He(d, n)^{7}Li reaction, a 23 μm thick silicon ΔE detector is placed at 20 mm upstream of the secondary target, which serves as both particle identification and beam normalization.

A $(CD_2)_n$ foil and a carbon foil, both with thickness of 1.7 mg/cm^2 are used to measure the ^{7}Li ions from ^{6}He$(d, n)^7$Li reaction and background, respectively. The energy of ^{6}He ions at the middle of the $(CD_2)_n$ foil is 36.4 MeV. A 300 μm thick multi-ring semiconductor detector (MRSD) with center hole is used as a residue energy (E_r) detector which is composed of a ΔE - E_r counter telescope together with a 23 μm thick silicon ΔE detector and an independent 300 μm thick center silicon detector (CSD).
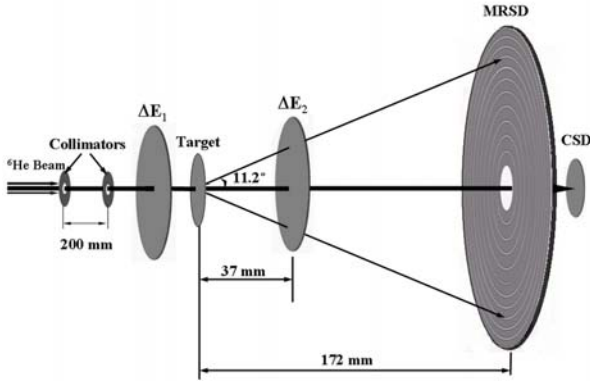
Figure 1: Schematic layout of the experiment.

The measured ^{6}He$(d, n)^7$Li angular distribution is shown in Fig. 2, which includes the contributions from the ground and first excited states in ^{7}Li because these two states can not be separated for their energy difference is less than the energy spread of ^{6}He beam. According to the theoretical calculation, the proton spectroscopic factors in ^{7}Li ground and first states are equal to each other [9]. The DWBA code is adopted in the data analysis and the calculated angular distributions are also presented in Fig. 2. The proton spectroscopic factors for the ground and first excited states of ^{7}Li are deduced to be 0.42 ± 0.06 [10].
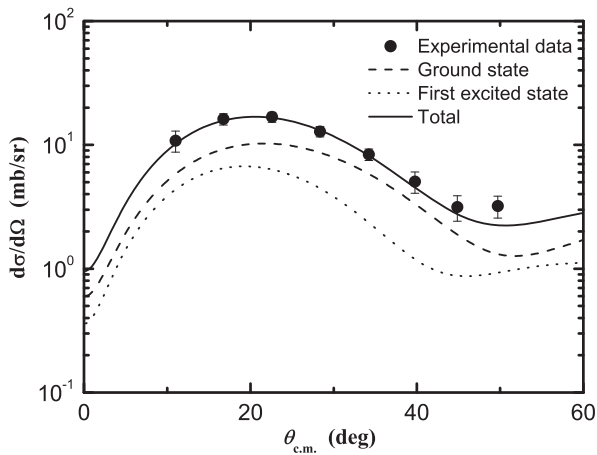
Figure 2: Angular distribution of the ^{6}He$(d, n)^7$Li reaction at $E_{c.m.} = 9.1$ MeV together with the DWBA calculations.

3 Analysis

In the energy region of astrophysical interest, the ^{6}He$(p, \gamma)^7$Li$_{g.s.}$ and ^{6}He$(p, \gamma)^7$Li$_{0.48}$ cross sections are dominated by $E1$ radiative capture of s-wave proton into the ground and first excited states of ^{7}Li. According to the traditional direct capture model [11, 12], the cross section can be deduced with the extracted spectroscopic factor $S_{l_f j_f}$ by:

$$\sigma = \frac{16\pi}{9}\left(\frac{E_\gamma}{\hbar c}\right)^3 \frac{e_{eff}^2}{k^2}\frac{1}{\hbar v}\frac{(2I_f + 1)}{(2I_1 + 1)(2I_2 + 1)}S_{l_f j_f} \times$$
$$\left|\int_0^\infty r^2 w_{l_i}(kr)u_{l_f}(r)dr\right|^2, \quad (1)$$

where E_γ is the emitted γ-ray energy; v is the relative velocity between target nucleus and proton; I_1, I_2 and I_f are the spins of target nucleus, proton and compound nucleus, respectively; $e_{eff} = eZ/A$ represents the proton effective charge for the $E1$ transition in the potential produced by a target nucleus with mass number A and atomic number Z; $k = \sqrt{2\mu E_{cm}}\hbar$ stands for the incident wave number; $w_{l_i}(kr)$ refers to the distorted radial wave function for the entrance channel; $u_{l_f}(r)$ denotes the radial wave function of the bound state proton in compound nucleus which can be calculated by solving the respective Schrödinger equation.

In order to extrapolate the cross section down to the low energies of astrophysical interest, the astrophysical $S(E)$ factor is defined as:

$$S(E) = E\sigma(E)exp(-2\pi\eta), \quad (2)$$

where η is the Sommerfeld parameter:

$$\eta = \frac{Z_1 Z_2 e^2}{\hbar v} = 0.1575 Z_1 Z_2 \left(\frac{\mu}{E}\right)^{\frac{1}{2}}, \quad (3)$$

μ is the reduced mass of the system, Z_1 and Z_2 are the atomic number of target nucleus and proton.

To calculate the wave function $w_{l_i}(kr)$ in Eq. 1, one has to know the optical potential parameters of the elastic scattering of ^{6}He + p system at $E_{c.m.} < 1$ MeV, which can be obtained by analyzing the ^{6}He$(p, p)^6$He angular distribution. However, no experimental data are available at such low energy presently. We assume that the imaginary part of the potential is negligible [13]. As to the real part, a Wood-Saxon potential is adopted, the radius and diffuseness parameters are set to be the standard values $r_0 = 1.25$ fm and $a = 0.65$ fm.
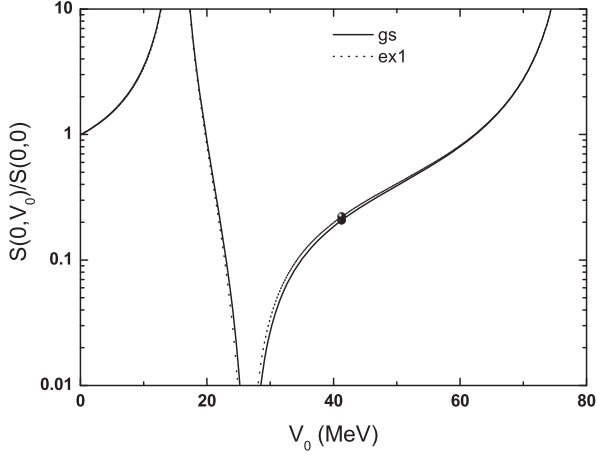
Figure 3: The V_0 related $S(E)$ factors scale to $S(0,0)$ for the ^{6}He(p, γ)^{7}Li$_{g.s.}$ and ^{6}He(p, γ)^{7}Li$_{0.48}$ reactions. The potential depthes V_0 used in the calculations are indicated.

In general, the potential depth of the continuum state plays an important role. To investigate the importance of the potential depth V_0 on the direct radiative capture cross section, we calculate the V_0 related astrophysical $S(0)$ factors $S(0, V_0)$, which are scaled to the $S(E)$ factors calculated with pure Coulomb wave function $S(0, 0)$, for the ^{6}He(p, γ)^{7}Li$_{g.s.}$ and ^{6}He(p, γ)^{7}Li$_{0.48}$ reactions. The results are present in Fig. 3, it demonstrates the sensitivity of the astrophysical $S(E)$ factors to the choice of the scattering potential depth V_0. In such case, the depth must be fixed by fitting the volume integral of potential per nucleon [14]. Although the optical potential changes considerably for different systems, the volume integral of potential per nucleon is relatively a more stable quantity.
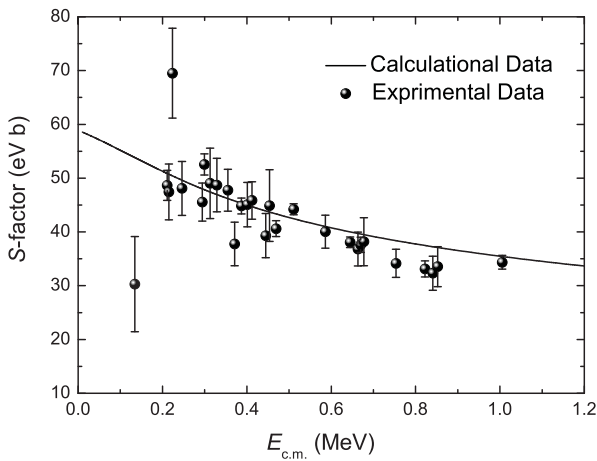
Figure 4: $S(E)$ factors for the ^{6}Li(p, γ)^{7}Be$_{g.s.}$ reaction, the experimental data (filled circles) are taken from Ref. [15].

The measured cross sections of ^{6}Li(p, γ)^{7}Be$_{g.s.}$ at low energies [15] is shown in Fig. 4. The potential depth of ^{6}Li $+ p$ system is determined to be 41.3 $\pm$ 2.0 MeV by fitting the ex-

perimental data using the weight least square method, which can be used by ^{6}He $+ p$ system since both ^{6}Li and ^{6}He have the same mass number.

The energy dependence of astrophysical $S(E)$ factor for the ^{6}He(p, γ)^{7}Li reaction is extracted with the obtained spectroscopic factors and the above potential parameters, as shown in Fig. 5, which contains the contributions of ^{6}He(p, γ)^{7}Li$_{g.s.}$ and ^{6}He(p, γ)^{7}Li$_{0.48}$ reactions. The $S(0)$ factor is found to be 111.9 $\pm$ 21.6 eV b. The error results from the uncertainties of spectroscopic factor (14%) and the potential depth (13%).
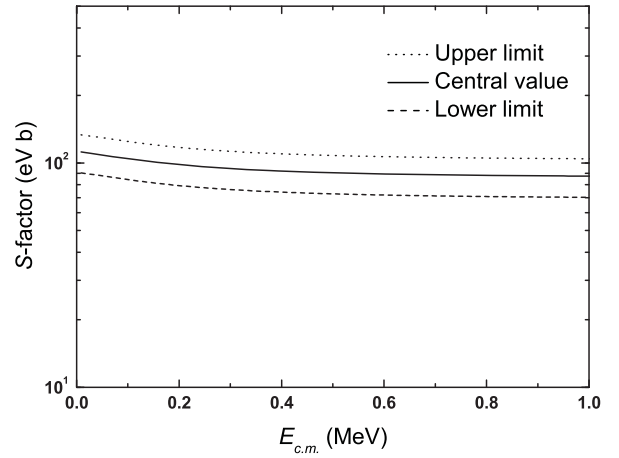
Figure 5: Astrophysical $S(E)$ factors as a function of $E_{c.m.}$ for the ^{6}He(p, γ)^{7}Li reaction, which contain the contributions of ^{6}He(p, γ)^{7}Li$_{g.s.}$ and ^{6}He(p, γ)^{7}Li$_{0.48}$ reactions.

Usually, the temperature dependence of reaction rate for the direct capture can be calculated by:

$$N_A \langle \sigma v \rangle = N_A \left(\frac{8}{\pi \mu} \right)^{1/2} \frac{1}{(k_B T)^{3/2}} \times \int_0^\infty S(E) E \exp[-\frac{b}{E^{1/2}} - \frac{E}{kT}] dE \quad (4)$$

where N_A is the Avogadro number, k presents the Boltzmann constant, and b is given by:

$$b = \frac{(2\mu)^{1/2} \pi e^2 Z_1 Z_2}{\hbar}, \quad (5)$$

the square of b is so-called the Gammow energy.
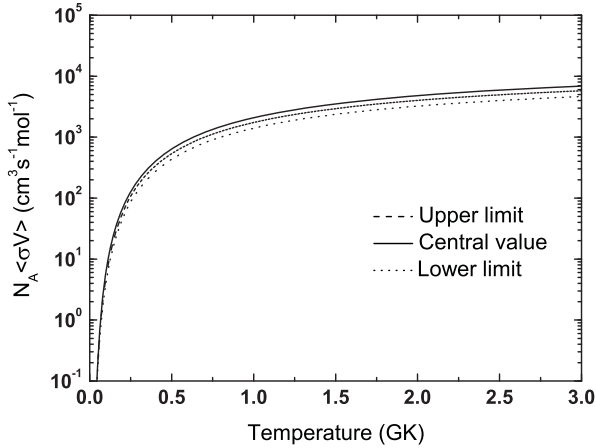
Figure 6: Temperature dependence of the $^6\text{He}(p, \gamma)^7\text{Li}$ reaction rates. The solid, dashed and dotted lines are the central value, upper and lower limit, respectively.

By substituting $S(E)$ factors given in Fig. 5 into Eq. (4), the $^6\text{He}(p, \gamma)^7\text{Li}$ direct radiative capture reaction rates are then obtained, as shown in Fig. 6. The total reaction rates as a function of temperature T_9 (in unit of 10^9 K) are fitted with an expression used in the astrophysical reaction rate library REACLIB [16]:

$$\begin{aligned} N_A < \sigma v > \quad = \quad & \exp[15.638 - 0.0428983T_9^{-1} - 4.05561T_9^{-1/3} \\ & -4.37573T_9^{1/3} + 0.32091T_9 - 0.0224889T_9^{5/3} \\ & +1.21365 \ln T_9], \end{aligned} \tag{6}$$

The fitting errors are less than 1% in the temperature range from $T_9 = 0.01$ to $T_9 = 10$.

4   Summary

In summary, the measurement of differential cross sections for the $^6\text{He}(d, n)^7\text{Li}$ transfer reaction has been carried out at $E_{c.m.} = 9.1$ MeV. The astrophysical $S(E)$ factors and rates for $^6\text{He}(p, \gamma)^7\text{Li}$ direct radiative capture reaction are then deduced by using the extracted proton spectroscopic factors. The BBN network calculation which includes $^4\text{He}(2n, \gamma)^6\text{He}(\beta^- \bar{\nu})^6\text{Li}$ and $^4\text{He}(2n, \gamma)^6\text{He}(p, \gamma)^7\text{Li}$ is under way to reveal the effect of this reaction chain on the primordial lithium abundances.

References

[1]. Spite F et al. 1982 *Astro. Astrophys.* **115** 357.
[2]. Spergel D N et al. 2003 *The Astrophys. Journ. Suppl. Series* **148** 175.
[3]. Coc A 2004 *The Astrophys. Journ.* **600** 544.
[4]. Ryan S G 2000 *The Astrophys. Journ.* **530** 57(L).
[5]. Görres J et al. 1995 *Phys. Rev. C* **52** 4.
[6]. Bai X X et al. 1995 *Nucl. Phys. A* **588** 273(C).
[7]. Liu W P et al. 2003 *Nucl. Instrum. Methods B* **204** 62.
[8]. Liu W P et al. 2005 *Nucl. Phys. A* **758** 110(C).
[9]. Rudchik A A et al. 2005 *Phys. Rev. C* **72** 034608.
[10]. Li Z H et al. 2010 *Eur. Phys. J. A* **44** 1.
[11]. Rolfs C 1973 *Nucl. Phys. A* **217** 29.
[12]. Li Z H et al. 2005 *Phys. Rev. C* **71** 052801(R).
[13]. Su J et al. 2006 *Chin. Phys. Lett.* **23** 55.
[14]. Camargo O et al. 2008 *Phys. Rev. C* **78** 034605.
[15]. Switkowski Z E et al. 1979 *Nucl. Phys. A* **331** 50.
[16]. Thielemann F K et al. 1987 *Advances in Nuclear Astrophysics,* edited by Vangioni-Flam E et al. (Gir-sur-Yvette: Editions Frontieres).

Study of proton resonances in ^{18}Ne via resonant elastic scattering of ^{17}F+p and its astrophysical implication in the stellar reaction of ^{14}O$(\alpha,p)^{17}$F

J.J. He[1], J. Hu[1], S.W. Xu[1], Z.Q. Chen[1], X.Y. Zhang[1], J.S. Wang[1], H.W. Wang[3], W.D. Tian[4], X.Q. Yu[1], L.Y. Zhang[1,2], L. Li[1,2], Y.Y. Yang[1,2], P. Ma[1], X.H. Zhang[1], J. Su[4], E.T. Li[4], Z.G. Hu[1], Z.Y. Guo[1], X. Xu[1,2], X.H. Yuan[1], W. Lu[1,2], Y.H. Yu[1,2], Y.D. Zang[1,2], S.W. Ye[1,2], R.P. Ye[1,2], J.D. Chen[1,2], S.L. Jin[1,2], C.M. Du[1,2], S.T. Wang[1,2], J.B. Ma[1], L.X. Liu[1,2], Z. Bai[1,2], X.Q. Li[5], X.G. Lei[1], Z.Y. Sun[1], Y.H. Zhang[1], X.H. Zhou[1] & H.S. Xu[1]

[1] *Institute of Modern Physics, Chinese Academy of Sciences (CAS), Lanzhou 730000, China*
[2] *Graduate School of Chinese Academy of Sciences, Beijing 100049, China*
[3] *Shanghai Institute of Applied Physics (SINAP), Chinese Academy of Sciences, Shanghai 201800, China*
[4] *China Institute of Atomic Energy (CIAE), P.O. Box 275(10), Beijing 102413, China*
[5] *School of Physics and State Key Laboratory of Nuclear Physics and Technology, Peking University, Beijing 100871, China*

The stellar ^{14}O$(\alpha,p)^{17}$F reaction is thought to be one of the most important breakout reactions from the Hot CNO cycles into the *rp*-process in Type I x-ray bursters. In the present work, the properties of proton resonances in ^{18}Ne have been investigated efficiently by utilizing a technique of proton resonant elastic scattering with a ^{17}F radioactive ion (RI) beam and a thick proton target. A 4.22 MeV/nucleon ^{17}F RI beam, which was produced via a projectile-fragmentation reaction and experiencing a series of energy degradation, was separated by a Radioactive Ion Beam Line in Lanzhou (RIBLL) and bombarded a $(CH_2)_n$ target. Energy spectra of the recoiled protons were measured by two sets of ΔE-E silicon telescope at center-of-mass scattering angles of $\theta_{c.m.} \approx 175° \pm 5°$, $\theta_{c.m.} \approx 152° \pm 8°$, respectively. Several proton resonances in ^{18}Ne were observed, and their resonant parameters have been determined by an *R*-matrix analysis of the differential cross sections. A doublet structure around 7.10 MeV has been identified and thought to be one state at 7.05 MeV (2$^+$) and another one at 7.12 MeV (4$^+$). The presently calculated total reaction rates of ^{14}O$(\alpha,p)^{17}$F are, at least, a factor of 1.2~1.9 larger than the previous ones in temperature region of 1.7~3.0 GK mainly owing to the contribution from the 7.05-MeV (2$^+$) state. This result implies that this breakout reaction may play a more important role than previously expected.

PACS: 25.60.-t, 25.40.Ny, 26.20.Fj, 26.30.Ca

1 Introduction

Explosive hydrogen and helium burning are thought to be the main sources for energy generation and nucleosynthesis of heavier elements in cataclysmic binary systems, for example, Type I x-ray bursters [1, 2, 3]. In such a close binary system, hydrogen and helium rich material from a companion star pile up onto the surface of a neutron star, and form an accretion disk where thermal runaway reactions can be ignited through both the triple-α reaction and breakout from the hot carbon-nitrogen-oxygen (CNO) cycles into the rapid proton capture process (*rp*-process). Energy generation increases rapidly as a function of temperature, and hence the rate of energy release can increase faster than the rate of cooling, ultimately leading to uncontrollable thermonuclear explosions in the accreting disk, the so called Type I x-ray bursts [4]). The αp chain is initiated through the reaction

sequence ^{14}O$(\alpha,p)^{17}$F$(p,\gamma)^{18}$Ne$(\alpha,p)^{21}$Na [5], and increases the rate of energy generation by 2 orders of magnitude [3]. In x-ray burster scenarios, the nucleus ^{14}O ($t_{1/2}$=71 s) forms an important waiting point, and the ignition of the ^{14}O$(\alpha,p)^{17}$F reaction at temperatures ~0.4 GK produces a rapid increase in power and can lead to breakout from the hot CNO cycles into the *rp*-process with the production of medium mass proton-rich nuclei [6, 7, 8]. As a crucial breakout reaction, its reaction rate determines the conditions under which the bursts are initiated and triggered, and thus plays an important role in the field of nuclear astrophysics.

Wiescher *et al.* [9] calculated the reaction rates of ^{14}O$(\alpha,p)^{17}$F in detail, and showed that the resonant reaction rates dominated the total rates above temperature ~0.3 GK. Later on, Funck *et al.* [10, 11] found that direct-reaction contribution to the $\ell=1$ partial wave was comparable to or even greater than the resonant one at certain temperatures. Since resonant reaction rates of ^{14}O$(\alpha,p)^{17}$F depend sensi-

tively on the resonant energies, spin-parities, partial and total widths of the relevant excited states in the compound nucleus ^{18}Ne, Hahn *et al.* [12] extensively studied the levels in ^{18}Ne by three reactions, ^{16}O(^{3}He,n)^{18}Ne, ^{12}C(^{12}C,^{6}He)^{18}Ne and ^{20}Ne(p,t)^{18}Ne. It was found that this reaction rate, at temperature above ~0.5 GK, was dominated by capture on a single 1^- resonance at an excitation energy of 6.150 MeV lying 1.035 MeV above the ^{14}O+α threshold (Q_α=5.115 MeV [13]). Harss *et al.* [14] studied the time reverse reaction ^{17}F(p,α)^{14}O by using a ^{17}F beam at ANL, and determined the resonance strengths for three levels at 7.16, 7.37, 7.60 MeV. Later, Gómez del Campo *et al.* [15] used a p(^{17}F,p) resonant elastic scattering on a thick CH$_2$ target to look for resonances of astrophysical interest in ^{18}Ne at ORNL, and assigned the E_x=6.15, 6.35 MeV states as J^π=1^-, and 2^-, respectively. Subsequently, a new set of resonant parameters [E_r, J^π, Γ, *etc.*] for several resonances in ^{18}Ne were deduced from another experiment at ANL [16], and the spin-parities were re-assigned based on the Coulomb-shift calculation as well as Fortune and Sherr's comments [17]. The resonance strength and Γ_α width for the 6.15-MeV state was extracted based on a 1^- assignment as well as the previously obtained excitation function [14]. In addition, the inelastic component of this key 1^- resonance in the ^{14}O(α,p)^{17}F reaction was also studied by a new highly sensitive technique at ISOLDE/CERN [18, 19]. It was found that this inelastic component would enhance the reaction rate, contributing approximating equally to the ground-state component of the reaction rate, however not to the relative degree suggested in Ref. [20]. Although our understanding in the reaction rates of ^{14}O(α,p)^{17}F has been greatly improved so far, there are still some discrepancies to be cleared. Recently, the 1^- assignment for the 6.15-MeV state was questioned [21] by a careful reanalysis of the previous experimental data [15]. It has been found that most probably the 6.286-MeV state is the key 1^- state whereas the 6.15-MeV state is a 3^- or 2^- state, and hence the resonance at E_x=6.286 MeV probably dominates the reaction rates in the temperature below ~2 GK [21]. However, low statistics of experimental data [15] around E_x=6.286 MeV prevent us from putting the new assignments on a very firm ground.

Figure 1: Schematic view of the RIBLL. All relevant parameters are indicated in the figure.

In the present work, we have investigated the proton resonant properties of the compound nucleus ^{18}Ne, covering an

excitation energy (E_x) region of 4.7~8.0 MeV, by using a resonant elastic scattering of a ^{17}F beam with a thick (CH$_2$)$_n$ target. This sort of thick-target method [22, 23, 24, 25, 26] enables simultaneous measurements of excitation function within a very wide energy range. Proton resonant parameters have been determined by an *R*-matrix analysis of the differential cross sections of ^{17}F+p, and the astrophysical implication of ^{14}O(α, p)^{17}F reaction is briefly discussed based on the present work.

2 Experiment

The experiment was carried out by using the Heavy Ion Research Facility in Lanzhou (HIRFL) [27, 28]. A primary beam of ^{20}Ne^{10+} was accelerated up to 69.5 MeV/nucleon by a Separate Sector Cyclotron (SSC, K = 450) with an intensity of ~300 enA, and bombarded a 4094-μm ^{9}Be primary target. A secondary beam of ^{17}F^{9+}, which was produced via a projectile-fragmentation reaction mechanism, was then separated, purified, and transported by a Radioactive Ion Beam Line in Lanzhou (RIBLL)[29] to the secondary target chamber.

The schematic view of RIBLL is shown in Fig. 1. At the momentum-dispersive focal plane (**C1**), a 313-μm flat-shaped Al degrader was installed to separate the ^{17}F^{9+} particles from other reaction products. In order to meet physics requirement, the particle energies were subsequently reduced by two degraders (a 323-μm Si and a 294-μm Al) and a 34-μm C$_9$H$_{10}$ plastic scintillator (hereafter referred to as TOF1) at the intermediate focal point (**T1**). Two horizontal slits were used to purify the beam and to restrict the momentum spreads of the ^{17}F^{9+} particles, here, the momentum spread $\Delta p/p$ was limited to ±0.34% at **C1** and to ±0.92% at **C2**, respectively.
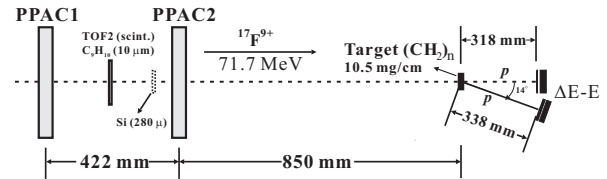
Figure 2: Experimental setup for the scattering measurement at T2. See text for details.

At the achromatic focal plane (**T2**), a scattering setup was installed inside a vacuum chamber as shown in Fig. 2. The setup consisted of two parallel-plate avalanche counters (PPACs)[30], one 10-μm C$_9$H$_{10}$ plastic scintillator (hereafter referred to as TOF2), one 10.5-mg/cm^2 (CH$_2$)$_n$ target and two sets of ΔE-E silicon telescope detection system. During the beam tuning, a 280-μm Si detector was inserted just before PPAC2 to measure the total energies of the particles (see the dashed box in Fig. 2). All beam particles can be identified clearly by using the time-of-flight (TOF) measured by the TOF1 and TOF2 scintillators, together with the total en-

ergy deposited in the Si detector in an event-by-event mode. Figure 3 shows an identification plot for the beam particles, and it can be seen that the ^{17}F^{9+} particles can be identified completely by using the TOF information only. Although this Si detector was moved out during the experimental runs, the ^{17}F^{9+} particles can be identified uniquely by using the TOF information as shown in Fig. 4. The position and incident angle of the beam particles on the target have been determined by extrapolating the two-dimensional hit positions measured by two PPACs whose position resolution is about 1 mm (FWHM) [30].
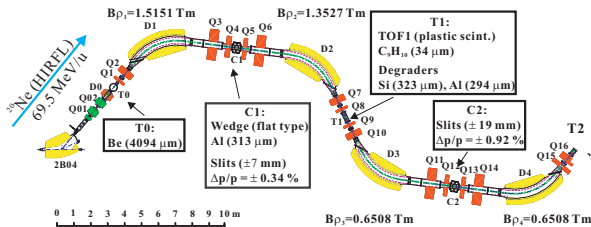
At (CH$_2$)$_n$ target position, the average intensity of ^{17}F^{9+} beam was about 1×10^3 particles/s with a ~50% purity. The ^{17}F^{9+} beam-spot widths (FWHM) were 17 mm horizontally and 16 mm vertically. The horizontal and vertical angular spread (FWHM) of the beam were 30 mrad and 9 mrad, respectively. The mean energy of ^{17}F^{9+} was 4.22 MeV/nucleon with a 0.25 MeV/nucleon width (FWHM). In addition, the experimental data with a C target (10.7 mg/cm^2) was also acquired in a separate run to evaluate the contributions from the reactions of ^{17}F with C nuclei contained in the (CH$_2$)$_n$ target.
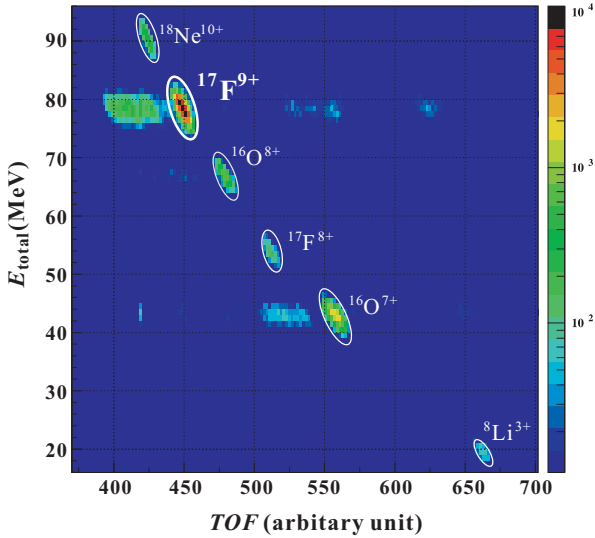
Figure 3: Identification plot for the beam particles. Where, E_{total} indicates the total beam energy deposited in the 280-μm Si detector at T2 (just before PPAC2), and TOF indicates the time-of-flight measured by TOF1 & TOF2 detectors at T1 and T2. See text for details.

All beam particles were fully stopped in the thick (CH$_2$)$_n$ target. Light particles recoiled from the target were measured by using two sets of ΔE-E silicon detectors (Micron Semiconductor Ltd. [31]) at scattering angles, $\theta_{lab}\approx0°$, 14°, respectively (see Fig. 2). At $\theta_{lab}\approx0°$, the telescope was consisted of a 63-μm-thick W1-type double-sided-strip (16×16 strips) detector and a 1500-μm-thick MSX25-type pad detector; at $\theta_{lab}\approx14°$, the telescope was consisted of a 300-μm-

thick MSQ25-type detector and a 1000-μm-thick MSPX042-type double-sided-strip (16×16 strips) detector. Each silicon detector had a sensitive area of 50×50 mm^2 and subtended an angular range of $\Delta\theta_{lab}\approx9°$. Two telescopes covered laboratory solid angles ($\Delta\Omega_{lab}$) about 25 msr and 22 msr, respectively. In the center-of-mass (c.m.) frame, the scattering angles covered by two telescopes are $\theta_{c.m.}\approx175°\pm5°$ and $\theta_{c.m.}\approx152°\pm8°$, respectively. The recoiled protons were clearly identified by the energies deposited both in ΔE and E detectors as shown in Fig. 5, where the energy calibration for detectors was performed by using a standard triple α source.
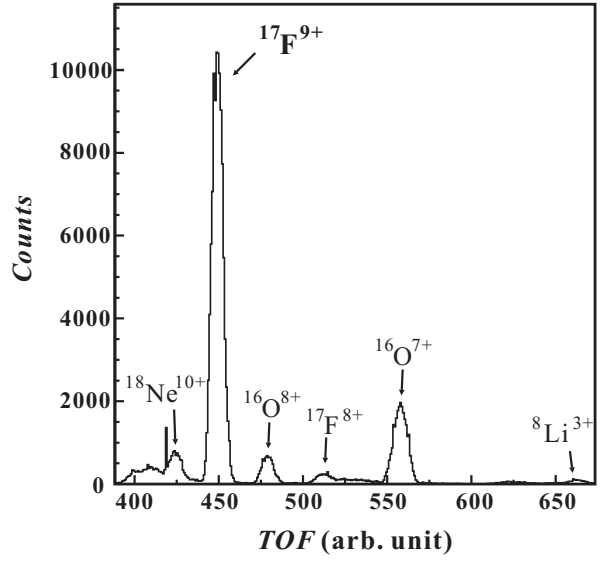
Figure 4: Identification plot for the beam particles in a typical TOF spectrum.
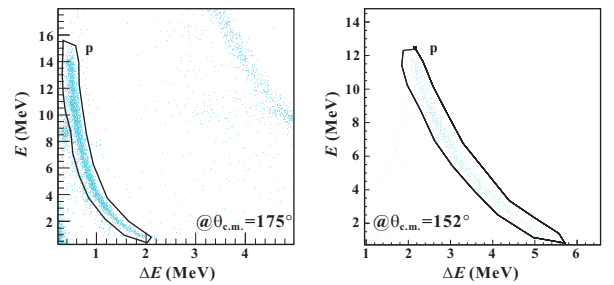
Figure 5: Identification plot for the recoiled particles in two ΔE-E telescopes. The polygonal boxes for the proton gates are shown and utilized in the analysis.

3   Results and Discussions

Differential cross section for the ^{17}F+p elastic scattering in the c.m. frame has been calculated by the following relation-

ship (*e.g.*, see [23, 25])

$$\frac{d\sigma}{d\Omega_{c.m.}}(E_{c.m.}, \theta_{c.m.}) = \frac{1}{4\cos\theta_{lab}} \times \frac{N_p}{I_b N_H \Delta\Omega_{lab}}, \quad (1)$$

where N_p is the number of detected protons, *i.e.*, at energy interval of $E_{c.m.} \rightarrow E_{c.m.} + \Delta E_{c.m.}$; I_b is the total number of $^{17}F^{9+}$ beam particles bombarding on the $(CH_2)_n$ target; N_H is the number of H atoms per unit area per energy bin ($\Delta E_{c.m.}$) in the target [32]. Here, center-of-mass energy, $E_{c.m.}$, for the $^{17}F+p$ elastic scattering has been calculated by (*e.g.*, see [25])

$$E_{c.m.} = \frac{A_b + A_t}{4A_b \cos^2\theta_{lab}} E_p, \quad (2)$$

where A_b and A_t are the mass numbers of the beam and target nuclei; the proton energy at the reaction point, E_p, has been calculated through the total energy deposited in the detectors by making a correction for the proton energy loss in the target. Thus, energy of the excited state in ^{18}Ne can be calculated by $E_x = E_r + S_p$, thereinto the proton separation energy of ^{18}Ne is $S_p = 3.924$ MeV [13], and the resonant energy E_r has been determined by the R-matrix analysis discussed below. The uncertainty of the deduced excitation energy is estimated to be about ±30 keV.
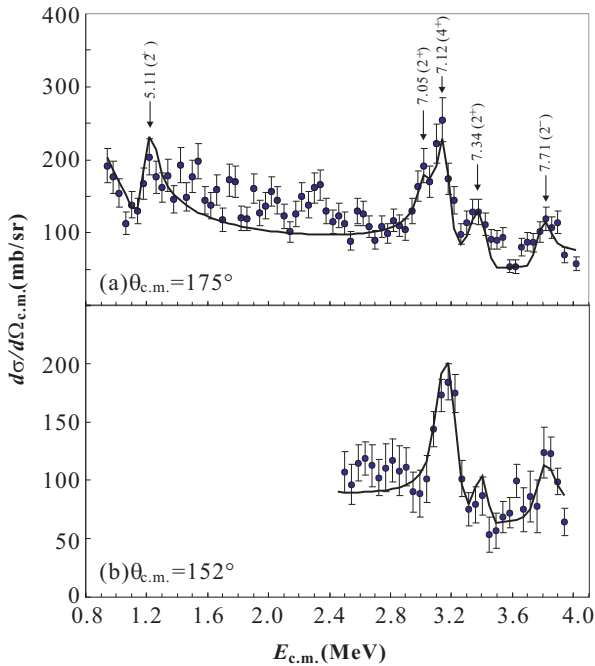
Figure 6: The c.m. differential cross sections for elastically scattered protons produced by bombarding a thick $(CH_2)_n$ target with 71.7 MeV ^{17}F particles at scattering angles of (a) $\theta_{c.m.} \approx 175° \pm 5°$ and (b) $\theta_{c.m.} \approx 152° \pm 8°$. The curved lines represent the R-matrix fits to the data, see text for details.

Figure 6(a)&(b) show the deduced c.m. differential cross sections for the $^{17}F+p$ elastic scattering at angles of

$\theta_{c.m.} \approx 175° \pm 5°$ and $\theta_{c.m.} \approx 152° \pm 8°$, respectively. The uncertainties shown in the figures are mainly the statistical ones. Note the data shown in Fig. 6(b) were eliminated below 2.4 MeV because of the electronics noise.

In order to determine the resonant parameters of the observed resonances, the multichannel R-matrix calculations [33, 34, 35] (see example [21, 36]) that include the energies, widths, spins, angular momenta, and interference sign for each candidate resonance have been performed in the present work. A channel radius of $R=4.464$ fm [$=1.25 \times (1+17^{1/3})$ fm] appropriate for the $^{17}F+p$ system[9, 12, 15] has been utilized in the present R-matrix calculation, where the fitting results are insensitive to the choice of radius within the present statistics. The ground state spin-parity configurations of ^{17}F and proton are $5/2^+$ and $1/2^+$, respectively. Thus, there are two channel spins in the elastic channel, *i.e.* $s = 2, 3$. Actually there are only minor differences between the R-matrix calculations with two different values.

Five resonances, *i.e.*, at E_x=5.11, 7.34, 7.71 MeV, and one doublet around 7.1 MeV, have been analyzed and the most probable fitting curves are shown in Fig. 6. It shows that the fitting results at scattering angle $\theta_{c.m.} \approx 152°$ are consistent with those at $\theta_{c.m.} \approx 175°$. For the well-known 5.11-MeV state, the input parameters are $J^\pi=2^+$, $\ell=0$, $\Gamma_p=45$ keV [15, 12, 18]. Unfortunately, the poor statistics around 6.15 MeV state prevent one making a reliable R-matrix fit. The enlarged individual R-matrix fits are shown in Fig. 7 explicitly. The results are discussed in the following subsections.
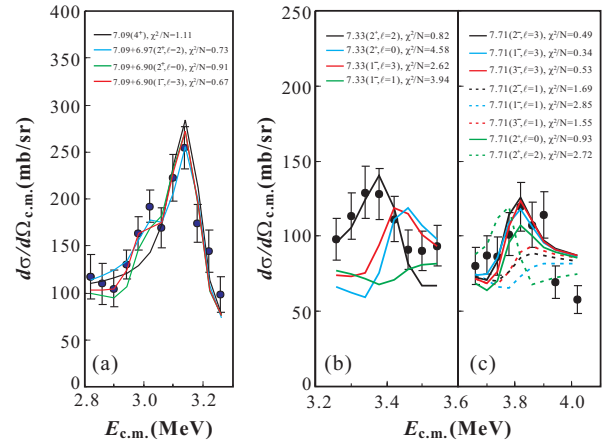
Figure 7: R-matrix fit results for the resonances at (a) around 7.1 MeV, (b) 7.33 MeV, and (c) 7.71 MeV, respectively. See text for details.

3.1 7.1 MeV doublet

This state was strongly populated by the $^{16}O(^3He,n)^{18}Ne$ reaction but not by the $^{20}Ne(p,t)^{18}Ne$ reaction [37, 12]. Nero *et al.* [37] observed a 7.06-MeV state ($\Gamma=180\pm50$ keV) ex-

hibiting $J^{\pi}=(1^-, 2^+)$ characters in the measured angular distribution, and thought 2^+ was a more admissible assignment based on a reaction-mechanism analysis. Hahn *et al.* [12] also observed a broad state at 7.07 MeV (Γ=200±40 keV), and a smaller fitting χ^2/N value could be achieved for a doublet at 7.05&7.12 MeV. In this work, the peak around 7.1 MeV exhibits also a doublet structure as shown in Fig. 7(a) where *R*-matrix fitting results for the doublets are better than that for a singlet. Now it can be concluded that one of the doublet, say, the latter 7.09-MeV state is of a 4^+ character based on the present and Harss *et al.*'s data [16], while the spin-parity of the former state in the doublet is not obvious yet. Two possible assignments (1^- or 2^+) proposed by Nero *et al.* [37] were attempted in the present *R*-matrix analysis. Two resonances at, *i.e.*, 6.97 MeV (2^+, ℓ=2) and 7.09 MeV (4^+, ℓ=2), can reproduce the data reasonably. A 120 keV gap between these two states is consistent with the previous 70 keV one (7.05&7.12 MeV) within the uncertainty. Although other $2^+(\ell$=0) and $1^-(\ell$=3) fits can reproduce the data as well, a large gap of 190 keV excludes these assignments. If taking the precise energies from Ref. [12], this doublet should be a state at 7.05 MeV (2^+) and another at 7.12 MeV (4^+). Furthermore, a fact that both 7.05- and 7.12-MeV states were observed in the previous thick-target (α, p) experiment [38, 39, 40] may probably indicates they are all natural parity states, and that is consistent with the present assignments.

3.2   7.35 MeV state

Previously, it was observed in the (^{3}He,n), (^{12}C,^{6}He) reactions [12] and showed (1^-, 2^+) characters in the measured (^{3}He,n) angular distribution. Hahn *et al.* [12] suggested a 1^- for this state based on a very simple mirror argument. Later, following Fortune and Sherr's arguments [17], Harss *et al.* [16] speculated it as a 2^+ state based on the Coulomb-shift discussion. Present data support the $2^+(\ell$=2) assignment rather than the 1^- one [12] as clearly shown in Fig. 7(b). The presently deduced energy of 7.33 MeV is consistent with the previous values (7.35 MeV in [12]) within the uncertainty.

3.3   7.71 MeV state

It was observed in the (^{3}He,n), (^{12}C,^{6}He) reactions but not in the (p,t) reaction, and behaved an unnatural parity character in the angular distribution [12]. In addition, it was also not observed in the (p,α) reaction [16]. Therefore, Harss *et al.* [16] assigned it as a unnatural 2^- state, and this assignment could reproduce their excitation function data although the structure was not evident in the measured energy region. The present *R*-matrix calculation gives three possible assignments (3^-, 2^-, 1^-) with ℓ=3, and hence the previous 2^- assignment is reasonable. The additional 2^+ fits are not very ideal as shown in Fig. 7(c). Actually, the fact that this state was not observed in the (α, p) reaction [38, 39, 40] and exhibited an unnatural character may exclude the 2^+ assignment as well.

3.4   7.60 MeV state

Previously, the 7.60-MeV state was assigned as a natural 1^- state because of its strong population in the ^{17}F(p,α)^{14}O reaction [16]. In this work, a 'groove-like' structure was observed at $E_{c.m.}$~3.6 MeV (*i.e.*, E_x~7.5 MeV) as seen in Fig. 6, and it possibly indicates the existence of a 1^- (ℓ=1) resonance which may show a 'groove' rather than a 'bump' structure in the ^{17}F+p excitation function [21]. While it's difficult to fit it reliably due to low statistics.

4   Astrophysical implication
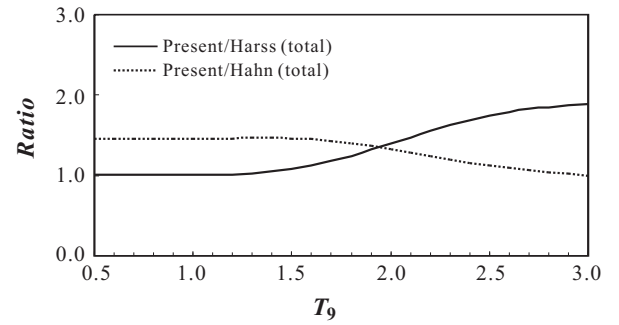
Figure 8: Calculated ratios between the present resonant reaction rates and those previous ones as a function of temperature. See text for details.

The astrophysical reaction rates for the ^{14}O(α,p)^{17}F reaction have been extensively studied by many works as cited in the introduction. As learned from Wiescher *et al.*'s work [9], its resonant reaction rates dominate the total rates above temperature ~0.25 GK, and hence the resonant reaction rates are actually the total ones beyond this temperature.

The resonant reaction rate (in units of cm^{3}s^{-1}mol^{-1}) has been calculated by using the isolated and narrow resonance formula [9, 16, 25, 26],

$$N_A\langle\sigma v\rangle_{\text{res}} = 1.54 \times 10^{11}(\frac{1}{\mu T_9})^{3/2}\Sigma_i(\omega\gamma)_i \times \exp(-\frac{11.605E_r^i}{T_9}), \quad (3)$$

where the E_r^i are the center-of-mass energies and the $(\omega\gamma)_i$ are the strengths of the resonances in MeV, the reduced mass μ in unit of amu. For this (α,p) reaction, because of $\Gamma_\alpha \ll \Gamma_p \approx \Gamma_{\text{tot}}$ [12, 16], the resonance strength is calculated by [26],

$$\omega\gamma = \omega\frac{\Gamma_\alpha\Gamma_p}{\Gamma_{\text{tot}}} \simeq (2J + 1)\Gamma_\alpha, \quad (4)$$

where J is spin of the resonance. The α-particle partial width can be expressed in a form of [12, 26]

$$\Gamma_\alpha \propto C^2S_\alpha \times P_\ell(E_r). \quad (5)$$

Table 1: Resonant parameters used in the reaction rate calculations for the stellar ^{14}O(α,p)^{17}F reaction.

E_x (MeV)			J^π			$\omega\gamma_{(\alpha,p)}$ (eV)		
Present[1]	Harss [16]	Hahn [12]	Present	Harss [16]	Hahn [12]	Present[2]	Harss [16]	Hahn [12]
6.15±0.02	6.15±0.02	6.15±0.02	1⁻	1⁻	1⁻	9.6^{+15}_{-6}	9.6^{+15}_{-6}	6.6
7.12±0.03	7.05±0.10	7.05±0.03	4⁺	4⁺	4⁺	1.5×(360±126)[3]	360±126	430
7.35±0.02	7.37±0.06	7.35±0.02	2⁺	2⁺	1⁻	200±150	200±150	4500
7.62±0.02	7.60±0.05		1⁻	1⁻		3000±360	3000±360	
7.05±0.03			2⁺			2.6×(360±126)[4]		

[1] The excitation energies and its errors are adopted from Ref. [12].
[2] The resonant strengths are adopted from Ref. [16] except for the 7.05&7.12 MeV states.
[3] A spectroscopic factor C^2S_α=0.11 is adopted for the 4⁺ state [12].
[4] A conservative spectroscopic factor C^2S_α=0.01 is assumed for the 2⁺ assignment [9].

Here C^2S_α is the α-particle spectroscopic factor [12], and the Coulomb penetrability factor P_ℓ is calculated by a `RCWFN` code [41] with an interaction radius of R=5.20 fm.
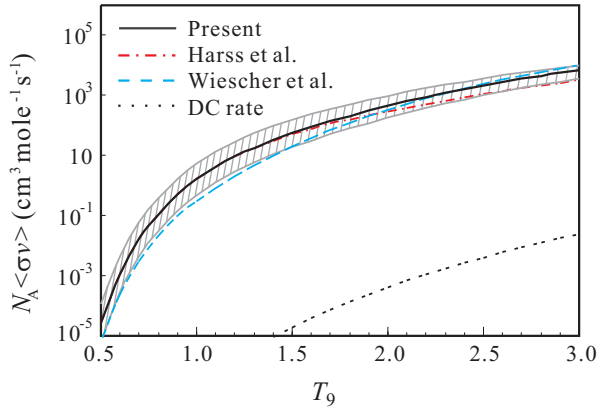
Figure 9: Calculated resonant reaction rates for the stellar ^{14}O(α,p)^{17}F reaction. Harss et al.'s rates [16], Wiescher et al.'s rates [9] as well as the direct capture (DC) rates [9], are also shown for comparison. The gray-shaded area represents the uncertainty in the present calculation.

For the 7.1-MeV broad state, a doublet structure has been considered in the present calculation, i.e., a state at 7.05 MeV (2⁺) and another at 7.12 MeV (4⁺) in comparison to a singlet [i.e., 7.05 MeV (4⁺)] used in the previous calculations [12, 16]. Although the resonance strength of the latter 7.12-MeV state (4⁺, E_r=2.01 MeV) is about a factor of $R=\frac{P_{\ell=4}(E_r=2.01)}{P_{\ell=4}(E_r=1.94)}\simeq1.5$ larger than that of the previous work [12, 16] in which an energy of 7.05 MeV (E_r=1.94 MeV) was used, the corresponding resonant rate ratio still remains about unity above ~2 GK because of the exponential term [exp(-11.605E_r/T_9)]. For the low-energy component 7.05-MeV (2⁺) state, a conservative spectroscopic factor C^2S_α(2⁺)=0.01 [9] is assumed in the present work while a

factor C^2S_α(4⁺)=0.11 [12] was adopted in the previous work. Thus, the resonance strength ratio between the 2⁺ and 4⁺ assignments can be expressed by

$$R = \frac{\omega(2^+)}{\omega(4^+)} \times \frac{C^2S_\alpha(2^+)}{C^2S_\alpha(4^+)} \times \frac{P_{\ell=2}(E_r=1.94)}{P_{\ell=4}(E_r=1.94)} \simeq 2.6. \quad (6)$$

This enhancement factor 2.6 could be even larger if 7.05-MeV (2⁺) state has a larger C^2S_α factor (note that a 2⁺, 5.260-MeV state in ^{18}O mirror has much larger factor, $C^2S_\alpha\geqslant0.04$ [9]).

Table 2: Total reaction rates of ^{14}O(α,p)^{17}F in units of cm³s⁻¹mol⁻¹.

T_9	Present	Harss et al. [16]	Hahn et al. [12]	Wiescher et al. [9]
0.5	2.75E-05	2.75E-05	1.89E-05	6.14E-06
0.6	1.15E-03	1.15E-03	7.91E-04	2.32E-04
0.7	1.60E-02	1.60E-02	1.10E-02	3.03E-03
0.8	1.12E-01	1.12E-01	7.70E-02	2.05E-02
0.9	4.99E-01	4.98E-01	3.43E-01	9.08E-02
1.0	1.62E+00	1.62E+00	1.11E+00	3.03E-01
1.2	9.32E+00	9.19E+00	6.38E+00	2.04E+00
1.4	3.26E+01	3.10E+01	2.23E+01	9.70E+00
1.6	8.68E+01	7.73E+01	6.00E+01	3.74E+01
1.8	2.00E+02	1.60E+02	1.43E+02	1.21E+02
2.0	4.18E+02	2.99E+02	3.17E+02	3.30E+02
2.5	1.94E+03	1.11E+03	1.73E+03	2.35E+03
3.0	6.11E+03	3.25E+03	6.12E+03	9.77E+03

Total resonant reaction rate of ^{14}O(α,p)^{17}F has been calculated with those resonances listed in Table 1. It should be noted that contribution from the 6.286-MeV state is negligible [18] and neglected in the present calculation. In addition, the energy of 7.71-MeV state is too high to contribute to the rate considerably, and it is unable to contribute to the rate because of its unnatural parity as well. The present parameters for resonant energies and errors are adopted from Hahn et al.'s work [12] where the excitation energies in ^{18}Ne are determined precisely, while those for resonant strengths and errors are adopted from Harss et al.'s work [16] where the

strengths were determined experimentally. The total resonant reaction-rate ratios between the present and the previous ones are shown in Fig. 8. It shows that the present rates are generally larger than the previous ones. For instance, it is about a factor of 1.4 larger than Hahn *et al.*'s rate below 2.0 GK mainly because of a larger strength value for the 6.15-MeV state used in the present calculation; and it is about factors of 1.2~1.9 larger than Harss *et al.*'s rate in temperature region of 1.7~3.0 GK mainly owing to a low-energy component of the 7.1-MeV doublet (*i.e.*, 7.05 MeV, 2^+ state) involved in the present calculation.

The total reaction rates are shown in Fig. 9 in the temperature region of 0.5~3.0 GK with the numerical values listed in Table 2. The associated uncertainties are indicated as the gray-shaded area, where both the uncertainties of resonant energy and strengths are included in the calculation (see Table 1). The previous Harss *et al.*'s rates are shown for comparison. The direct capture (DC) rates are negligible comparing to the resonant ones as shown in the figure. In addition, the Wiescher *et al.*'s rates [9] are also calculated for comparison. It shows that Wiescher *et al.*'s rates are out of the present uncertainty below ~1.5 GK mainly because a 1^- resonance state was predicted at 6.125 MeV based on a Thomas-Ehrman shift calculation.

5 Summary

We have investigated the proton resonant properties in ^{18}Ne through an elastic scattering of ^{17}F+p by using a radioactive beam of ^{17}F bombarding a thick hydrogen target. The resonance parameters have been determined by the *R*-matrix analysis of the *c.m.* differential cross sections A better fitting can be achieved for a 7.1-MeV doublet which most probably contains a state at 7.05 MeV (2^+) and another at 7.12 MeV (4^+). As for the stellar ^{14}O(α,p)^{17}F reaction, the resonant rates attributed from this doublet will be enhanced considerably in comparison to the previous singlet assignment. It indicates that this doublet will contribute more to the total rate at relatively low temperature region in which the 6.15-MeV state was previously thought to be dominant. The present total rates are at least a factor of 1.2~1.9 larger than Harss *et al.*'s rates around ~2 GK mainly because of contribution from the 7.05-MeV (2^+) state. It should be noted that spin-parities for the 6.15- and 6.286-MeV states are still not determined very well [21], and hence the associated uncertainty isn't included in the present calculation yet. As a suggestion, additional high-precision and high-statistics experiments are still needed to determine those resonant parameters, and it will help us to deeply understand the role of breakout ^{14}O(α,p)^{17}F reaction occuring in the stellar x-ray bursters.

References

[1]. S.E. Woosley and R.E. Taam, Nature **263**, 101 (1976).

[2]. A.E. Champage and M. Wiescher, Annu. Rev. Nucl. Part. Sci. **42**, 39 (1992).

[3]. M. Wiescher, H. Schatz, and A.E. Champagne, Phil. Trans. R. Soc. A **356**, 2105 (1998).

[4]. R.E. Taam, Annu. Rev. Nucl. Part. Sci. **35**, 1 (1985).

[5]. D.W. Bardayan *et al.*, Phys. Rev. C **62**, 055804 (2000).

[6]. H. Schatz *et al.*, Phys. Rep. **293**, 167 (1998).

[7]. H. Schatz *et al.*, Phys. Rev. Lett. **86**, 3471 (2001).

[8]. M. Breitenfeldt *et al.*, Phys. Rev. C **80**, 035805 (2009).

[9]. M. Wiescher *et al.*, Astrophys. J. **316**, 162 (1987).

[10]. C. Funck and K. Langanke, Nucl. Phys. A **480**, 1888 (1988).

[11]. C. Funck, B. Grund, and K. Langanke, Z. Phys. A **332**, 109 (1989).

[12]. K.I. Hahn *et al.*, Phys. Rev. C **54**, 1999 (1996).

[13]. G. Audi, A.H. Wapstra and C. Thibault, Nucl. Phys. A **729**, 337 (2003).

[14]. B. Harss *et al.*, Phys. Rev. Lett. **82**, 3964 (1999).

[15]. J. Gómez del Campo *et al.*, Phys. Rev. Lett. **86**, 43 (2001).

[16]. B. Harss *et al.*, Phys. Rev. C **65**, 035803 (2002).

[17]. H.T. Fortune and R. Sherr, Phys. Rev. Lett. **84**, 1635 (2000).

[18]. J.J. He *et al.*, Phys. Rev. C **80**, 042801(R) (2009).

[19]. J.J. He *et al.*, Nucl. Phys. A **834**, 670(c) (2010).

[20]. J.C. Blackmon *et al.*, Nucl. Phys. A **718**, 127(c) (2003).

[21]. J.J. He *et al.*, arXiv:1001.2053v1 [astro-ph.SR], (2010).

[22]. K.P. Artemov *et al.*, Sov. J. Nucl. Phys. **52**, 408 (1990).

[23]. S. Kubono, Nucl. Phys. A **693**, 221 (2001).

[24]. T. Teranishi *et al.*, Phys. Lett. B **650**, 129 (2007).

[25]. J.J. He *et al.*, Phys. Rev. C **76**, 055802 (2007).

[26]. J.J. He *et al.*, Phys. Rev. C **80**, 015801 (2009).

[27]. J.W. Xia *et al.*, Nucl. Instr. and Meth. Phys. Res. A **488**, 11 (2002).

[28]. W.L. Zhan *et al.*, Nucl. Phys. A **834**, 694(c) (2010).

[29]. Z. Sun *et al.*, Nucl. Instr. and Meth. A **503**, 496 (2003).

[30]. P. Ma *et al.*, Atomic Energy Sci. and Tech. (2010), in press.

[31]. Micron Semiconductor Ltd., Lancing, UK. Please see: http://www.micronsemiconductor.co.uk/.

[32]. J.F. Ziegler *et al.*, *The Stopping and Range of Ions in Solids*, Pergamon Press, New York, 1985.

[33]. A.M. Lane and R.G. Thomas, Rev. Mod. Phys. **30**, 257 (1958).

[34]. P. Descouvemont, *Theoretical Models for Nuclear Astrophysics*, Nova Science Publishers Inc., New York, 2003.

[35]. C.R. Brune, Phys. Rev. C **66**, 044611 (2002).

[36]. A.St.J. Murphy *et al.*, Phys. Rev. C **79**, 058801(2009).

[37]. A.V. Nero, E.G. Adelberger and F.S. Dietrich, Phys. Rev. C **24**, 1864 (1981).

[38]. M. Notani *et al.*, Nucl. Phys. A **738**, 411(c) (2004).

[39]. M. Notani *et al.*, Nucl. Phys. A **746**, 113(c) (2004).

[40]. S. Kubono *et al.*, Eur. Phys. J. A **27**, 327 (2006).

[41]. A.R. Barnett *et al.*, Comput. Phys. Commun. **8**, 377 (1974).

Development of a Lorentzian-Function Approximation utilizing in the charged-particle-induced non-resonant reaction rate

J.J. He[1], L. Li[1,2], J. Hu[1], L.Y. Zhang[1,2], S.W. Xu[1], X.Q. Yu[1] & M.L. Liu[1]

[1]Institute of Modern Physics, Chinese Academy of Sciences (CAS), Lanzhou 730000, China
[2]Graduate School of Chinese Academy of Sciences, Beijing 100049, China

A development has been made for the charged-particle-induced non-resonant reaction-rate equations. The forms of reaction-rate equations for non-resonant and resonant reactions have been united in a frame of Lorentzian-Function Approximation (LFA) mathematically. In the frame of LFA, the non-resonant reaction taken place within the Gamow window can be considered, in form, as a "resonance" reaction with a full width at half maximum (FWHM, Γ^{nr}) equal to the $1/e$ width (Δ) in a well-known Gaussian-Function Approximation (GFA).

1 Introduction

It is well-known that nuclear reactions play a dominant role in energy production and element synthesis in most astrophysical sites. In order to interpret those appealing astrophysical phenomena, a huge amount of nuclear physics information is required in the astrophysical models as input. Thereinto the reaction rate, which is defined as how fast a reaction takes place, is one of the most critical inputs [1, 2, 3]. As we know a narrow-resonance reaction can be well described by a Lorentzian-shape function, and recently a Lorentzian-Function Approximation (LFA) has been developed for calculating the non-resonant reaction rate [4], and hence it's possible to unite the forms of reaction-rate equations for non-resonant and resonant reactions in one frame together. This work aims at addressing this unification carefully. In order to make readers easy to follow, the exactly same notations and definitions utilized in Ref. [3] are being adopted here.

2 Gaussian-Function Approximation (GFA)

It is well known the reaction rate per particle pair $\langle \sigma v \rangle$ can be written in the form of Equ. (4.17) in Ref. [3], i.e.,

$$\langle \sigma v \rangle = \left(\frac{8}{\pi \mu}\right)^{1/2} \frac{1}{(kT)^{3/2}} \int_0^\infty S(E)\exp\left[-\frac{E}{kT} - \frac{b}{E^{1/2}}\right]dE. \quad (1)$$

For a given stellar temperature T, nuclear reactions take place in a relatively narrow energy window around the effective burning energy of E_0 (See Fig. 4.6 in Ref. [3] and the present Fig. 1).

Frequently, the $S(E)$ factor is nearly a constant over the window,

$$S(E) = S(E_0) = \text{const.}.$$

In this condition, Equ. 1 reduces to

$$\langle \sigma v \rangle = \left(\frac{8}{\pi \mu}\right)^{1/2} \frac{1}{(kT)^{3/2}} S(E_0) \int_0^\infty \exp\left[-\frac{E}{kT} - \frac{b}{E^{1/2}}\right]dE. \quad (2)$$

Although the integration can be computed by the numerical method readily, a Gaussian-Function Approximation (GFA) for the integrand in Equ. 2 had been used in order to make the physics clear (e.g., see Refs. [2, 3]). Briefly, the exponential term in the integrand can be fairly well approximated by a Gaussian function:

$$\exp\left(-\frac{E}{kT} - \frac{b}{E^{1/2}}\right) = I_{\max}\exp\left[-\left(\frac{E - E_0}{\Delta/2}\right)^2\right], \quad (3)$$

here $I_{\max}=\exp(-\tau)$ with $\tau=\frac{3E_0}{kT}$. In this GFA approximation, the Gamow-peak energy is given by

$$E_0 = \left(\frac{bkT}{2}\right)^{2/3} = 1.22(Z_1^2 Z_2^2 \mu T_6^2)^{1/3}(\text{keV}),$$

the $1/e$ width of the peak is defined as the effective width Δ of the energy window, wherein most of the reactions take place. This width is determined by matching the second derivative of Equ. 3, i.e.,

$$\Delta = \frac{4}{3^{1/2}}(E_0 kT)^{1/2} = 0.749(Z_1^2 Z_2^2 \mu T_6^5)^{1/6}(\text{keV}).$$

Actually the quantity ΔE_0 indicated on the Figure 4.6 [3] is improper, and it should be the $1/e$ width rather than the full

width at half maximum (FWHM) of the Gamow peak. With GFA in Equ. 3, the reaction rate becomes

$$
\begin{aligned}
\langle \sigma v \rangle &\simeq \left(\frac{8}{\pi\mu}\right)^{1/2} \frac{1}{(kT)^{3/2}} S(E_0) \int_{-\infty}^{\infty} I_{\max} \exp\left[-\left(\frac{E-E_0}{\Delta/2}\right)^2\right] dE \\
&= \left(\frac{2}{\mu}\right)^{1/2} \frac{\Delta}{(kT)^{3/2}} S(E_0) \exp\left(-\frac{3E_0}{kT}\right)
\end{aligned}
\tag{4}
$$

by using a result of Gaussian integration:

$$
\int_{-\infty}^{\infty} e^{-ax^2} dx = \sqrt{\pi/a}.
$$

It should be noted that the exact derivation of Equ. 4 (*i.e.,* Equ. (4.27) in Ref. [3]) requires the lower-limit of integration to be set as $-\infty$, although it is not necessarily so small, *e.g.,* $-E_0$ is small enough. As discussed in the literature [2, 3], the exact form of $\exp\left(-\frac{E}{kT} - \frac{b}{E^{1/2}}\right)$ is slightly asymmetric around the energy E_0 compared with the Gaussian distribution. This general feature of the Gamow peak can be accounted for when calculating the integral in Equ. 2 by the factor $F(\tau)$:

$$
F(\tau) = 1 + \frac{5}{12}\frac{1}{\tau} - \frac{35}{288}\frac{1}{\tau^2} + \cdots,
$$

where in general the correction provided by the $1/\tau$ is sufficient [3]. Generally speaking this correction is very small, *e.g.,* in first order (at $T_6=15$)

$$
\begin{aligned}
p + p &: \quad F(\tau) = 1.030, \\
{}^{16}O + {}^{16}O &: \quad F(\tau) = 1.00076.
\end{aligned}
$$

If the $S(E)$ factor is described by a slowly varying function of energy E rather than by a constant, it can be expanded in a Taylor series,

$$
S(E) = S(0) + \dot{S}(0)E + \frac{1}{2}\ddot{S}(0)E^2 + \cdots.
$$

As a result of GFA, one can replace the constant $S(E_0)$ factor in Equ. 4 in Ref. [3]) by an effective S-factor [1, 3]:

$$
\begin{aligned}
S_{\mathrm{eff}}(E_0) = S(0)&\left[1 + \frac{5}{12\tau} + \frac{\dot{S}(0)}{S(0)}\left(E_0 + \frac{35}{36}kT\right)\right] \\
&+ S(0)\left[\frac{1}{2}\frac{\ddot{S}(0)}{S(0)}\left(E_0^2 + \frac{89}{36}E_0kT\right)\right].
\end{aligned}
\tag{5}
$$
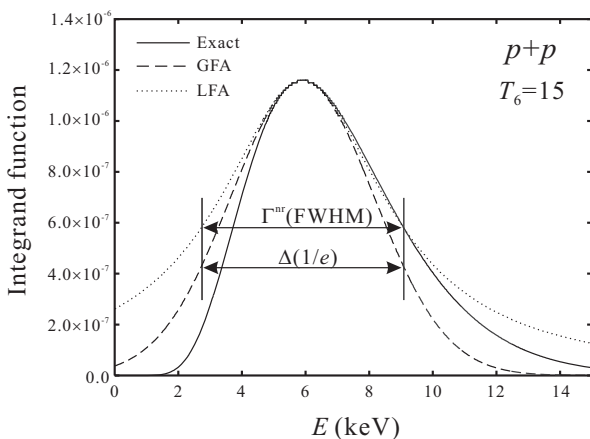
Figure 1: Curves for the Gamow peak for the $p+p$ reaction at $T_6=15$, as obtained from an exact expression and from a Gaussian-Function Approximation (GFA) as well as a Lorentzian-Function Approximation (LFA). Here, $E_0=5.89$ keV with $\Gamma^{\mathrm{nr}} = \Delta=6.37$ keV.

3 Lorentzian-Function Approximation (LFA)

In a recent work [4], a Lorentzian-Function Approximation (LFA) has been used to obtain some similar equations as those deduced from GFA. In the LFA frame, the integrand in Equ.2 can be expressed by

$$
\exp\left(-\frac{E}{kT} - \frac{b}{E^{1/2}}\right) = I_{\max}\frac{(\Gamma^{\mathrm{nr}}/2)^2}{(E-E_0)^2 + (\Gamma^{\mathrm{nr}}/2)^2}.
\tag{6}
$$

Similarly, the FWHM width of this Lorentzian function, Γ^{nr}, can be determined by matching the second derivative of Equ. 6, with a result of $\Gamma^{\mathrm{nr}} = \Delta$ as shown in Fig. 1. The reaction rate equation then becomes

$$
\begin{aligned}
\langle \sigma v \rangle &\sim \left(\frac{8}{\pi\mu}\right)^{1/2} \frac{1}{(kT)^{3/2}} S(E_0) \int_{-\infty}^{\infty} I_{\max}\frac{(\Gamma^{\mathrm{nr}}/2)^2}{(E-E_0)^2 + (\Gamma^{\mathrm{nr}}/2)^2} \\
&= \sqrt{\pi} \times \left(\frac{2}{\mu}\right)^{1/2} \frac{\Gamma^{\mathrm{nr}}}{(kT)^{3/2}} S(E_0)\exp\left(-\frac{3E_0}{kT}\right).
\end{aligned}
\tag{7}
$$

It is obviously that the rate calculated by Equ. 7 is overestimated by a factor of $\sqrt{\pi}$ compared to that calculated by GFA (Equ. 4). Similar to GFA, a correction factor $L(\tau)$ is introduced here to account for the feature of Gamow peak, and simply

$$
L(\tau) = \frac{1}{\sqrt{\pi}}F(\tau).
$$

Therefore, the reaction rate $\langle \sigma v \rangle$ can be written in the same form (*i.e.,* Equ. (4.32) in Ref. [3]) with respect to GFA and LFA,

$$
\langle \sigma v \rangle = \left(\frac{2}{\mu}\right)^{1/2} \frac{\Gamma^{\mathrm{nr}}(\mathrm{or}\Delta)}{(kT)^{3/2}} S(E_0)(1 + \frac{5}{12\tau})\exp(-\tau).
\tag{8}
$$

In addition, as a result of LFA, one can obtain

$$
\begin{aligned}
S_{\mathrm{eff}}^{\mathrm{LFA}}(E_0) &= S(0)\left\{1 + \frac{\dot{S}(0)}{S(0)}E_0 + \frac{1}{2}\frac{\ddot{S}(0)}{S(0)}\left[E_0^2 + \left(\frac{\Gamma^{\mathrm{nr}}}{2}\right)^2\right]\right\}\left(1 + \frac{5}{12\tau}\right) \\
&= S(0)\left[1 + \frac{5}{12\tau} + \frac{\dot{S}(0)}{S(0)}\left(E_0 + \frac{5}{36}kT\right) + \frac{1}{2}\frac{\ddot{S}(0)}{S(0)}\left(E_0^2 + \frac{53}{36}E_0kT\right)\right].
\end{aligned}
\tag{9}
$$

when the $S(E)$ factor is a slowly varying function of energy. For general case $kT \ll E_0$, the difference between the present derived effective S-factor [$S_{\mathrm{eff}}^{\mathrm{LFA}}(E_0)$] and previously derived one (Equ. 5) is quite small.

4 Unification

In the frame of LFA, the reaction rate equation (Equ. 8) can be alternatively written as

$$\langle \sigma v \rangle = \left(\frac{2}{\mu}\right)^{1/2} \frac{\Gamma^{\text{nr}}}{(kT)^{3/2}} S_{\text{eff}}(E_0) \exp(-\tau) \qquad (10)$$

$$= \left(\frac{2\pi}{\mu kT}\right)^{3/2} \hbar^2 \left[\frac{\mu S_{\text{eff}}}{2\pi^{3/2}\hbar^2} \exp\left(-\frac{2E_0}{kT}\right)\Gamma^{\text{nr}}\right] \exp\left(-\frac{E_0}{kT}\right).$$

Thus, in comparison with that for an isolated narrow resonance, *i.e.*,

$$\langle \sigma v \rangle = \left(\frac{2\pi}{\mu kT}\right)^{3/2} \hbar^2 (\omega\gamma)_R \exp\left(-\frac{E_R}{kT}\right), \qquad (11)$$

a non-resonant reaction can be regarded as a "resonant" one in form, the corresponding "resonant" energy (E^{nr}), width (Γ^{nr}), and strength (($\omega\gamma)^{\text{nr}}$) are, $E^{\text{nr}} = E_0$, $\Gamma^{\text{nr}} = \Delta$, and

$$(\omega\gamma)^{\text{nr}} = \frac{\mu S_{\text{eff}}}{2\pi^{3/2}\hbar^2} \exp\left(-\frac{2E_0}{kT}\right)\Gamma^{\text{nr}},$$

respectively. Hence, the total reaction-rate equation for the non-resonant and resonant contributions can be expressed as

$$\langle \sigma v \rangle = \left(\frac{2\pi}{\mu kT}\right)^{3/2} \hbar^2$$
$$\times \left[(\omega\gamma)^{\text{nr}}\exp\left(-\frac{E_0}{kT}\right) + (\omega\gamma)_R\exp\left(-\frac{E_R}{kT}\right)\right]. (12)$$

Thus, the forms of reaction-rate equations for non-resonant and resonant reactions have been united in one framework of LFA.

5 Summary

A Lorentzian-Function Approximation (LFA) has been developed in calculating the non-resonant reaction rate of charged-particle-induced reactions. The forms of reaction-rate equations for non-resonant and resonant reactions have been united in a frame of Lorentzian-Function Approximation (LFA) mathematically. In the LFA frame, the non-resonant reaction taken place within the Gamow window can be considered, in form, as a "resonance" reaction with a FWHM width equal to the $1/e$ width in a well-known Gaussian-Function Approximation (GFA).

References

[1]. W.A. Fowler, G.R. Caughlan, and B.A. Zimmerman, *Ann. Rev. Astron. Astrophys.* **5** (1967) 525.

[2]. D.D. Clayton, *Principles of Stellar Evolution and Nucleosynthesis*, (University of Chicago Press, Chicago, 1983).

[3]. C.E. Rolfs and W.S. Rodney, *Cauldrons in the Cosmos*, (University of Chicago Press, Chicago, 1988).

[4]. J.J. He, *Eur. Phys. J. A* **33** (2007) 5.

Reexamination of astrophysical resonance-reaction-rate equations for an isolated, narrow resonance

J.J. He[1], J. Hu[1], L.Y. Zhang[1,2], L. Li[1,2], S.W. Xu[1], X.Q. Yu[1] & M.L. Liu[1]

[1]*Institute of Modern Physics, Chinese Academy of Sciences (CAS), Lanzhou 730000, China*
[2]*Graduate School of Chinese Academy of Sciences, Beijing 100049, China*

The well-known astrophysical resonant-reaction-rate (RRR) equations for an isolated narrow resonance induced by the charged particles have been reexamined. The validity of those assumptions used in deriving the classical analytic equations has been checked, and found that these analytic equations only hold for certain circumstances. It shows the customary definition of 'narrow' is inappropriate or ambiguous in some sense, and it awakes us not to use those analytic equations without caution. As a suggestion, it's better to use the broad-resonance equation to calculate the RRR numerically even for a narrow resonance of a few keV width. The present conclusion may influence some work in which the classical narrow-resonant equations were used for calculating the RRRs, especially at low stellar temperatures for those previously defined 'narrow' resonances.

1 Introduction

Nuclear astrophysics can address some of the most remarkable questions in nature: What are the origins of the elements making life on earth possible? How did the sun, the solar system, and the stars form and evolve? and so on and so forth. In order to answer these questions, a huge amount of nuclear physics information is required in the astrophysical models as input. Thereinto the reaction rate, which is defined as how fast a reaction takes place, is one of the most critical ones. It reflects most of the critical stellar features, *e.g.*, time scale, energy production and nucleosynthesis of the elements as well as, *etc.*. Nuclear astrophysics has been developed for more than 50 years, and a great number of stellar reaction rates have been calculated by utilizing the classical equations based on the experimental data.

This work is focusing on the validity of resonant-reaction-rate (hereafter referred to as RRR) equations for an isolated narrow resonance induced by the charged particles. Actually these equations have been derived in many books or references [1, 2, 3]. As an example, let's thumb through the famous Book "*Cauldrons in the Cosmos*" [3]. To make readers easy to follow, a similar deriving procedure and the same notations used in Ref. [3] are being adopted here.

It is well-known the stellar reaction rate per particle pair $\langle \sigma v \rangle$ can be expressed as (Eq. (4.1) in Ref. [3]),

$$\langle \sigma v \rangle = \left(\frac{8}{\pi\mu}\right)^{1/2} \frac{1}{(kT)^{3/2}} \int_0^\infty \sigma(E) E \exp\left(-\frac{E}{kT}\right) dE. \quad (1)$$

As for an isolated resonance the cross section can be ex-

pressed by a famous Breit-Wigner formula as (Eq. (4.52) in Ref. [3])

$$\sigma(E)_{BW}^N = \pi\left(\frac{\lambda}{2\pi}\right)^2 \frac{2J+1}{(2J_1+1)(2J_2+1)}(1+\delta_{12})$$
$$\times \frac{\Gamma_a \Gamma_b}{(E-E_R)^2 + (\Gamma/2)^2}. \quad (2)$$

According to the energy dependence of the cross section for a narrow resonance ($\Gamma \ll E_R$), Eq. 1 of the stellar RRR per particle pair can be replaced by

$$\langle \sigma v \rangle = \left(\frac{8}{\pi\mu}\right)^{1/2} \frac{1}{(kT)^{3/2}} \int_0^\infty \sigma(E)_{BW}^N E \exp\left(-\frac{E}{kT}\right) dE. \quad (3)$$

Assuming the Maxwell-Boltzmann function $E\exp(-E/kT)$ changing very little over the resonance region (hereafter referred to as "the FIRST assumption"), Eq. 3 can be written in a form of (*i.e.*, Eq. (4.53) in Ref. [3]),

$$\langle \sigma v \rangle = \left(\frac{8}{\pi\mu}\right)^{1/2} \frac{1}{(kT)^{3/2}} E_R \exp\left(-\frac{E_R}{kT}\right) \int_0^\infty \sigma(E)_{BW}^N dE. \quad (4)$$

And thus for a narrow resonance with $\left(\frac{\lambda}{2\pi}\right)^2 \simeq \left(\frac{\lambda}{2\pi}\right)_R^2$ (hereafter referred to as "the SECOND assumption"), the integration of the Breit-Wigner cross section can be written as (*i.e.*, Eq. (4.54) in Ref. [3]),

$$\int_0^\infty \sigma(E)_{BW}^N dE = \pi\left(\frac{\lambda}{2\pi}\right)_R^2 \omega \Gamma_a \Gamma_b \int_0^\infty \frac{1}{(E-E_R)^2 + (\Gamma/2)^2}$$
$$= 2\pi^2 \left(\frac{\lambda}{2\pi}\right)_R^2 \omega \frac{\Gamma_a \Gamma_b}{\Gamma}. \quad (5)$$

Where $\omega\gamma=\omega\frac{\Gamma_a\Gamma_b}{\Gamma}$ is defined as the resonance strength. Here, the energy dependence of the partial and total widths was neglected for a narrow resonance (hereafter referred to as "the THIRD assumption") Finally, the RRR per particle pair for an isolated narrow resonance can be written as

$$\langle\sigma v\rangle = \left(\frac{2\pi}{\mu kT}\right)^{3/2}\hbar^2(\omega\gamma)_R\exp\left(-\frac{E_R}{kT}\right). \qquad (6)$$

This classical analytic Eq. 6 is so famous that it has been utilized in a great number of nuclear astrophysics work (*e.g.*, see Refs. [5, 6, 7]).

After a careful survey, we find the definition and border of narrow and broad resonances in the previous literature are not quite clear. For instance, the statement "a resonance for which $\Gamma/E_R\geqslant 10$ % is called a broad resonance" [3] maybe mislead that a resonance with $\Gamma/E_R<10$ % can be treated as a narrow one. In the present work, we will examine the validity of all three assumptions mentioned above.
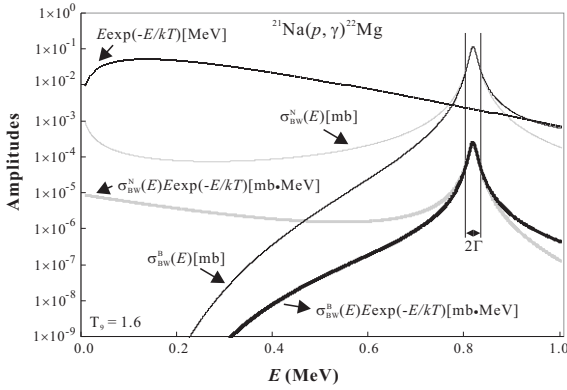
Figure 1: Amplitudes of relevant functions used in the equations. The units are included in the square brackets. See text for details.

2 Validity of Assumptions

The FIRST assumption A resonance for which $\Gamma/E_R<10$ % can be treated as a narrow resonance (*e.g.*, see Ref. [3]), here it shows this definition of 'narrow' is inappropriate especially at low temperatures. If one defines the variation δ_{MB} of the Maxwell-Boltzmann function $f_{MB} = E\exp(-E/kT)$ over the resonance region as

$$\begin{aligned}\delta_{MB} &= \frac{f_{MB}(E_R) - f_{MB}(E_R + \Gamma/2)}{f_{MB}(E_R)} \\ &= 1 - \frac{E_R + \Gamma/2}{E_R}\exp\left(-\frac{E_R + \Gamma/2 - E_R}{kT}\right) \\ &= 1 - \left(1 + \frac{\Gamma/2}{E_R}\right)\exp\left(-\frac{\Gamma}{2kT}\right),\end{aligned}$$

then δ_{MB} may be large at certain circumstances (*e.g.*, assuming a resonance with Γ=16 keV and $\frac{\Gamma}{E_R}$=10 %, $\delta_{MB}\approx 59$ %,

17 % at $T = 0.1, 0.4$ GK, respectively). Clearly, the variation δ_{MB} exponentially depends on the stellar temperature, and therefore this assumption is not a good one for low temperatures. From the definition of δ_{MB}, another complementary restriction for a narrow resonance should be expressed as $\Gamma \leqslant \frac{T_9}{11.608}\ln\frac{1+\frac{\Gamma/2}{E_R}}{1-\delta_{MB}}$ (Γ in unit of MeV). For instance, with δ_{MB}=5 % and $\Gamma/E_R<10$ %, another restriction for width is $\Gamma \leqslant 0.017\,T_9$ MeV. It should be noted that in some literature a definition of 'narrow' was $\Gamma\ll E_R$, but its ambiguity may give rise to certain misleading in some sense.

The SECOND assumption The de Broglie wavelength squared $(\frac{\lambda}{2\pi})^2$ $(=\frac{\hbar^2}{2\mu E})$ is inversely proportional to the center-of-mass energy E, and therefore this assumption $(\frac{\lambda}{2\pi})^2\simeq(\frac{\lambda}{2\pi})_R^2$ means $E\simeq E_R$ over the resonance region. It's a reasonable assumption for a resonance with $\Gamma/E_R<10$ %.

The THIRD assumption The partial width for a charged particle a (usually either proton or α particle) is strongly energy dependent because the projectile must penetrate the Coulomb barrier, and can be defined as (Eq. (4.65) in Ref. [3])

$$\Gamma_a = \frac{2\hbar}{R_n}\left(\frac{2E}{u}\right)^{\frac{1}{2}}P_\ell\theta_\ell^2,$$

where the penetration factor can be calculated by $P_\ell=\frac{1}{(F_\ell^2+G_\ell^2)}$ [4] with the regular and irregular Coulomb wave functions F_ℓ, G_ℓ. The quantity θ_ℓ^2, called the dimensionless reduced width of a nuclear state, is generally determined experimentally and contains the nuclear structure information. Generally speaking, θ_ℓ^2 is independent of energy E. Here, for simplicity, only *s*-wave case has been discussed. Therefore, it is sufficient to use the expression $\Gamma_a=c_1\sqrt{E}P_{\ell=0}(E)\propto\sqrt{E}e^{-2\pi\eta}$, where the penetration factor $P_{\ell=0}$ for the Coulomb barrier is approximated by a Gamow factor [3]. The quantity c_1 depends on the nuclear structure of the resonance. The exponent is $2\pi\eta=c_2\sqrt{1/E}$ with c_2=31.29$Z_1Z_2\sqrt{\mu}$ depending on the projectile-target combination. Note only in this equation the center-of-mass energy E is given in units of keV. On the other hand, γ-ray partial widths depend only weakly on the energy via $\Gamma_\gamma=c_3E_\gamma^{2L+1}\propto(E+Q)^{2L+1}$, where E_γ and L are the energy and multipolarity, respectively, of the γ-ray transition under consideration, and Q is the reaction Q-value. The quantity c_3 depends on the nuclear structure of the two levels involved in the interaction. Therefore, for the usual particle-gamma reaction channel (*e.g.*, (p,γ) or (α,γ)), the variation of quantity $\Gamma_a\Gamma_\gamma$ $(\propto\sqrt{E}(E+Q)^{2L+1}e^{-c_2\sqrt{1/E}})$ over the resonance region can be expressed as

$$\begin{aligned}\delta_{\Gamma_a\Gamma_\gamma} &= \frac{\Gamma_a(E_R+\Delta E)\times\Gamma_\gamma(E_R+\Delta E)}{\Gamma_a(E_R)\times\Gamma_\gamma(E_R)} \\ &= \sqrt{1+\Delta E/E_R}\times\left(1+\frac{\Delta E}{E_R+Q}\right)^{2L+1}\times\exp^{-\frac{c_2}{\sqrt{E_R}}\left(\frac{1}{\sqrt{1+\Delta E/E_R}}-1\right)}.\end{aligned}$$

Here, ΔE defines the energy interval between the resonance energy E_R and the energies where the Maxwell-Boltzmann function crossing the Breit-Wigner function. It is obvious that the dominate variation takes place in the third exponential term. Given a condition of $\Delta E/E_R = 5$ %, for $p(p,\gamma)$ reaction, $\delta_{\Gamma_a\Gamma_\gamma}$ are only about 8%, 5%, 4% for resonances at E_R=0.1, 0.5, 1.0 MeV, respectively; while for $^{12}C(p,\gamma)$ reaction, $\delta_{\Gamma_a\Gamma_\gamma}$ are respectively increased to 58%, 24%, 18% for the above resonance energies. Clearly the variation $\delta_{\Gamma_a\Gamma_\gamma}$ is very sensitive to the projectile-target combination via quantity c_2. Therefore, the THIRD assumption is appropriate only for certain projectile-target combinations for a resonance with $\Gamma/E_R<10$ %.

Actually, the RRR per particle pair for a narrow resonance can be directly written as (use Eqs. 2 & 3)

$$\langle \sigma v \rangle = \quad \sqrt{2\pi} \frac{\hbar^2 \omega}{(\mu kT)^{3/2}}$$
$$\times \int_0^\infty \exp\left(-\frac{E}{kT}\right) \frac{\Gamma_a \Gamma_b}{(E-E_R)^2 + (\Gamma/2)^2} dE. \quad (7)$$

If one assumes quantity $\exp(-E/kT)$ as a constant over the resonance region, Eq. 7 is equivalent to Eq. 6. But, obviously this is not a good assumption for certain circumstances (see discussion for the FIRST assumption). As a conclusion, except the SECOND reasonable assumption, the FIRST and THIRD assumptions only hold for certain circumstances.

Now, let's turn to Eq. 5. Here an approximation (*i.e.*, $\arctan(\frac{E_R}{\Gamma/2}) \simeq \frac{\pi}{2}$) was utilized, and hence one can get

$$\int_0^\infty \frac{1}{(E-E_R)^2 + (\Gamma/2)^2} dE \simeq \frac{\pi}{\Gamma/2}.$$

This approximation causes about a 3% error for a condition of $\Gamma/E_R= 10$%, and thus it can be regarded as a reasonable one. The integration ranges, from 0 to ∞, were used in Eq. 5, and therefore the quantity $\Gamma_a\Gamma_b$ can't be considered as a constant and taken outside the integral. The quantity $\Gamma_a\Gamma_b$ can be roughly considered as a constant over a very narrow energy interval, and therefore the integration ranges on Eq. 5 should be physically restricted [7]. A general equation has been derived here,

$$\int_{E_R-n\frac{\Gamma}{2}}^{E_R+n\frac{\Gamma}{2}} \frac{1}{(E-E_R)^2 + (\Gamma/2)^2} dE = \frac{2}{\Gamma/2}\arctan(n). \quad (8)$$

Ratios between the values of quantity $\frac{\pi}{\Gamma/2}$ and those of quantity $\frac{2}{\Gamma/2}\arctan(n)$ are 0.5, 0.7, 0.8 for n=1,2,4, respectively. For a small value of n, the derivation of Eq. 5 is inappropriate in the integration-range point of view; while for a large n, although the difference becomes small, the above-mentioned assumptions might be inappropriate in the 'narrow' point of view. Therefore, the classical analytic Eqs. 4-6 are suggested not to be utilized in the future RRR calculations without caution.

3   Numerical Integration

In the past, some researchers utilized the numerical integration of Eq. 1 with a broad-resonance formula to calculate the resonant-reaction-rate (RRR) of a narrow resonance (*e.g.*, see Refs. [7, 8]), while others still utilized the simple analytic expression of Eq. 6 (*e.g.*, see Refs. [5, 9]). In order to check their differences, as an example, the RRR of a key stellar reaction $^{21}Na(p,\gamma)^{22}Mg$ is discussed below. There is a known resonant state in the compound nucleus ^{22}Mg at E_R=0.821 MeV (J^π=1$^+$, ℓ=0) with a proton width of Γ_p=16 keV and a resonant strength of $\omega\gamma$=0.556 eV (here $\Gamma_\gamma \approx \frac{\omega\gamma}{\omega}$=1.48 eV, and hence $\Gamma \approx \Gamma_p$) [10]. The corresponding γ-transition to the ground state in ^{22}Mg is a pure $M1$ transition (*i.e.*, $1^+ \rightarrow 0^+$) with a multipolarity L=1. According to the previous definition, this resonance ($\Gamma/E_R \approx 2$%) can be 'reasonably' treated as a narrow one.

Figure 1 shows the amplitudes of relevant functions used in the equations for this resonance state at the 'Gamow-peak' temperature T=1.6 GK. The narrow-resonance cross section $\sigma_{BW}^N(E)$ is calculated by assuming the constant partial widths Γ_p, Γ_γ (and Γ). Obviously the tendencies for this cross section and the corresponding integrand curve (indicated by a grey thick solid line) are physically unreal towards lower energies. The reason is the assumption of constant widths is invalid out of the resonance region. If a broad-resonance formula is used in the calculation, the integrand curve (indicated by a thick solid line) become physically reasonable at low energies. Here, the broad-resonance cross section $\sigma_{BW}^B(E)$ can be written as, (*i.e.*, Eq. (4.59)) in Ref. [3],

$$\sigma(E)_{BW}^B = \sigma_R \frac{E_R}{E} \frac{\Gamma_p(E)}{\Gamma_p(E_R)} \frac{\Gamma_\gamma(E)}{\Gamma_\gamma(E_R)} \frac{(\Gamma_R/2)^2}{(E-E_R)^2 + [\Gamma(E)/2]^2}. \quad (9)$$

The energy dependence of the proton and γ-ray partial widths are given by

$$\Gamma_p(E) = \Gamma_p(E_R) \frac{P_{\ell=0}(E)}{P_{\ell=0}(E_R)},$$

$$\Gamma_\gamma(E) = \Gamma_\gamma(E_R) B_\gamma \left(\frac{E + Q_{p\gamma} - E_{xf}}{E_R + Q_{p\gamma} - E_{xf}} \right)^{2L+1},$$

where $Q_{p\gamma}$ is the (p, γ) reaction Q-value (Q=5.508 MeV [10]), B_γ is the primary γ-ray branching ratio to the final state at E_{xf} (Here, B_γ is assumed to be unity and E_{xf}=0 for the ground state). The penetration factors, P_ℓ, are calculated by using a RCWFN [4] code with a channel-radius parameter of a_0=1.35 fm.

The resonant-reaction-rates (RRRs), due to this 0.821-MeV resonance's contribution, have been calculated by the numerical method (integration of Eq. 1 with a broad-resonance formula) and the analytical method (using Eq. 6), respectively. Ratios of the numerical and analytical results are shown in Fig. 2 as a function of temperature. Notably, at lower temperatures, the numerical results become much larger than the analytical ones. This implies a higher-energy resonance

can contribute to the reaction rate at low temperature significantly (or tremendously) more than the previous analytical result. Furthermore, presume this E_R=0.821 MeV resonance locating at 0.160, 0.323 MeV, the calculated *Ratio*s are 0.78, 0.90, respectively, at the relevant 'Gamow-peak' temperatures of 0.14, 0.4 GK. This conclusion demonstrates that the previous analytic results were underestimated by a considerable amount for a resonance of a few keV width even at their 'Gamow-peak' temperatures. Although the condition Γ/E_R<10 % still holds in these cases, δ_{MB} varies from 6 % to 37 % in the temperature range of 0.2~1.6 GK. It indicates that, in the present case, the resonance width is not narrow enough to use the analytic equations at low temperatures, and hence another restriction on the width should be set, *e.g.*, $\Gamma \leqslant 3.4$ keV for a temperature of 0.2 GK, and it is about five times narrower than the experimental value (Γ=16 keV). Finally, it should be pointed out two methods give almost the same results above 0.8 GK, and this demonstrates that the analytic Eq. 6 works very well only at certain temperature region (around its 'Gamow-peak' temperature).
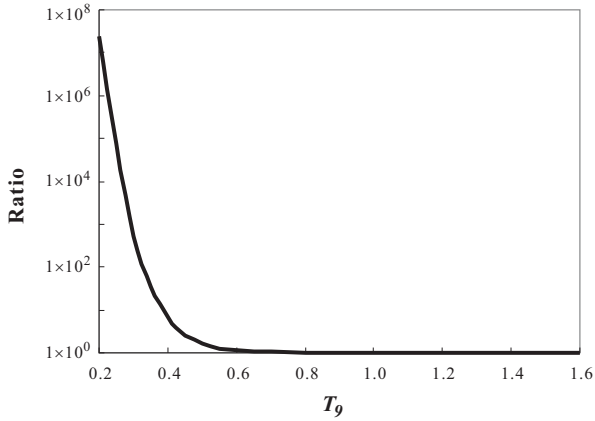
Figure 2: Ratios of the calculated resonant-reaction-rates (RRRs) using the numerical integration of Eq. 1 with a broad-resonance formula and using the analytic Eq. 6 as a function of temperature.

4 Conclusions

The validity of the resonant-reaction-rate (RRR) equations for an isolated narrow resonance have been reexamined, and it reminds us not to use those analytic equations without careful examination. As a suggestion, it's better to use the broad-resonance equation to calculate the RRR numerically even for a narrow resonance. In addition, the RRR is usually calculated by using the measured E_R and $\omega\gamma$ analytically in the popular direct measurement approach. We think this kind of calculation is inaccurate at low temperatures for a resonance of a few keV width. Because there are still researchers using the analytic equations without rigorous examinations so far, it is worthwhile to address this issue clearly and it will be helpful for the communities. In addition, some authors [7] thought that the product of Maxwell-Boltzmann distribution and cross section could give rise to another maximum caused by the low-energy wing of a resonance but, our calculation shows the appearance of this low-energy maximum depends on the temperature condition, for instance, there is no such maximum (but a plateau) in our example beyond $T \sim 0.5$ GK (of course, no maximum at T=1.6 GK in Fig. 1).

References

[1]. W.A. Fowler, G.R. Caughlan, and B.A. Zimmerman, *Ann. Rev. Astron. Astrophys.* **5** (1967) 525.

[2]. D.D. Clayton, *Principles of Stellar Evolution and Nucleosynthesis*, (University of Chicago Press, Chicago, 1983).

[3]. C.E. Rolfs and W.S. Rodney, *Cauldrons in the Cosmos*, (University of Chicago Press, Chicago, 1988).

[4]. A.R. Barnett *et al.*, Comput. Phys. Commun. **8** (1974) 377.

[5]. M. Wiescher *et al.*, Astron. Astrophys. **160** (1986) 56.

[6]. M. Wiescher *et al.*, Astrophys. J. **316** (1987) 162.

[7]. C. Angulo *et al.*, Nucl. Phys. A **656** (1999) 3.

[8]. K.I. Hahn *et al.*, Phys. Rev. C **54** (1996) 1999.

[9]. H. Herndl *et al.*, Phys. Rev. C **52** (1995) 1078.

[10]. J.M. D'Auria, *et al.*, Phys. Rev. C **69** (2004) 065803.

Determination of the astrophysically relevant ^{6}Li(n,γ)^{7}Li cross sections from the ^{7}Li(^{6}Li,^{7}Li)^{6}Li elastic-transfer reaction

SU Jun (苏俊), LI ZhiHong (李志宏), GUO Bing (郭冰), BAI XiXiang (白希祥), LI ZhiChang (李志常),
LIU JianCheng (刘建成), WANG YouBao (王友宝), LIAN Gang (连钢), ZENG Sheng (曾晟), WANG BaoXiang (王宝祥),
YAN ShengQuan (颜胜权), LI YunJu (李云居), LI ErTao (李二涛), FAN Qi-Wen(樊启文) & LIU WeiPing (柳卫平)

China Institute of Atomic Energy, Beijing 102413, China

(To be Published)

Angular distributions of the ^{7}Li(^{6}Li,^{7}Li)^{6}Li elastic-transfer reaction have been measured with the Q3D magnetic spectrograph at HI-13 tandem acceletator of Beijing, China. The neutron spectroscopic factors of ^{7}Li are derived by comparing the calculational differential cross sections with the distorted-wave Born approximation (DWBA) to the experimental data, and then used to deduce the direct capture cross sections in ^{6}Li(n,γ)^{7}Li at energies of astrophysical relevance.

Keywords: Big Bang nucleosynthesis, elastic-transfer reaction, spectroscopic factor

1   Introduction

Based on the baryon density value determined accurately by Wilkinson microwave anisotropy probe (WMAP)[1], the standard Big Bang nucleosynthesis (SBBN) has been successful in predicting the primary abundances of the light elements. However, the lithium abundances both for the ^{6}Li and ^{7}Li from SBBN deviate clearly from the observations of the metal-poor halo stars[2], these discrepancies have been attracting more and more interest along with the improvement both in the astrophysical observation and nucleosynthesis calculation. The key process for the production of ^{7}Li is the ^{3}He(α, γ)^{7}Be(EC+β^+)^{7}Li, and the ^{3}He(α, γ)^{7}Be cross sections have been well measured by a series of experiments[3, 4, 5, 6]. Moreover, the ^{7}Li also can be produced by the ^{6}Li(n,γ)^{7}Li reaction or destroyed by the reverse process, in a sense, ^{6}Li(n,γ)^{7}Li is a bridge between the ^{6}Li and ^{7}Li, its cross sections would affect the abundances of both ^{6}Li and ^{7}Li.

Toshiro et al. have measured the ^{6}Li(n,γ)^{7}Li cross sections at astrophysically relevant energies with a pulsed neutron beam[7], but the results are 1.5 times higher than the evaluated data, thus an independent verification is necessary. At the astrophysically relevant energies, the cross sections of ^{6}Li(n,γ)^{7}Li are most likely dominated by the E1 transitions into the ground and first excited states in ^{7}Li, which can also be derived by the direct capture model with the spectroscopic factors extracted from the single particle transfer reaction[8, 9, 10, 11].

In the present work, angular distributions for the ^{7}Li(^{6}Li,^{7}Li)^{6}Li elastic-transfer reaction have been measured. The neutron spectroscopic factors of ^{7}Li are derived and used to calculate the direct capture cross sections in ^{6}Li(n,γ)^{7}Li at energies of astrophysical relevance.

2   Angular distribution of ^{7}Li(^{6}Li,^{7}Li)^{6}Li
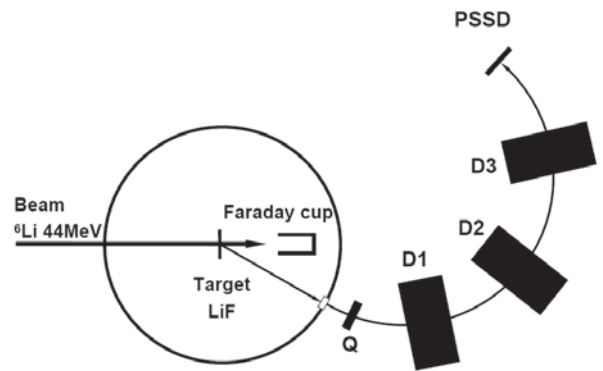
Figure 1: Schematic layout of the experimental setup.

The experiment is performed with the Q3D magnetic spectrograph at the Beijing HI-13 tandem accelerator. A natural LiF target is bombarded with a 44 MeV ^{6}Li beam. The thickness of the target is 530 $\mu g/cm^2$, the beam intensity is about 100 pnA during the experiment. A Faraday cup is set downstream of the target for recording the beam. The reac-

tion products are measured by Q3D magnetic spectrograph. By changing the angle of the spectrograph, the angular distribution of the reaction is obtained. The experimental setup is shown in Fig. 1.

The experimental angular distribution obtained for the ^{7}Li(^{6}Li,^{7}Li)^{6}Li elastic-transfer reaction is shown in Fig. 2. The experimental data at forward angles and at backward angles are obtained by measuring the reaction products ^{7}Li and ^{6}Li, respectively. For the elastic-transfer process, the contribution of the elastic scattering and transfer can not be distinguished in the experiment. However, the theoretical calculation shows that their mutual contributions at the respective forward angles are negligibly small. As a result, the effective differential cross sections at forward angles of the two processes can be obtained respectively. Thus, the experimental data at backward angles are used to extract the optical potential parameters for ^{6}Li+^{7}Li system, and these at forward angles are used to derive the neutron spectroscopic factor of ^{7}Li through the distorted wave Born approximation (DWBA) calculations.
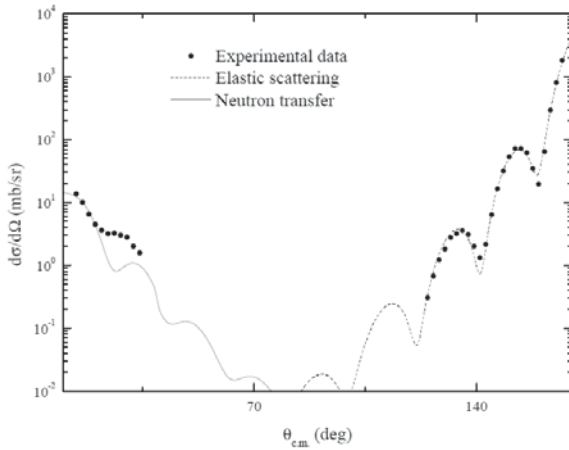
Figure 2: The angular distribution for the ^{7}Li(^{6}Li,^{7}Li)^{6}Li elastic-transfer reaction.

The spectroscopic factor ^{7}Li=^{6}Li⊗n, denoted as $S_{^7Li}$, can be derived by normalizing the DWBA calculations to the experimental data according to the expression

$$\left(\frac{d\sigma}{d\Omega}\right)_{EXP} = S_{^7Li}^2 \left(\frac{d\sigma}{d\Omega}\right)_{DWBA}. \qquad (1)$$

By comparing the experimental data with the calculations, the neutron spectroscopic factor for the ground state in ^{7}Li is determined to be 0.73±0.05, which is in good agreement with the theoretical predictions [12, 13] and the experimental results [14, 15]. Furthermore, the transfer reaction ^{7}Li(^{6}Li,^{7}Li$_{0.48}$)^{6}Li is also measured in our work, and the neutron spectroscopic factor for the first excited state in ^{7}Li is derived to be 0.90±0.09.

3 Astrophysically relevant ^{6}Li(n,γ)^{7}Li cross sections

At low energies of astrophysical interest, the direct capture reaction is almost dominated by the s wave neutron capture process, the contribution of the d wave is negligible. The cross sections for E1 capture of the neutron can be determined by

$$\sigma_t = \frac{16\pi}{9}\left(\frac{E_\gamma}{\hbar c}\right)^3 \frac{e_{eff}^2}{k^2}\frac{1}{\hbar v}\frac{(2I_f+1)}{(2I_1+1)(2I_2+1)}S_{l_f j_f}$$
$$\times \left|\int_0^\infty r^2 w_{l_i}(kr)u_{l_f}(r)dr\right|^2, \qquad (2)$$

where E_γ stands for the γ-ray energy, v is the relative velocity between neutron and ^{6}Li, k is the incident wave number, I_1, I_2 and I_f are the spins of neutron, ^{6}Li and ^{7}Li, respectively; $e_{eff} = -ez/(A+1)$ represents the neutron effective charge for the E1 transition; $w_{l_i}(kr)$ refers the distorted radial wave function for the entrance channel, and $u_{l_f}(r)$ is the radial wave function of the bound state neutron in ^{7}Li.

The energy dependence of direct capture cross section for the ^{6}Li(n,γ)^{7}Li reaction, including the contributions of the ground and first excited states in ^{7}Li, are then calculated with the spectroscopic factors extracted above, the results are
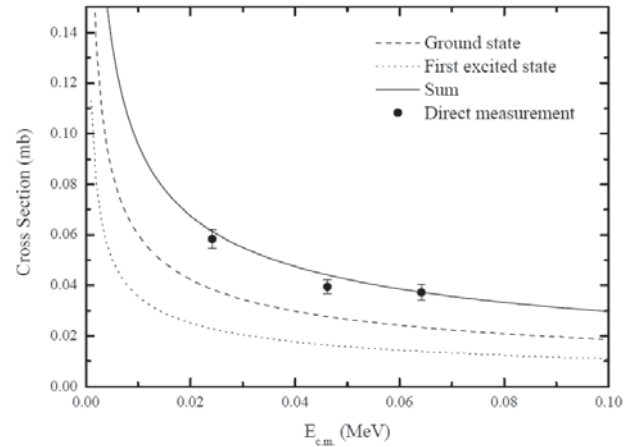
Figure 3: Cross sections of the ^{6}Li(n,γ)^{7}Li reaction.

4 Summary

In summary, the angular distribution for the ^{7}Li(^{6}Li,^{7}Li)^{6}Li elastic-transfer reaction has been measured. The neutron spectroscopic factors for the ground and first excited states in ^{7}Li are determined based on the DWBA analysis, then used to calculate the direct capture cross sections in ^{6}Li(n,γ)^{7}Li at energies of astrophysical relevance, our results are consistent with the direct measurement.

References

[1]. Dunkley J et al 2009 *Astrophys. J. Suppl* **180** 306
[2]. Cayrel R et al 2008 *arXiv:0810.4290v2*
[3]. Sin B S N et al 2004 *Phys. Rev. Lett.* **93** 262503
[4]. Gyurky G et al 2007 *Phys. Rev. C.* **75** 035805
[5]. Confortola F et al 2007 *Phys. Rev. C.* **75** 065803
[6]. Brown T A D et al 2007 *Phys. Rev. C.* **76** 055801
[7]. Toshiro O et al 2000 *AIP Conference Proceedings* **529** 678
[8]. Li Z H et al 2005 *Phys. Rev. C* **71** 052801(R)
[9]. Su J et al 2006 *CHIN. PHYS. LETT.* **23** 55
[10]. Li Z H et al 2006 *Phys. Rev. C* **74** 035801
[11]. Guo B et al 2007 *CHIN. PHYS. LETT.* **24** 65
[12]. Cohen S and Kurath D 1967 *Nucl. Phys. A* **101** 1
[13]. Kumar N 1974 *Nucl. Phys. A* **225** 221
[14]. Li T Y and Mark S K 1969 *Nucl. Phys. A* **123** 147
[15]. Towner I S 1969 *Nucl. Phys. A* **126** 97

New determination of the astrophysical ^{13}C$(p,\gamma)^{14}$N $S(E)$ factors and reaction rates via the ^{13}C$(^7$Li,^{6}He$)^{14}$N reaction

Y. J. LI(李云居)[1], Z. H. LI(李志宏)[1]*, E. T. Li(李二涛)[1], X. X. Bai(白希祥)[1], J. Su(苏俊)[1], B. Guo(郭冰)[1],

B. X. Wang(王宝祥)[1], S. Q. Yan(颜胜权)[1], S. Zeng(曾晟)[1], Z. C. Li(李志常)[1], J. C. Liu(刘建成)[1],

X. Liu(刘鑫)[1], S. J. Jin(金孙均)[1], Y. B. Wang(王友宝)[1], L. Y. Zhang(张立勇)[2], X. Q. Yu(于祥庆)[2],

L. Li(李龙)[2], G. Lian(连钢)[1], Q. W. Fan(樊启文)[1] & W. P. Liu(柳卫平)[1]

[1]*China Institute of Atomic Energy, Beijing 102413, China;*
[2]*Institute of Modern Physics, Chinese Academy of Sciences (CAS), Lanzhou 730000, PRC*

(The current article has been submitted to Eur. Phys. J. A)

The ^{13}C$(^7$Li,^{6}He$)^{14}$N$_{0,1}$ reactions were measured at $E(^7$Li$) = 34$ MeV with the Q3D magnetic spectrograph of HI-13 tandem accelerator, and the first peaks of the angular distributions were obtained for the first time. The ^{14}N$_{0,1}$ proton spectroscopic factors were extracted to be 0.67 ± 0.09 and 0.73 ± 0.10, respectively. Using the ^{13}C$(p,\gamma)^{14}$N direct capture $S_{\rm dc}(E)$ factors derived by the spectroscopic factors, the direct measurement data for both 1^- and 0^- resonances were well fitted via updating the resonance parameters, and then the total astrophysical ^{13}C$(p,\gamma)^{14}$N $S(E)$ factors and reaction rates were determined at stellar energies. The present work offers an independent examination to the existing results of the ^{13}C$(p,\gamma)^{14}$N reaction.

1 Introduction

^{13}C$(p,\gamma)^{14}$N is one of the key reactions in the CNO cycle [1]. It supplies the ^{14}N seed nuclei for the ^{14}N$(p,\gamma)^{15}$O radiative capture reaction which is the slowest one, and hence decides the rate of energy production in this cycle. The ^{13}C$(p,\gamma)^{14}$N reaction is also important for the nucleosynthesis via the s-process because it affects the abundance of seed nuclei for the ^{13}C$(\alpha,n)^{16}$O reaction which is believed to be the neutron source in AGB stars with solar metalicity [2].

So far, several direct measurements of the ^{13}C$(p,\gamma)^{14}$N reaction [3, 4, 5, 6] have only reached down to 100 keV which is much higher than the stellar energies ($\sim$25 keV). The accurate measurement for the $S(E)$ factors was carried out in the energy range of $100 \sim 900$ keV [6], and the R-matrix fit gave $S(0) = 7.6$ keV b [7, 8], whereas the latest measurement in inverse kinematics and R-matrix fit deduced a relatively small result of $S(0) = 4.85$ keV b [9].

There are two excited states at 1^- 8062 keV and 0^- 8776 keV in ^{14}N contribute to the ^{13}C$(p,\gamma)^{14}$N resonant captures in the astrophysical energy region. Although the contribution from the resonance tails may be much higher than that from the direct capture component, the interference between two processes can lead to an appreciable influence on the total

S(E) factors. Thus the precise measurement of direct capture is necessary to obtain the reliable S(E) factors, particularly at astrophysically relevant energies. The ^{13}C$(p,\gamma)^{14}$N direct capture cross section can be derived in term of spectroscopic factor or asymptotic normalization coefficient (ANC) of ^{14}N$\rightarrow^{13}$C $+ p$, deduced from the angular distribution of proton transfer reactions.

Several experiments have been performed to study the spectroscopic factors or ANCs of ^{14}N$\rightarrow^{13}$C $+ p$ through the ^{13}C(d,n) [10, 11], ^{13}C$(^3$He, $d)$ [12, 13, 14], ^{13}C$(^7$Li,^{6}He$)$ [15] and ^{13}C$(^{14}$N,^{13}C$)$ [16] reactions. The spectroscopic factors and ANCs extracted from these measurements deviate in varying degrees, especially for the first excited state in ^{14}N. In order to clarify the discrepancy, new measurement is still needed. The $(^7$Li,^{6}He$)$ reactions are thought to be a valuable spectroscopic tool [17] because the shapes of their angular distributions can be well reproduced by the distorted wave Born approximation (DWBA), and the proton spectroscopic factor of ^{7}Li is well determined [18, 19]. Unfortunately, the above mentioned ^{13}C$(^7$Li,^{6}He$)$ measurement missed the first peak. Hence it is highly desired to ameliorate the measurement of ^{13}C$(^7$Li, ^{6}He$)^{14}$N reaction.

In the present work, the angular distributions of ^{7}Li elastic scattering on ^{13}C and ^{13}C$(^7$Li,^{6}He$)^{14}$N transfer reactions

leading to ground and first excited states in ^{14}N have been measured with the Q3D magnetic spectrograph [20] at E(^{7}Li) = 34 MeV. The spectroscopic factors were derived based on DWBA analysis, and then used to calculate the astrophysical ^{13}C$(p, \gamma)^{14}$N $S(E)$ factors and reaction rates at stellar energies.

2   Measurement of the angular distributions

Our experiment was carried out with a 34 MeV ^{7}Li beam from HI-13 tandem accelerator, Beijing. The 150 enA ^{7}Li beam impinged on a 90 μg/cm^2 self-supporting ^{13}C target with a purity of 94%. A ^{12}C target with the same thickness served as the background measurement. A removable Faraday cup behind the target was used to collect the beam for normalization. It covered an angular range of $\pm 6°$ and thus restricted the attainable minimum angle. The relative normalization of measurements at angles of $\theta_{lab} \leqslant 6°$ was carried out by monitoring the elastic scattering events with a ΔE - E counter telescope placed at 25° downstream of the target. The accepted solid angle of Q3D magnetic spectrometer was set to be 0.34 mSr for a good angular resolution. The reaction products were focused and separated by Q3D, and measured by a 50 mm × 50 mm two-dimensional position sensitive silicon detector (PSSD) on the focal plane.
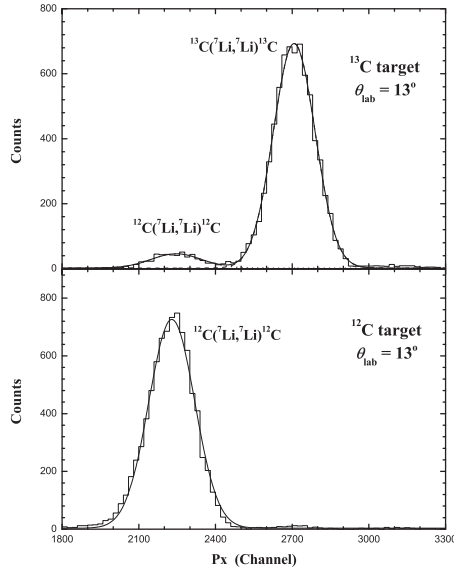
Figure 1: Typical position spectra on the Q3D focal plane for the ^{7}Li + ^{12,13}C elastic scattering.

The ^{13}C$(^{7}$Li,^{7}Li)^{13}C elastic scattering and the ^{13}C$(^{7}$Li, ^{6}He)^{14}N$_{0,1}$ transfer reactions were measured in the angular ranges of $9° \leqslant \theta_{lab} \leqslant 27°$ and $2° \leqslant \theta_{lab} \leqslant 21°$ in steps of 1°, respectively. The typical position spectra of elastic scattering events for ^{7}Li on ^{13}C and ^{12}C targets are shown in Fig.1. The purity of ^{13}C target can be determined accurately via the analysis of the position spectra. The disturbance from

the ^{12}C contaminant in ^{13}C target can completely be eliminated based on the position spectra at each angle. Finally, the ^{13}C$(^{7}$Li,^{7}Li)^{13}C, ^{13}C$(^{7}$Li,^{6}He)^{14}N$_0$ and ^{13}C$(^{7}$Li,^{6}He)^{14}N$_1^*$ angular distributions were obtained as shown in Fig.2 with solid circles. It can be seen clearly that the first peaks of ^{13}C$(^{7}$Li,^{6}He)^{14}N$_{0,1}$ angular distributions are fully measured in the present work. The uncertainties of the differential cross sections are about 7%, mainly from the statistics and ununiformity of the target thickness.
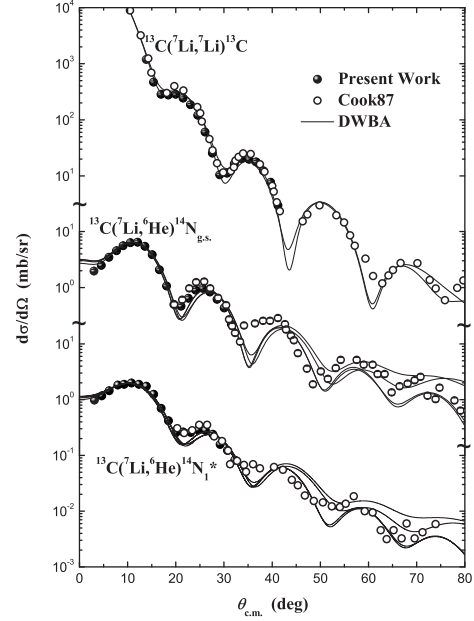
Figure 2: Angular distributions of ^{13}C$(^{7}$Li, ^{7}Li)^{13}C, ^{13}C$(^{7}$Li, ^{6}He)^{14}N$_0$ and ^{13}C$(^{7}$Li, ^{6}He)^{14}N$_1^*$ at $E(^{7}$Li) = 34 MeV, together with the DWBA calculations. The solid and open circles denote the data obtained in the present experiment and the earlier work[15], respectively.

3   DWBA calculations

^{13}C$(^{7}$Li,^{6}He)^{14}N$_{0,1}$ angular distributions were calculated with the DWBA code PTOLEMY[21]. The optical potential parameters for the entrance channel were chosen from Ref.[15] and extracted by fitting the present ^{13}C$(^{7}$Li,^{7}Li)^{13}C angular distribution with real and imaginary potentials of Woods-Saxon form, respectively. Since no experimental data exist for the ^{6}He elastic scattering on ^{14}N, the angular distributions of the ^{14}N$(^{6}$Li,^{6}Li)^{14}N at E_{lab} = 32 MeV[22] and ^{13}C$(^{6}$Li,^{6}Li)^{13}C at E_{lab} = 28 MeV[23] were used to derive the potential parameters for the exit channels. All the potential parameters are listed in Table 1. For calculating the wave functions of the bound states, the Woods-Saxon potentials with the standard geometrical parameters r_0 = 1.25 fm and a = 0.65 fm were adopted, and the potential depths were adjusted automatically to reproduce the proton binding energies of ^{14}N$_{0,1}$.

Table 1: Woods-Saxon potential parameters for the entrance and exit channels of ^{13}C(^{7}Li,^{6}He)^{14}N$_{0,1}$. Set I is taken from Ref.[15], Set II, III and IV are extracted by fitting the ^{13}C(^{7}Li,^{7}Li)^{13}C, ^{14}N(^{6}Li,^{6}Li)^{14}N and ^{13}C(^{6}Li,^{6}Li)^{13}C elastic scattering angular distributions, respectively. The depths and geometrical parameters are in MeV and fm, respectively. The last row gives the goodness of fit(χ^2 per point).

Channel	^{7}Li + ^{13}C		^{6}He + ^{14}N	
	Set I	Set II	Set III	Set IV
U_V	159.0	198.75	124.88	131.65
r_R	0.63	0.52	0.52	0.60
a_R	0.81	0.90	1.02	0.91
W_V	8.16	8.70	15.37	7.14
r_I	1.33	1.31	1.30	1.31
a_I	0.78	0.73	0.54	0.7
r_C	1.25	1.0	1.0	1.0
χ^2/p		15.22	6.37	1.35

The ^{14}N proton spectroscopic factor $S^{l_p j_p}_{^{14}N}$ can be derived by normalizing the DWBA calculations to the experimental data according to the expression

$$\left(\frac{d\sigma}{d\Omega}\right)_{exp} = \sum_{l_p j_p} S_{^7Li} S^{l_p j_p}_{^{14}N} \left(\frac{d\sigma}{d\Omega}\right)^{l_p j_p}_{DWBA}, \quad (1)$$

where $(d\sigma/d\Omega)_{exp}$ and $(d\sigma/d\Omega)_{DWBA}$ are the measured and calculated differential cross sections, respectively. The proton spectroscopic factor of ^{7}Li has been determined to be $S_{^7Li} = 0.42$ in Refs. [18, 19].
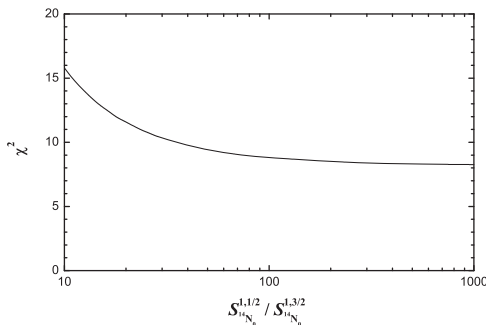
Figure 3: Goodness of fit vs. $S_{p1/2}/S_{p3/2}$ for the ^{13}C(^{7}Li, ^{6}He)^{14}N$_0$ angular distribution.

Table 2: Theoretical and experimental proton spectroscopic factors for the ground and first exited states in ^{14}N.

$S_{^{14}N_0}$	$S_{^{14}N_1^*}$	Exp. or The.	Ref.
0.68	0.99	Theory	[24]
0.80	0.96	Theory	[26]
0.65	0.89	Theory	[27]
1.09±0.19	1.42±0.24	^{13}C(d, n)^{14}N	[10]
0.50±0.10	0.56±0.11	^{13}C(d, n)^{14}N	[11]
0.76±0.15	0.92±0.18	^{13}C(^{3}He,d)^{14}N	[12]
0.58±0.04	0.93±0.07	^{13}C(^{3}He,d)^{14}N	[13]
0.60±0.09	0.79±0.12	^{13}C(^{3}He,d)^{14}N	[14]
0.68±0.04	0.58±0.06	^{13}C(^{14}N,^{13}C)^{14}N	[16]
0.62±0.07	0.83±0.10	^{13}C(^{7}Li,^{6}He)^{14}N	[15]
0.67±0.09	0.73±0.10	^{13}C(^{7}Li,^{6}He)^{14}N	Present

Proton transfers to the $1p_{1/2}$ and $1p_{3/2}$ orbits of the ground state in ^{14}N were taken into account in the analysis of experimental data. It was found that the χ^2 decreases with the increase of $S^{1,1/2}_{^{14}N_0}/S^{1,3/2}_{^{14}N_0}$, as shown in Fig.3. This result indicates that $S^{1,1/2}_{^{14}N_0}/S^{1,3/2}_{^{14}N_0}$ should be greater than 100 according to the precision of our experiment. It supports the theoretical calculations[24, 25], and differs from the previously experimental value of 20[16]. Because of the very small contribution, the $1p_{3/2}$ component was neglected in DWBA analysis for the ^{13}C(^{7}Li,^{6}He)^{14}N$_0$ reaction. For the proton transfer to the first exited state in ^{14}N, only $1p_{1/2}$ component was taken into account due to the parity and angular momentum constraints.

The calculated results are also shown in Fig.2 with solid lines. It can be seen that the experimental angular distributions are well reproduced. Different from the earlier (^{7}Li,^{6}He) study[15], no obvious phase shift between the calculations and the experimental data is found in the present work. The spectroscopic factors of ^{14}N$_0 \rightarrow {}^{13}$C + p and ^{14}N$_1^* \rightarrow {}^{13}$C + p are determined to be 0.67 ± 0.09 and 0.73 ± 0.10, respectively. The uncertainties are mainly from the measurement(7%), divergence of optical potential parameters (8%) and error of the ^{7}Li proton spectroscopic factors (9%). The spectroscopic factors obtained in several theoretical and experimental investigations are listed in Table 2. Our result is in fair agreement with those derived from the ^{13}C(^{3}He, d)^{14}N[14] and ^{13}C(^{14}N,^{13}C)^{14}N[16] reactions within the uncertainty. As compared to the previous ^{13}C(^{7}Li, ^{6}He)^{14}N work[15], the results are close to each other by chance, however, the $S_{^7Li}$ cited therein is a factor of 1.4 larger than that used in our calculations.

4 The ^{13}C(p, γ) astrophysical $S(E)$ factors and reaction rates

The ^{13}C$(p, \gamma)^{14}$N direct captures are dominated by the $E1$ transition from incoming s-, d- wave to the first three bound states and p-wave to the next four excited states in ^{14}N. The astrophysical $S(E)$ factors are related to the cross sections by

$$S(E) = E\sigma(E) \exp(E_G/E)^{1/2}, \quad (2)$$

where $E_G = 0.989Z_1^2 Z_2^2 \mu$ MeV is the Gamow energy, and μ denotes the reduced mass. The cross section for $E1$ direct

capture can be expressed as

$$\sigma = \frac{16\pi}{9}\left(\frac{E_\gamma}{\hbar c}\right)^3 \frac{e_{\text{eff}}^2}{k^2} \frac{1}{\hbar v} \frac{(2I_f + 1)}{(2I_1 + 1)(2I_2 + 1)} S_{l_f j_f}$$
$$\times \left| \int_0^\infty r^2 \omega_{l_i}(kr) u_{l_f}(r) dr \right|^2, \quad (3)$$

where E_γ is the γ-ray energy; k denotes the incident wave number; $e_{\text{eff}} = e(A - Z)/(A + 1)$ stands for the proton effective charge of the $E1$ transition in the potential produced by a target nucleus with mass number A and atomic number Z; v is the relative velocity between proton and ^{13}C; I_1, I_2 and I_f are the spins of proton, ^{13}C, and ^{14}N, respectively; $S_{l_f j_f}$ is the proton spectroscopic factor of ^{14}N; $\omega_{l_i}(kr)$ is the distorted radial wave function for the entrance channel, and $u_{l_f}(r)$ is the radial wave function of the bound state proton in ^{14}N.
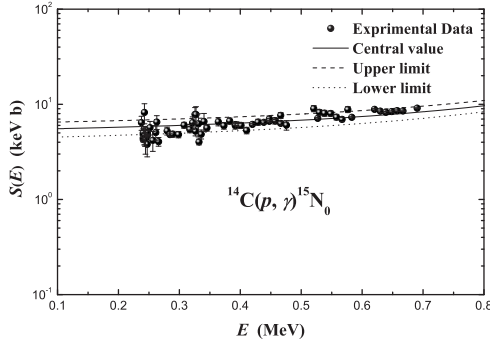
Figure 4: Astrophysical $S(E)$ factors for the ^{14}C$(p, \gamma)^{15}$N$_0$ reaction. The solid circles denote the experimental data from [32]. The solid, dashed and dotted lines are central value, upper and lower limits, respectively.

In the calculation of $u_{l_f}(r)$, the imaginary part of the optical potential was neglected because of the small flux into other reaction channels. For the real part, a Wood-Saxon potential is adopted, for which r_0 and a were set as the same as those for the ^{14}N$\rightarrow^{13}$C $+ p$ bound state. According to the previous approach[28, 29, 30, 31], the potential depth for the ^{13}C $+ p$ system was adjusted to reproduce the volume integral of potential per nucleon $J_V/A= 374 \pm 20$ MeV fm^3 derived from fit the ^{14}C$(p, \gamma)^{15}$N$_0$ astrophysical $S(E)$ factors[32]. The same proton spectroscopic factor of ^{15}N$_0$ and resonance parameters therein were used in our fitting, the result is shown in Fig.4. With the fitted J_V/A value, the ^{13}C $+ p$ potential depth was derived to be $V_0 = 30.8 \pm 1.6$ MeV for the s-wave. As to the d-wave, a pure coulomb wave function was used in the calculation due to the influence of centrifugal potential. Based on the $S_{^{14}N}$ and potential parameters derived above, the energy dependence of astrophysical ^{13}C$(p, \gamma)^{14}$N$_0$ direct capture $S_{\text{dc}}(E)$ factors was calculated with the code RADCAP[33], as shown in Fig.5 with dashed line.

The resonant capture $S_{\text{res}}(E)$ factors can be calculated with the Breit-Wigner formula[1],

$$S_{\text{res}}(E) = \frac{\pi \hbar^2}{2\mu} \frac{2J + 1}{(2J_1 + 1)(2J_2 + 1)}$$

$$\times \frac{\Gamma_p(E)\Gamma_\gamma(E)}{(E - E_R)^2 + (\Gamma_{\text{tot}}/2)^2} \exp\left(\frac{E_G}{E}\right)^{1/2}, \quad (4)$$

where J, J_1 and J_2 are the spins of ^{14}N, proton and ^{13}C, respectively; E_R stands for the resonance energy; Γ_p, Γ_γ and Γ_{tot} denote the proton, radiative and total widths in sequence. The energy dependence of Γ_p and Γ_γ are given by

$$\Gamma_p(E) = \Gamma_p(E_R) \frac{\exp[-(E_G/E)^{1/2}]}{\exp[-(E_G/E_R)^{1/2}]}, \quad (5)$$

and

$$\Gamma_\gamma(E) = \Gamma_\gamma(E_R) \frac{(Q + E)^{2l+1}}{(Q + E_R)^{2l+1}}, \quad (6)$$

where Q and l are the reaction energy and multipolarity of the gamma transition, respectively.

Since the angular momentum (s wave) and multipolarity for the resonant captures of 1^- 8062 keV and 0^- 8776 keV states into ^{14}N$_0$ are identical with those of direct capture, they can interfere with each other. In this case, the total $S(E)$ factors should be calculated by[34]

$$S(E) = S_{\text{dc}}(E) + \sum_i S_{\text{res}i}(E)$$
$$\pm \sum_i 2[S_{\text{dc}}(E)S_{\text{res}i}(E)]^{1/2} \cos(\delta_i), \quad (7)$$

where i denotes the resonance number; $\delta = \arctan[\frac{\Gamma_p(E)}{2(E - E_R)}]$ is the resonance phase shift. Generally, the sign of the interference in equation 7 has to be determined experimentally.

Among the direct measurements of ^{13}C$(p, \gamma)^{14}$N$_0$ reaction, only Zeps et al.[35] provided the available excitation function which covered both the 1^- and 0^- resonances. The excitation function was transformed to astrophysical $S(E)$ factors through normalizing to the data of 1^- resonance peak[6, 9]. The result is well consistent with that from Ref.[6] in the energy range of 600 ~ 900 keV. Finally, we chose the data of 100 ~ 900 keV from Ref.[6] and those of 600 ~ 1850 keV from Ref.[35] to fit the ^{13}C$(p, \gamma)^{14}$N$_0$ astrophysical $S(E)$ factors.

Table 3: Resonance parameters for the ^{13}C$(p, \gamma)^{14}$N reaction.

J^π, T	E_R (keV)			
	Ref.[6]	Ref.[35]	Ref.[8]	Present
1^-, 1	518.14±0.95		517	517.7±2.2
0^-, 1	1225.7±6.5	1251.0±7.0	1244	1313.0±16.0
	Γ_p (keV)			
1^-, 1	37.14±0.98	37.07	37	37.1±1.0
0^-, 1	408.57	440±8	416	601±48

Table 4: Radiative widths used in the present calculation along with those form Refs.[6, 8].

J^π, T	J^π, E_f	Γ_γ (keV)		
		Ref.[6]	Ref.[8]	Present
$1^-, 1$	$1^+, 0.00$	9.1 ± 1.3	9.1	9.1 ± 0.7
	$0^+, 2.31$	0.22 ± 0.04	0.22	0.21 ± 0.05
	$1^+, 3.95$	1.53 ± 0.21	1.53	1.57 ± 0.07
	$0^-, 4.92$	0.262 ± 0.043	0.26	0.27 ± 0.04
	$2^-, 5.11$	0.075 ± 0.025	0.085	0.074 ± 0.019
	$1^-, 5.69$	0.61 ± 0.14	0.63	0.61 ± 0.08
$0^-, 1$	$1^+, 0.00$	46 ± 12	56	45.4 ± 2.5
	$1^+, 3.95$	0.46 ± 0.14	0.56	
	$2^-, 5.11$	0.37 ± 0.14	0.23	
	$1^-, 5.69$	0.23 ± 0.20	0.23	

Based on the $S_{dc}(E)$ factors obtained above, the direct measurement data were fairly reproduced via adjusting the resonance parameters. The adopted resonance parameters are listed in Tables 3 and 4 together with the previous ones. It is found that our $S_{dc}(E)$ factors lead to the best fitting for the $^{13}C(p,\gamma)^{14}N_0$ astrophysical $S(E)$ factors at the energy range of $100 \sim 1850$ keV, as displayed in Fig.5. Their uncertainties are mainly from the errors of spectroscopic factor and fitting result. As can be seen from Fig.5, the low energy tail of 1^- resonance and its interference with the direct capture dominates the $S(0)$ factor, and those of 0^- resonance also make a considerable contribution ($\sim 20\%$). On the other hand, the high energy tail of 1^- resonance affects the determination of the 0^- resonance parameters significantly, and therefore does the value of $S(0)$ factor. Thus it is more reasonable to take the direct measurement data of these two resonances into account.

The total $^{13}C(p,\gamma)^{14}N$ astrophysical $S(E)$ factors are the sum of the individual ones for the transitions to the ground and first six excited states. Follow the above procedure, the $S_{^{14}N_1^*}$ from this work and the $S_{^{14}N_{2\sim6}^*}$ from Refs.[8, 13, 16] were used to calculate the $S(E)$ factors for the first and other excited states, respectively. The $^{13}C(p,\gamma)^{14}N_{1\sim6}^*$ direct measurement data from King et al.[6] were used in the fitting. The $S(0)$ values corresponding to the ground and individual excited states as well as the total are listed in Table 5. The total $S(25$ keV$)$ is found to be 7.95 ± 0.59 keV b in this work.
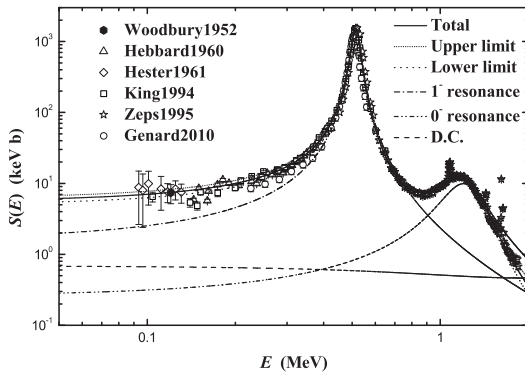
Figure 5: $^{13}C(p,\gamma)^{14}N_0$ astrophysical $S(E)$ factors. The experimental data are taken from Refs.[3, 4, 5, 6, 9, 35]. The various lines are the calculated results in the present work.

Table 5: Comparison of $S(0)$ values derived in this work and the previous ones from Refs.[8, 14, 9].

State ^{14}N	$S(0)$ (kev·b)			
J_f^π, E_f	Ref.[8]	Ref.[14]	Ref.[9]	Present
$1^+, 0.00$	5.16 ± 0.72	5.06	3.54 ± 0.59	5.53 ± 0.56
$0^+, 2.31$	0.32 ± 0.08	0.35		0.45 ± 0.08
$1^+, 3.95$	0.90 ± 0.13	0.79		0.98 ± 0.08
$0^-, 4.92$	0.33 ± 0.07	0.17		0.17 ± 0.01
$2^-, 5.11$	0.046 ± 0.009	0.046		0.034 ± 0.004
$1^-, 5.69$	0.77 ± 0.09	0.5		0.50 ± 0.04
$3^-, 5.83$	0.031 ± 0.007	0.03		0.023 ± 0.002
Total	7.58 ± 1.10	6.94	4.85 ± 0.76	7.70 ± 0.57

The astrophysical $^{13}C(p,\gamma)^{14}N$ reaction rates are calculated with

$$N_A\langle\sigma v\rangle = N_A(\frac{8}{\pi\mu})^{1/2}\frac{1}{(k_BT)^{3/2}}$$
$$\times \int_0^\infty S(E)\exp[-(\frac{E_G}{E})^{1/2} - \frac{E}{k_BT}]dE, \quad (8)$$

where v is the relative velocity of the colliding nuclei, N_A and k_B are Avogadro and Boltzmann constants, respectively. Our reaction rates are shown in Fig.6, along with the ratios of ours to the adopted ones in the NACRE compilation[36]. It can be seen that ours are a factor of 1.14 higher at temperatures corresponding to hydrostatic hydrogen burning.
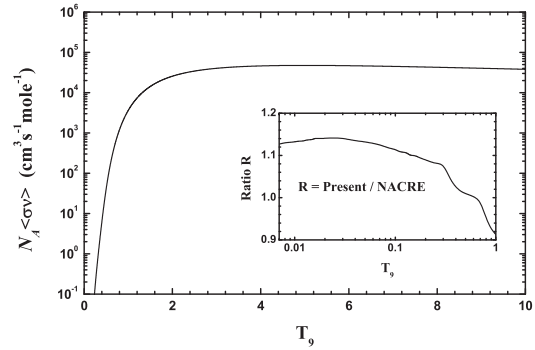
Figure 6: Astrophysical $^{13}C(p,\gamma)^{14}N$ reaction rates of present work, and the inset is the ratio of our adopted reaction rates to the reaction rates adopted in the NACRE compilation.

Table 6: Fitting parameters of the astrophysical $^{13}C(p,\gamma)^{14}N$ reaction rates.

Parameters	Values	Parameters	Values
a_0	53.7583	b_0	10.9970
a_1	-2.77259	b_1	0.00161815
a_2	-28.9595	b_2	-14.6062
a_3	-16.7963	b_3	11.3394
a_4	3.32144	b_4	-1.74689
a_5	-0.475174	b_5	0.118376
a_6	-5.01685	b_6	-2.65260

The total reaction rates as a function of temperature obtained in this work are parameterized with an expression used in the REACLIB,

$$N_A\langle\sigma v\rangle = \exp(a_0 + a_1 T_9^{-1} + a_2 T_9^{-1/3} + a_3 T_9^{1/3} + a_4 T_9$$

$$+a_5 T_9^{5/3} + a_6 \ln T_9) + \exp(b_0 + b_1 T_9^{-1} + b_2 T_9^{-1/3}$$
$$+b_3 T_9^{1/3} + b_4 T_9 + b_5 T_9^{5/3} + b_6 \ln T_9). \qquad (9)$$

The values of fit parameters $a_{0\sim6}$ and $b_{0\sim6}$ for the present adopted reaction rates are listed in Table 6, and the fitting errors are less than 2% in the temperature range of $0.001 < T_9 < 10$.

5   Summary and Discussion

In this work the angular distributions of the $^{13}C(^{7}Li, ^{7}Li)^{13}C$ elastic scattering and the $^{13}C(^{7}Li, ^{6}He)^{14}N_{0,1}$ reactions have been measured at $E(^{7}Li) = 34$ MeV with the Q3D magnetic spectrograph. The first peaks of angular distributions for the transfer reactions have been completely presented for the first time. The data were fairly reproduced by the DWBA calculations, and then the proton spectroscopic factors of $^{14}N_0$ and $^{14}N_1^*$ were derived.

The $^{13}C(p, \gamma)^{14}N$ direct capture $S_{dc}(E)$ factors were determined by using the proton spectroscopic factors of ^{14}N. Based on the $S_{dc}(E)$ factors, the direct measurement data for 1^- and 0^- resonances were well fitted via updating the resonance parameters. The total $^{13}C(p, \gamma)^{14}N$ astrophysical $S(E)$ factors were then calculated. The result indicates that these two resonances should be taken into account simultaneously for the precise analysis of $S(E)$ factors.

The astrophysical $^{13}C(p, \gamma)^{14}N$ reaction rates derived in this work are a factor of 1.14 higher than the adopted in NACRE compilation for the temperature range of hydrostatic hydrogen burning. This implies the increase of seed nuclei for the $^{14}N(p, \gamma)^{15}O$ reaction in CNO cycle and weakening of the $^{13}C(\alpha, n)^{16}O$ reaction as a neutron source for the s process.

The present work offers an independent examination to the existing results of the $^{13}C(p, \gamma)^{14}N$ reaction.

References

[1].   C.E. Rolfs, W.S. Rodney, *Cauldrons in the Cosmos* (The University of Chicago Press, Chicago, 1988).

[2].   M. Lugaro, F. Herwig, J.C. Lattanzio, R. Gallino, O. Straniero, Astrophys. J. **586**, 1305 (2003).

[3].   E.J. Woodbury and W.A. Fowler, Phys. Rev. **85**, (1952) 51.

[4].   D.F. Hebbard, J.L. Vogl, Nucl. Phys. **21**, (1960) 652.

[5].   R.E. Hester, W.A.S. Lamb, Phys. Rev. **121**, (1961) 584.

[6].   J.D. King, R.E. Azuma, J.B. Vise, J. Görres, C. Rolfs, H.P. Trautvetter, A.E. Vlieks, Nucl. Phys. A **567**, (1994) 354.

[7].   A.M. Mukhamedzhanov, A. Azhari, V. Burjan, C.A. Gagliardi, V. Kroha, A. Sattarov, X. Tang, L. Trache, R.E. Tribble, Phys. Rev. C **66**, (2002) 207602.

[8].   A.M. Mukhamedzhanov, A. Azhari, V. Burjan, C.A. Gagliardi, V. Kroha, A. Sattarov, X. Tang, L. Trache, R.E. Tribble, Nuclear Physics A **725**, (2003) 279.

[9].   G. Genard, P. Descouvemont, G. Terwagne, J. Phys. Confer. Ser. **202**, (2010) 012015.

[10].   G.S. Mutchler, D. Rendic, D.E. Velkley, W.E. Sweeney, G.C. Phillips, Nucl. Phys. A **172**, (1971) 469.

[11].   J.R. Bobbitt, M.P. Etten, G.H. Lenz, Nucl. Phys. A **203**, (1973) 353.

[12].   R.J. Peterson, J.J. Hamill, Nucl. Phys. A **362**, (1981) 163.

[13].   P. Bém, V. Burjan, V. Kroha, J. Novák, Š. Piskoř, E. Šimečková, J. Vincour, C.A. Gagliardi, A.M. Mukhamedzhanov, R.E. Tribble, Rhys. Rev. C **62**, (2000) 024320.

[14].   S.V. Artemov, A.G. Bajajin, S.B. Igamov, S.B. Igamov, G.K. Nie, R. Yarmukhamedov, Phys. Atom. Nucl. **71**, (2008) 998.

[15].   J. Cook, M.N. Stephens, K.W. Kemper, Nucl. Phys. A **466**, (1987) 168.

[16].   L. Trache, A. Azhari, H.L. Clark, C.A. Gagliardi, Y.-W. Lui, A.M. Mukhamedzhanov, R.E. Tribble, F. Carstoiu, Phys. Rev. C **58**, (1998) 2715.

[17].   K.W. Kemper, R.L. White, L.A. Charlton, G.D. Gunn, G.E. Moore, Phys. Lett. B **52**, (1974) 179

[18].   L. Lapikás, J. Wesseling, R.B. Wiringa, Phys. Rev. Lett. **82**, 1999 4404.

[19].   Z.H. Li, E.T. Li, B.Guo, X.X. Bai, Y.J. Li, S.Q. Yan, Y.B. Wang, G. Lian, J. Su, B.X. Wang, S. Zeng, X. Fang, W.P. Liu, Eur. Phys. J. A **44**, (2010) 1.

[20].   Z. Li, Y. Cheng, C. Yan, J. Yang, Q. Zhang, S. Li, K. Zhao, X. Lu, C. Jiang, Nucl. Instrum. Methods Phys. Res. A **336**, (1993) 150.

[21].   I.J. Thompson, Comput. Phys. Rep. **7**, 1998 167.

[22].   K.O. Groeneveld, A. Richter, U. Strohbusch, B. Zeidman, Phys. Rev. Lett. **27**, 1971 1806.

[23].   G. Bassani, N. Saunier, B.M. Traore, J. Raynal, A. Foti, G. Pappalardo, Nucl Phys A **189**, (1972) 353.

[24].   S. Cohen, D. Kurath, Nucl. Phys. **73**, (1965) 1.

[25].   S. Cohen, D. Kurath, Nucl. Phys. A **101**, (1967) 1.

[26].   N.K. Timofeyuk, Phys. Rev. C **81**, (2010) 064306.

[27].   D.J. Millener, *in Topics in Strangeness Nuclear Physics, Lecture Notes in Nuclear Physics*, Vol. 724, (edited by P. Bydzovsky, A. Gal, J. Mares, Springer, New York, 2007), p. 31.

[28].   Z.H. Li, W.P. Liu, X.X. Bai, B. Guo, G. Lian, S.Q. Yan, B.X. Wang, S. Zeng, Y. Lu, J. Su, Y.S. Chen, K.S. Wu, N.C. Shu, T. Kajino, Phys. Rev. C **71**, (2005) 052801(R).

[29].   J. Su, Z.H. Li, B. Guo, W.P. Liu, X.X. Bai, S. Zeng, G. Lian, S.Q. Yan, B.X. Wang, Y.B. Wang, Chin. Phys. Lett. **23**, (2006) 55.

[30].   J. Su, Z.H. Li, B. Guo, X.X. Bai, Z.C. Li, J.C. Liu, Y.B. Wang, G. Lian, S. Zeng, B.X. Wang, S.Q. Yan, Y.J. Li, E.T. Li, Q.W. Fan, W.P. Liu, Chin. Phys. Lett. **27**, (2010) 052101.

[31].   O. Camargo, V. Guimarães, R. Lichtenthäler, V. Scarduelli, J.J. Kolata, C.A. Bertulani, H. Amro, F.D. Becchetti, J. Hao, E.F. Aguilera, D. Lizcano, E. Martinez-Quiroz, H. Garcia, Phys. Rev. C **78**, (2008) 034605

[32].   J. Görres, S. Graff, M. Wiescher, R.E. Azuma, C.A. Barnes, H.W. Becker, T.R. Wang, Nucl. Phys. A **517**, (1990) 329.

[33].   C.A. Bertulani, Comput. Phys. Commun. **156**, (2003) 123.

[34].   C.E. Rolfs, W.S. Rodney, Nucl. Phys. A **235**, (1974) 450.

[35].   V.J. Zeps, E.G. Adelberger, A. Garcia, C.A. Gossett, H.E. Swanson, W. Haeberli, P.A. Quin, J. Sromicki, Phys. Rev. C **51**, (1995) 1494.

[36].   C. Angulo, M.Arnould, M. Rayet, P. Descouvemont, D. Baye, C. Leclercq-Willain, A. Coc, S. Barhoumi, P. Aguer, C. Rolfs, R. Kunz, J.W. Hammer, A. Mayer, T. Paradellis, S. Kossionides, C. Chronidou, K. Spyrou, S. Degl'Innocenti, G. Fiorentini, B. Ricci, S. Zavatarelli, C. Providencia, H. Wolters, J. Soares, C. Grama, J. Rahighi, A. Shotter, M. L. Rachti, Nucl. Phys. A **656**, (1999) 3.

Nuclear astrophysics experiments in collaboration with ruhr university

ZENG Sheng (曾晟)[1], F. RAIOLA[2], T. SPILLANE[2], LIAN Gang (连刚)[1],
WANG Baoxiang(王宝祥)[1], YAN Shengquan (颜胜权)[1] & C. ROLFS[2]

[1]*China Institute of Atomic Energy, Beijing 102413, China*
[2]*Ruhr University, Bochum D 44780, Germany*

(To be Published.)

In collaboration with Ruhr University, the reactions $^{12}\text{C}(^{12}\text{C},\alpha)^{20}\text{Ne}$ and $^{12}\text{C}(^{12}\text{C},\text{p})^{23}\text{Na}$ have been studied from E = 2.10 to 4.75 MeV by γ-ray spectroscopy using a C target of ultralow hydrogen contamination. The deduced astrophysical S(E) factor exhibits new resonances at E $\leqslant$ 3.0 MeV, in particular a strong resonance at E = 2.14 MeV, which lies at the high-energy tail of the Gamow peak. The resonance increases the reaction rate of the α-channel by a factor 5 near T = 8×10^8 K.

For a deep understanding of the electron screening effects, we cooperated with the astrophysics group of Ruhr University to study the electron screening in the d(d,p)t reaction for a series of deuterated metal-, insulator- and semiconductor targets. As compared to measurements performed with a gaseous D_2 target, a large effect has been observed in most metals, while a comparatively small effect is found in the insulators and semiconductors. Subsequently, temperature dependence of the electron screening in the d(d,p)t reaction has been studied for the deuterated metal Pt and Co. The enhanced electron screening decreases with increasing temperature. The data represent the first observation of a temperature dependence of a nuclear cross section.

Keywords: nuclear astrophysics, $^{12}\text{C} + ^{12}\text{C}$ fusion reaction, direct measurement, electron screening

1 Introduction

In a large variety of astrophysical objects, nuclear reactions play a pivotal role for both energy production and nuclearsynthesis. Nuclear astrophysics is an interdisciplinary branch of physics involving close collaboration among researchers in various subfields of nuclear physics and astrophysics, That includes stellar modeling, measurement and theoretical estimation of nuclear reaction rates, stable and explosive stellar burning phases. Also the effects of the environment on the height of the coulomb barrier (electron screening) are part of this field. In general terms, nuclear astrophysics aims to understand the origin of the chemical elements and the energy generation in stars.The Dynamitron-Tandem-Laboratorium(DTL) of the Ruhr-University Bochum are working on most of these fields. Nuclear reactions, such as $^3\text{He}(d, p)^4\text{He}$, D(d, p)T, $^7\text{Li}(p, \alpha)^4\text{He}$, $^6\text{Li}(p, \alpha)^3\text{He}$, $^3\text{He}(\alpha, \gamma)^7\text{Be}$, $^{12}\text{C}(\alpha, \gamma)^{16}\text{O}$, $^{12}\text{C}(^{12}\text{C}, \alpha)^{20}\text{Ne}$, $^{12}\text{C}(^{12}\text{C}, p)^{23}\text{Na}$ and so on, were studied using 100kV, 500kV, 4MV accelerators of DTL respectively. The present Letter reports on such nuclear astrophysics experiments in Collaboration with Ruhr University.

2 $^{12}\text{C} + ^{12}\text{C}$ Fusion Reactions

The reactions $^{12}\text{C}(^{12}\text{C}, \alpha)^{20}\text{Ne}$ (Q = 4.62 MeV) and $^{12}\text{C}(^{12}\text{C}, p)^{23}\text{Na}$ (Q = 2.24 MeV) are referred to as carbon burning in stars, following the stellar hydrogen and helium burning stages [1]. The reactions represent key reactions in nuclear astrophysics since they influence not only the nucleosynthesis of ^{20}Ne and ^{23}Na but also the subsequent evolution of a star, e.g. whether a star evolves into a carbon-detonation supernova or not. Thus, the cross section of these reactions must be known with high accuracy down to the Gamow energy E_G = 1.5 ± 0.3 MeV for a temperature of 5×10^8 K. Using charged-particle or γ-ray spectroscopy the reactions were investigated over a wide range of energies down to the center-of-mass energy E = 2.5 MeV [1, 2, 3, 4, 5]. However, below E = 3.0 MeV the reported cross sections are rather uncertain, because at these energies the presence of ^1H and ^2H in the targets hampered the measurement of the $^{12}\text{C} + ^{12}\text{C}$ process in both spectroscopies. Thus, improved studies required C targets with an ultra-low hydrogen contamination. The present work reports on such studies by γ-ray spectroscopy.

The 4 MV Dynamitron tandem accelerator at the Ruhr-University Bochum provided the ^{12}C beam with up to 40 particle μA on target (at low energies). The energy calibration

and the energy spread of the beam are known to better than 3 keV and equal to 2 keV, respectively [6, 7]. The purity of the C beam is known to be better than 10^{-11}, for O and other light ions[11]. The beam passed through a collimator (diameter ϕ = 4 mm, distance to target = 60 cm) and was stopped at the C target (graphite foil of 1.0 mm thickness and 20 × 20 mm^2 area). The target was mounted on a stainless-steel conflat flange. The conflat beam pipe (ϕ = 4 cm, length = 30 cm) with the target holder was electrically insulated from the upstream beam pipe; they formed the Faraday cup for beam integration, with an estimated error of 3%. A Ge detector was placed at 0° to the beam axis (100% relative efficiency, resolution = 2.4 keV at E_γ= 1.4 MeV, front-face-distance to the target = 2 cm). The setup was surrounded by a 10 cm thick lead shield to suppress the room background in the relevant energy range by a factor 400. Finally, a plastic scintillator was used to veto cosmic-ray induced events in the detector. The accelerator and experiment setup are shoun in Fig. 1.
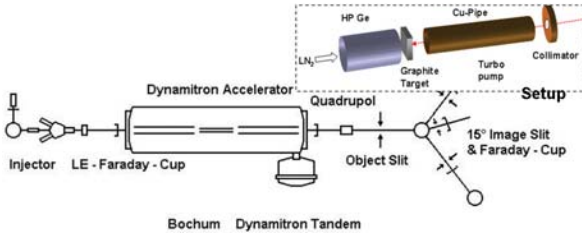
Figure 1: Schematic layout of 4MV Dynamitron tandem accelerator and the experimental setup of ^{12}C + ^{12}C reactions.

The intense ^{12}C beam heated the target to an estimated temperature of 700^oC and we observed - within about 10 minutes of bombardment - a decrease of the hydrogen contamination in the target to a negligible level. Aside from γ-ray lines due to intrinsic activities in the lead and/or target chamber, the spectra are dominated by the lines of interest at 440 and 1634 keV. The specific γ-ray yields of the two lines as a function of beam energy represent a sizable fraction of the total fusion yield (but it varies somewhat with beam energy), with a mean value of about 90% of the α and p channel, according to [4, 8]. It was also found that the two γ-rays exhibit nearly isotropic angular distributions [3]. Thus, we normalized our data to the recommended absolute cross section of [8].

The reaction yield of the infinitely thick C target, $Y^\infty(E)$, was obtained in several runs at E = 2.10 to 4.75 MeV, with energy steps Δ = 25 keV. In order to arrive at a thin-target yield curve, $Y(E)$, the thick-target yield curve was differentiated, i.e. the yield difference between two adjacent points $Y^\infty(E)$ and $Y^\infty(E-\Delta)$ was calculated and divided by Δ. The result is

$$Y(E) = (Y^\infty(E) - Y^\infty(E - \Delta))/\Delta$$
$$= \alpha\varepsilon(E)^{-1}\sigma(E_{eff}) \qquad (1)$$

where E_{eff} is the effective energy over the step $\Delta[1]$, α is the normalization constant, and $\varepsilon(E)$ is the stopping power [9]. The present technique avoids the previous problems of target deterioration and/or carbon deposition when using thin C targets, as discussed in [8]. The resulting cross sections $\sigma(E_{eff})$, i.e. the weighted average of several runs, are illustrated in Fig. 2 in form of the modified astrophysical S(E)* factor [1, 2, 3, 4, 11, 12] with E in units of MeV. The lowest data point corresponds to a cross section of about 20 pb. Screening effects of the atomic electrons with U_e = 5.9 keV [10] lead to a cross section enhancement of 8% at E = 2.2 MeV and has thus been neglected.
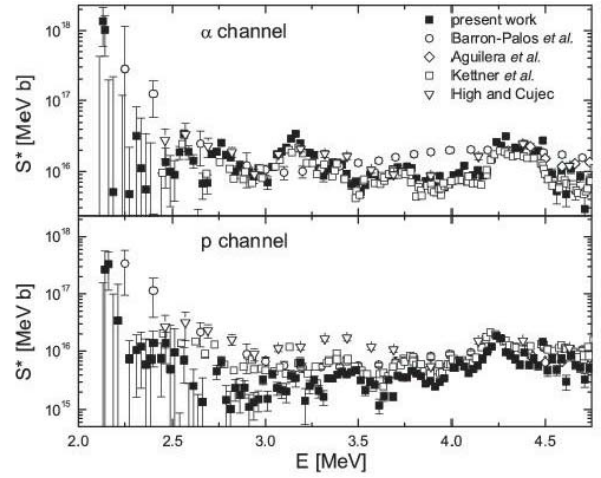
Figure 2: S(E)* factor of the fusion process ^{12}C + ^{12}C for the α and proton channels is compared with previous data obtained by γ-ray spectroscopy.

The data exhibit a pronounced resonance structure, which is in good agreement with previous data at E > 3.0 MeV. The resonance structure continues down to our low-energy limit, where a strong resonance is found at E_R = 2138±3 keV (width Γ_R = 12±4 keV) with a strength $(\omega\gamma)_R$ = 0.23±0.05 and 0.02±0.02 meV for the α- and p-channel,respectively, as deduced from the step in the thick-target yields at this resonance [7]; the quoted errors are mainly of statistical origin and contain the 5% uncertainties of the reference cross sections.

The reaction rate per particle pair for the non-resonant plus resonant parts is given by the expression [1, 11]

$$< \sigma v > = 3.33 \times 10^{-21}\tau^2 exp(-\tau)S^* + 5.54 \times 10^{-13}$$
$$T_6^{-3/2}(\omega\gamma)_R exp(-11.6E_R T_6^{-1})cm^3 s-1 \qquad (2)$$

with $\tau = 839/T_{eff}^{1/3}$ and T_{eff} = T$_6$/(1+ 4.0×10^{-5} T$_6$) where the temperature T$_6$ is in units of 10^6 K, S* is in units of keV b, and $(\omega\gamma)_R$ and E_R are in units of keV. It turns out that the 2.14 MeV resonance increases the α -channel rate by about a factor 8 near T = 8×10^8 K. Astrophysical consequences of this higher rate have to await the results of stellar model calculations.
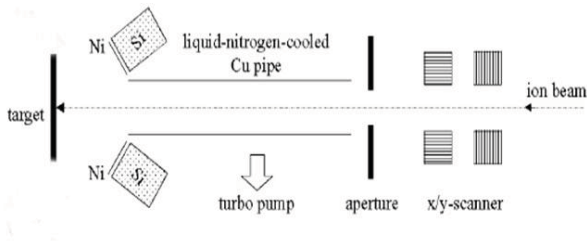
Figure 3: Schematic diagram of the experimental setup of D(d, p)T reaction.

Figure 4: Periodic table showing the studied elements, where those with small effect ($U_e < 100$ eV) are lightly shadowed and those with large effect ($U \geqslant 100$ eV) are heavily shadowed.

3 Electron Screening in d(d, p)t for Deuterated Targets

It is well known that the cross section $\sigma(E)$ of a charged-particle-induced nuclear reaction is enhanced at subcoulomb energies by the electron clouds surrounding the interacting nuclides, with an enhancement factor [1]

$$
\begin{aligned}
f_{lab} &= \sigma_s(E)/\sigma_b(E) = S_s(E)/S_b(E) \\
&\approx \sigma_b(E + U_e)/\sigma_b(E) \\
&\approx [E/(E + U_e)]exp(\pi\eta U_e/E)) \tag{3}
\end{aligned}
$$

where $\sigma_s(E)$ and $\sigma_b(E)$ are the cross section for screened nuclei and for bare nuclei, E is the center-of-mass energy, $\eta(E)$ is the Sommerfeld parameter, and U_e is the screening potential energy.

The equipment, procedures, and data analysis have been described elsewhere [13, 14, 15, 16]. Briefly, the 100 kV accelerator provided the 5 μA D3$^+$ beam. The beam direction and spot on target were defined by 2 apertures(fig 3). A liquid-nitrogen-cooled Cu tube extended from near the downstream aperture to within 5 cm of the target. Four Si detectors (active area = 600 mm^2) were installed at a laboratory angle $\theta = 130^o$ around the beam axis, each at a distance

of 5 cm from the target and covered with a 0.75 μm thick Ni foil to stop the intense flux of elastically scattered particles. In a first step, the surface of a given sample was cleaned in situ by Kr sputtering at 35 keV removing typically about 300 monolayers. As the second step, the sample was deuterated at a given deuteron energy until a saturated yield was reached. This implantation procedure was repeated over the full energy range of the planned experiment taking typically about 4 days of running. Finally, The reaction yield of the thick target, Y (E), was obtained in several runs at $E_d = 5$ to 30 keV, with energy steps $\Delta = 0.5$ keV at $E_d = 5$ to 10 keV and $\Delta = 1.0$ keV at $E_d = 10$ to 30 keV. The thin-target yield can be obtained from the differential of the thick-target yield according to equation 1. The screening potential energy U_e was obtained by fitting the data with the enhancement factor of equation 3. We tested also the stability of the solubility against diffusion by switching the deuteron beam off for an extended period (typically 6 hours); the subsequent yield measurement was unchanged within experimental uncertainty indicating a stable solubility, both at room temperature and elevated temperatures.

The electron screening in d(d,p)t was studied for deuterated metals, insulators, and semiconductors, i.e. 58 samples in total [13, 14]. A comparison of the U_e values with the periodic table indicates a common feature (fig. 4): as compared to measurements performed with a gaseous D_2 target ($U_e = 25$ eV [17]), a large screening was observed in the metals (of order $U_e = 300$ eV), while a small (gaseous) screening was found for the insulators and semiconductors. An exception was found for the metals of groups 3 and 4 of the periodic table and the lanthanides, which showed a small screening; this is related to their high hydrogen solubility y, of the order of one, that gives the deuterated targets of these metals the properties of insulators. We measured all metals of groups 3 and 4 and the lanthanides again at T = 200oC. In fact, at T = 200°, all these metals exhibited a large reduction in solubility and thus a large screening became observable[15, 16]. As a consistency test we also studied the insulator C at T = 200°. The solubility decreased from 0.35 (T = 20 ^{o}C) to 0.15, but no enhanced screening was observed.

An explanation of the large screening was suggested by the plasma screening of Debye applied to the quasi-free metallic electrons [13]. Quoted the electron Debye radius one can obtain

$$
\begin{aligned}
U_e &= \frac{Z_1 Z_2 e^2}{R_{Debye}} \\
&= Z_1 Z_2 e^2 (\frac{n_{eff}\rho_\alpha e^2}{\varepsilon_0 kT})^{1/2} \tag{4}
\end{aligned}
$$

where n_{eff} is the number of valence electrons per metallic atom, and ρ_α is the atomic density. A critical test of the Debye model is the predicted temperature dependence $U_e(T) \propto T^{-1/2}$.

We measured the screening effect for the deuterated metal Pt at a sample temperature between T = 20 ^{o}C and 340 ^{o}C,

and for Co at T = 20 ^{o}C and 200 ^{o}C. Both metals have a solubility of a few percent at all T of the present work. The results for Co and Pt are given in Table 1 and the U_e(T) values for Pt are plotted in Fig. 5 together with the expected dependence U_e(T) T-1/2 (dotted curve) [15, 16]. All data show a decrease of the screening, i.e. the U_e value, with increasing temperature. Over the present temperature range, the reported Hall coefficient for Pt increases by about 20% [18] leading to a corresponding decrease in n_{eff}, which we took into account (solid curve in Fig. 5); there is good agreement between observation and expectation. The data represent the first observation of a temperature dependence of a
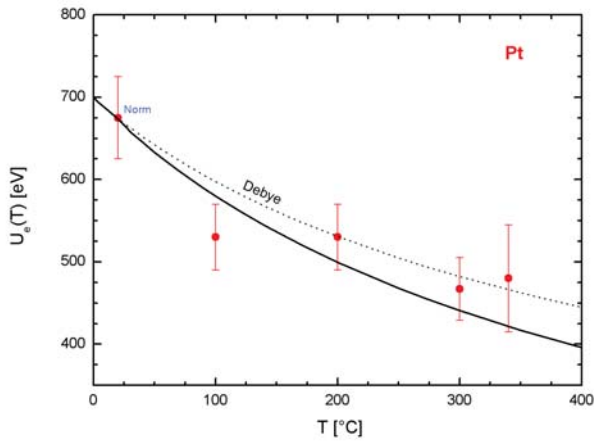
Figure 5: Temperature dependence of U_e for the deuterated Pt target.. The dotted curve represents the prediction of the Debye model (equation 4) and the solid curve includes the observed T-dependence of the Hall coefficient [18], i.e. n_{eff}(T).

4 Conclusions

The reactions ^{12}C(^{12}C, α)^{20}Ne and ^{12}C(^{12}C, p)^{23}Na have been studied from E = 2.10 to 4.75 MeV by γ-ray spectroscopy. The deduced astrophysical S(E)* factor exhibits new resonances at E $\leqslant$ 3.0 MeV, in particular a strong resonance at E = 2.14 MeV. The resonance increases the reaction rate of the α-channel by a factor 5 near T = 8×10^8 K. With an underground accelerator, even with an unshielded, but improved detection system such as a Ge crystal ball, a

beam current of 200 pμA, and long running times, it appears possible to perform measurements over the energy range of the Gamow peak.

All data on the enhanced electron screening in deuterated metals can be explained quantitatively by the Debye model applied to the quasi-free metallic electrons. An improved theory is highly desirable to explain why the simple Debye model appears to work so well. Without such a theory, one may consider the Debye model as a powerful parametrisation of the data.

References

[1]. Rolfs C, Rodney W S. 1988, Cauldrons in The Cosmos. Chicago USA: University of Chicago Press.

[2]. Mazarakis M G, Stephens W E. 1973, Phys. Rev. C, 7: 1280.

[3]. Kettner K U, Lorenz-Wirzha H, Rolfs C. 1977, Phys. Rev. Lett., 38: 337.

[4]. Becker H W, Kettner K U, Rolfs C, et al. 1981, Z. Phys. A, 303: 305

[5]. High M D, Cujec B. 1977, Nucl. Phys. A, 282: 181

[6]. Wüstenbecker S, Ebbing H, Schulte W H, et al. 1989, Nucl. Instrum. Method A, 279: 448

[7]. Spillane T. The Reaction Rates of Charged-Particle Exit Channels from the Fusion Reaction ^{12}C+^{12}C at Energies Below the Coulomb Barrier. Doctor Dissertation. Connecticut: University of Connecticut, 2007 (to be published)

[8]. Aguilera E F, Resales P, Martinez-Quiroz E, et al. 2006, Phys. Rev. C, 73: 064601

[9]. Andersen H, Ziegler J F. 1977,The Stopping and Ranges of Ions in Matter and SRIM-2003. New York: Pergamon Press,

[10]. Assenbaum H J, Langanke K, Rolfs C. 1987, Z. Phys. A, 1987, 327: 461

[11]. Spillane T, Raiola F, Rolfs C, et al. 2007, Phys. Rev. Lett., 98:122501

[12]. Zeng S, Spillane T, Raiola F, et al. 2009, Science China, 39: 801(in Chinese)

[13]. Raiola F, Gang L, Bonomo C, et al. 2004, Eur. Phys. J., A19: 283

[14]. Raiola F, Migliardi P, Gang L et al. 2002, Phys. Lett. B, 547: 193

[15]. Raiola F, Burchard B, Fulop Z, et al. 2005, J. Phys. G, 31: 1141

[16]. Zeng S, Raiola F, Burchard B, et al. 2005, HEP NP, 29: 1131(in Chinese)

[17]. Greife U, Gorris F, Junker M, et al. 1995, Z. Phys A, 351:107

[18]. Landolt-B?rnstein Numerical Data and Functional Relationships in Science and Technology. Berlin: Springer-Verlag, 1959. 166

Silicon abundances in nearby stars from the Si I infrared lines

J.R. Shi[1], M. Takada-Hidai[2], Y. Takeda[3], K.F. Tan[1], S.M. Hu[4], G. Zhao[1] & C. Cao[4]

[1]*National Astronomical Observatories, Chinese Academy of Sciences, Beijing 100012, P. R. China*
[2]*Liberal Arts Education Center, Tokai University, 4-1-1 Kitakaname, Hiratsuka, Kanagawa 259-1292, Japan*
[3]*National Astronomical Observatory of Japan 2-21-1 Osawa, Mitaka, Tokyo 181-8588, Japan*
[4]*Shandong Provincial Key Laboratory of Optical Astronomy and Solar-Terrestrial Environment, Shandong University at Weihai, P. R. China*

We have used high resolution, high signal-to-noise ratio infrared spectra from the Subaru Telescope atop Mauna Kea. Line forma-
tion calculations of Si I infrared lines in the atmospheres of nearby stars are presented. All abundance results of [Si/Fe] are derived
from local thermodynamic equilibrium (LTE) and NLTE statistical equilibrium calculations and spectrum synthesis methods. We
found that NLTE effects for Si I infrared lines are even important for metal-rich stars (>0.1 dex). And the NLTE effects may depend
on the surface gravities, e.g. they tend to be large for giant stars. A good agreement of silicon abundances between the optical and
infrared lines are obtained when the NLTE effects included, while a large difference found for the LTE results. The derived silicon
abundances show overabundant for metal-poor stars.

Keywords: Line: formation - Line: profiles - Stars: abundances - Stars: late-type – Galaxy: evolution.

PACS: 25.60.-t, 25.40.Ny, 26.20.Fj, 26.30.Ca

1 Introduction

Silicon is an important α-capture element, whose abundances
play a key role in studying the Galactic chemical evolution.
It is believed that silicon is made during oxygen and neon
burning in massive stars [35, 23], and type Ia supernove also
produce significant amounts of silicon [33, 15, 30, 20].

The previous abundance determinations of Si have been
based on the optical lines and the assumption of local thermo-
dynamic equilibrium (LTE). For extreme-metal poor stars,
the only optical lines at 3905 and 4103 Å can be used to
determine Si abundances. Recently, it is found that the in-
frared Si II lines can also be observed [16] for such type stars.
However, we noted that the infrared lines are sensitive to the
NLTE effects even in the solar spectrum [24]. Thus, it is
important to investigate the NLTE effects for these infrared
lines in metal-poor stars.

The present work is based on a sample of nearby stars
and aims at exploring their [Si/Fe] abundance ratios based
on the Si II infrared lines, applying a full spectrum synthe-
sis based on level populations calculated from the statistical
equilibrium equations, and to investigate whether similar sil-
icon abundances can be obtained from the infrared and opti-
cal lines. In Sect. 2 we present the observational technique
and the atmospheric models and stellar parameters are dis-
cussed in Sect. 3. NLTE line formation is discussed in Sect.
4. The results and comparison with these of the optical lines
are shown in Sec. 5. The discussion and conclusions are

presented in Sect. 6.

2 Observations

The high-resolution spectra analyzed in our present investi-
gation were obtained with the Infrared Camera and Spectro-
graph [17, 32, IRCS]) along with the 188-element curvature-
based adaptive optics system (AO188), which is mounted on
the IR Nasmyth focus of the 8.2 m Subaru Telescope atop
Mauna Kea on 2009 July 29 and 30 (UT). The observations
cover a spectral range from 10 100 to 11 900 Å. The spec-
tra were taken in the echelle spectrograph mode of IRCS,
which is equipped with a Raytheon 1024×1024 InSb array
with an Aladdin II multiplexer. The spectral resolution of R
is $\simeq$ 20 000. All stars were observed with S/N ~ 100 to 300.

Data extraction followed the standard "echelle" package
of the software IRAF2 including subtraction for background
cancellation, flat-fielding, bad-pixel correction, cosmic-ray
events correction, scattered-light subtraction, aperture ex-
traction, wavelength calibration, co-adding of spectrum
frames, and continuum normalization [28, 29, for detals].

3 Method of calculation

3.1 Model atmospheres

We use line-blanketed LTE model atmospheres, generated by
[11]. The main characteristics are: the iron opacity was cal-

culated with the improved meteoritic value log ε_{Fe} = 7.51 [2]; opacities for metal-poor stars with [Fe/H] < −0.6 were calculated using α-element abundances enhanced by 0.4 dex, and the mixing-length parameter l/H_p was adopted to be 0.5, in order to determine consistent temperatures for H_α and the higher Balmer lines [10].

Table 1: Atomic data of silicon infrared lines*.

λ [Å]	Transition	$\log gf$	$\log C_6$
10288.90	$4s^3P_0^o - 4p^3S_1$	−1.65	−30.661
10371.30	$4s^3P_1^o - 4p^3S_1$	−0.85	−30.659
10585.17	$4s^3P_2^o - 4p^3S_1$	−0.14	−30.659
10603.45	$4s^3P_1^o - 4p^3P_2$	−0.34	−30.677
10627.66	$4p^1P_1 - 4p^3P_2^o$	−0.39	−30.692
10661.00	$4s^3P_0^o - 4p^3P_1$	−0.34	−30.687
10689.73	$4p^3D_1 - 4d^3F_2^o$	−0.07	−29.964
10694.27	$4p^3D_2 - 4d^3F_3^o$	+0.06	−29.944
10727.43	$4p^3D_3 - 4d^3F_4^o$	+0.25	−29.907
10749.40	$4s^3P_1^o - 4p^3P_1$	−0.20	−30.689
10784.57	$4p^3D_2 - 4d^3F_2^o$	−0.69	−29.965
10786.88	$4s^3P_1^o - 4p^3P_0$	−0.34	−30.691
10827.10	$4s^3P_2^o - 4P^3P_2$	+0.21	−30.677
10843.87	$4P^1P_1 - 4d^1D_2^o$	−0.08	−30.145
10882.83	$4p^3D_3 - 4d^3F_3^o$	−0.80	−29.945
10979.34	$4s^3P_2^o - 4P^3P_1$	−0.55	−30.688

*$\log gf$ values have been determined from NLTE solar spectrum fits, and damping constants $\log C_6$ for Si II infrared lines are computed according to the table from [3, 4] and [5].

3.2 Stellar parameters

We adopt the stellar parameters for the sample stars determined by [13, 14] and [26], where the effective temperatures are derived from the wings of the Balmer lines based on the hydrogen resonance broadening calculated with [1] theory. The surface gravities are based on the HIPPARCOS parallaxes. Iron abundances are obtained from Fe II lines, and the microturbulence velocities are estimated by requiring that the iron abundance derived from Fe II lines should not depend on equivalent width. For HD 131156, high-resolution and high S/N spectra were obtained with the fiber optics échelle spectrograph attached to the 2.16 m telescope at National Astronomical Observatories (Xinglong China) on 2011 August 3. The observations cover a spectral range from 3700 Å to 9200 Å. The spectra were exposed on a 4096^2 CCD chip with 12 μm pixel size, providing a spectral resolving power of R ∼ 50 000. It were observed six times with S/N ∼ 200. While for G 29-23, fortunately, high-resolution and high S/N spectra covering a wide wavelength range were available from the archived ESO VLT/UVES [9] spectra database. In order to keep our analysis consistent, we determined the stellar parameters of these two stars using the method described above. The estimated uncertainties for the temperature, sur-

face gravity, metal abundance, and microturbulence velocity are for most of the stars as ±80 K, 0.10 dex, 0.05 dex and 0.2 km s^{-1}, respectively.

3.3 Atomic line data

Table 1 lists the relevant line data with their final solar NLTE fit values [24]. Collisional broadening through van der Waals interaction with hydrogen atoms is important for infrared Si lines. As already discussed in [12, 13], the resulting values of the van der Waals damping constants are mostly near those calculated according to the tables from [3, 4] and [5] . In our analysis, the absolute value of the oscillator strengths is unimportant because the abundances are evaluated in a fully differential way with respect to the sun.

4 NLTE calculations

4.1 Atomic model

The silicon model atom includes the most important levels of Si I and Si II and comprises 132 terms of Si I, 41 terms of Si II, plus the Si III ground state. The atomic properties are documented in [24, 25].

All calculations are carried out with a revised version of the DETAIL program [8] using accelerated lambda iteration [12, 13, for details].

4.2 NLTE effects

Fig.1 shows the behavior of the departure coefficients $b_i = n_i^{NLTE}/n_i^{LTE}$ for the model atmosphere of HD 19445. Here, n_i^{NLTE} and n_i^{LTE} are the statistical equilibrium and thermal (Saha-Boltzmann) number densities, respectively. The departure coefficients of the important levels of Si I and Si II ground state are shown as a function of continuum optical depth (τ_{5000} referring to λ = 5000 Å) in the model atmosphere of HD 19445.
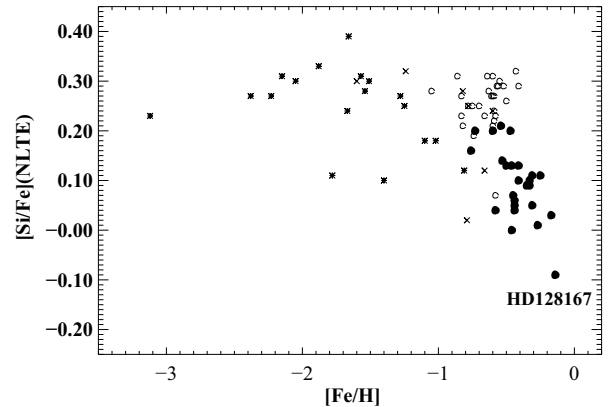
Figure 1: Departure coefficients as a function of $\log \tau$ for selected levels of Si I and Si II in the model atmosphere of

HD 19445.

The abundance analyses of Si II infrared lines clearly show the NLTE effects. It should be noted that the NLTE effects differ from line to line, the strong 10 585 and 10 827 Å lines show large NLTE effects for our program stars, while the weak lines show the smallest NLTE abundance effects (< 0.02 dex). The differences of abundance between LTE and NLTE analyses for the two strong Si II lines at 10 585 and 10 827 Åare plotted in Fig. 2 as a function of metal abundance, temperature and surface gravity, respectively. There is a trend that the NLTE effects increase with decreasing surface gravity. However, it should be noted that we only include one giant star (HD 122563) in our sample, this trend should be confirmed by more sample stars.
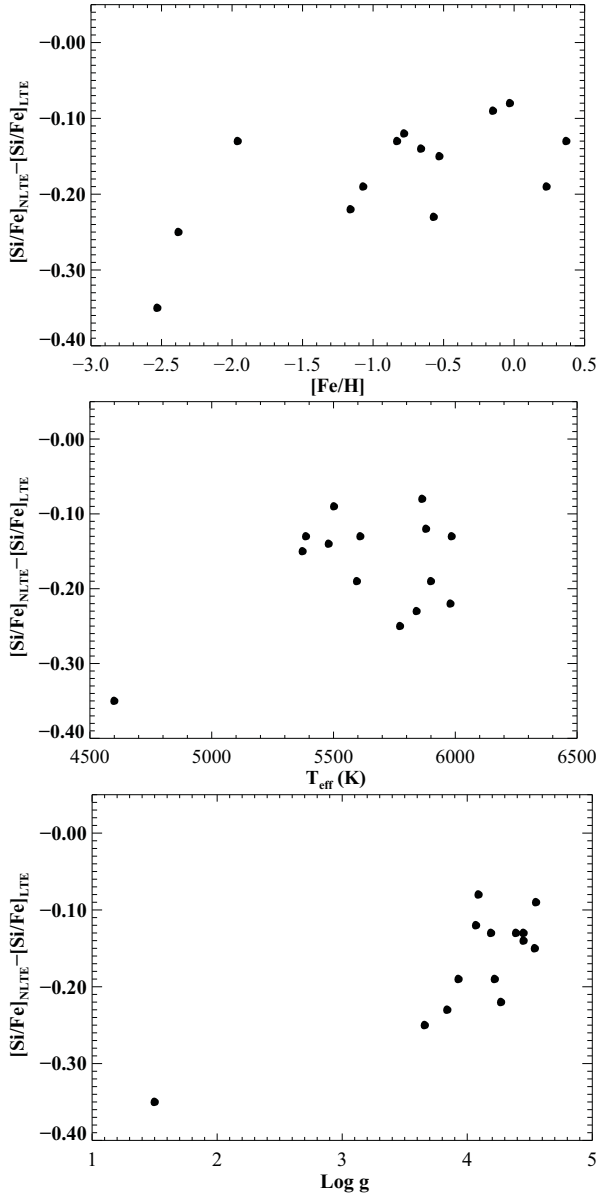
Figure 2: Difference of [Si/Fe] abundance ratios calculated under NLTE and LTE assumptions for the two strong Si II lines (10 585 and 10 827 Å) as a function of metal abundance (a), temperature (b), and surface gravity (c).

5 Results

5.1 Stellar silicon abundances

The abundance determinations for our program stars are made using spectral synthesis. Some examples of the profile fitting are presented in Fig.3. Consistent abundance results are obtained between different lines when NLTE effects included, the final abundance scatter of single lines is between 0.01 and 0.12. The derived abundance results based on both the infrared and optical lines are presented in Table 2.

5.2 Comparison with the optical results

We have also been determined the silicon abundances from the optical lines based on LTE and NLTE analyses for these stars [27, 34]. In Fig.4, we compare the [Si/Fe] values determined from infrared and optical lines for our program stars. A comparison of the abundances shows that consistent results are obtained when the NLTE effects included, while large differences can be found for the LTE results.
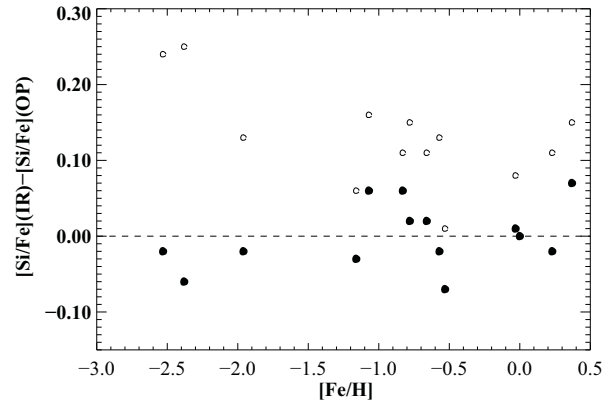
Figure 3: The differences of silicon abundance between the infrared and optical lines. open circles (○) are LTE results, while filled circles (●) for NLTE results. It is obviously that the LTE results give large difference between the Si abundances based on optical and infrared lines.

6 Discussion and Conclusions

We have determined silicon abundances for 15 nearby stars, spanning the range -2.6 < [Fe/H] <~0.4, based on the infrared lines. All abundances are derived from NLTE statistical equilibrium calculations. Fig.4 displays the behaviour of

the [Si/Fe] ratio with the metal abundance for all stars considered in this paper. Based on our results we come to the following conclusions:

1. Silicon is overabundant for metal-poor stars, and the LTE results overestimate the Si abundances.

2. The NLTE effects vary with different infrared lines. The weak lines are insensitive to NLTE effects, while the strong lines show large NLTE effects. NLTE leads to enhanced absorption in the line cores and negative abundance corrections over the range of stellar parameters studied here. This effects may depend on the surface gravity, thus tend to be large for giant stars.

3. Our results show that NLTE largely removes obvious discrepancies between optical and infrared lines obtained under an LTE assumption.
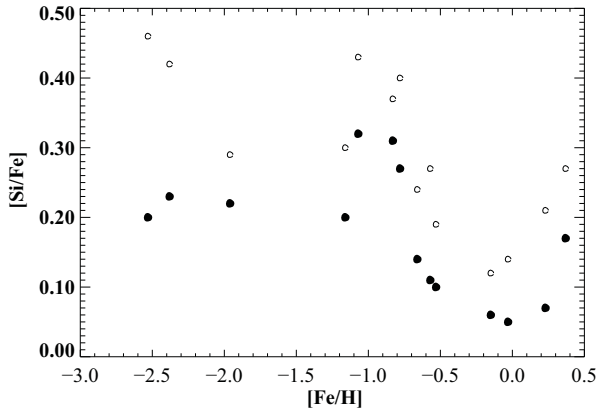
Figure 4: Abundance ratios [Si/Fe] as a function of [Fe/H]. Filled circles (•) represent the NLTE results, while open circles (○) for LTE results. The LTE results overestimate the Si abundances.

References

[1]. Ali, A. W., & Griem, H. R., 1966, Phys. Rev., 144, 366

[2]. Anders, E., & Grevesse, N. 1989, Geochim. Cosmochim. Acta, 53, 197

[3]. Anstee, S. D., & O'Mara, B. J. 1991, MNRAS, 253, 549

[4]. Anstee, S. D., & O'Mara, B. J. 1995, MNRAS, 276, 859

[5]. Barklem, P. S., Piskunov, N., & O'Mara, B. J. 2000b, A&AS, 142, 467

[6]. Baumüller, D., Gehren, T. 1996, A&A, 307, 961

[7]. Bergemann, M., & Cescutti, G. 2010 A&A, 522, 9

[8]. Butler, K., Giddings, J. Newsletter on the analysis os astronomical spectra No. 9, University of London

[9]. Dekker, H., DÓdorico, S., Kaufer, A., Delabre, B., Kotzlowski, H. 2000, Proc. SPIE, 4008, 534

[10]. Fuhrmann, K., Axer, M., Gehren, T. 1993, A&A, 271, 451

[11]. Fuhrmann, K., Pfeiffer, M., Frank, C. et al. 1997, A&A, 323, 909

[12]. Gehren, T., Butler, K., Mashonkina, L., Reetz, J., & Shi, J. R. 2001, A&A, 366, 981

[13]. Gehren, T., Liang, Y. C., Shi, J. R. Zhang, H. W., & Zhao, G. 2004, A&A, 413, 1045

[14]. Gehren, T., Shi, J. R., Zhang, H. W., Zhao, G., & Korn, A. J. 2006, A&A, 451, 1065

[15]. Iwamoto, K., Brachwitz, F., Nomoto, K., Kishimoto, N., Umeda, H., Hix, W. R., & Thielemann, F.-K. 1999, ApJS, 125, 439

[16]. Jönsson, H., Ryde, N., Nissen, P. E., Collet, R., Eriksson, K., Asplund, M., & Gustafsson, B. A&A, 2011, 530, 144

[17]. Kobayashi, N., et al. 2000, Proc. SPIE, 4008, 1056

[18]. Kobayashi, C., Umeda, H., Nomoto, K., Tominaga, N., & Ohkubo, T., 2006, ApJ, 653, 1145

[19]. Korn, A., Shi, J. R., & Gehren, T. 2003 A&A, 407, 691

[20]. Maeda, K., Röpke, F. K., Fink, M., Hillebrandt, W., Travaglio, C., & Thielemann, F.-K. 2010, ApJ, 712, 624

[21]. Mashonkina, L., Gehren, T., Shi, J. R., Korn, A., & Gruup, F. 2011, A&A, accepted

[22]. Nomoto, K., Iwamoto, K., Nakasato, N., Thielemann, F.-K., Brachwitz, F., Tsujimoto, T., Kubo, Y., & Kishimoto, N. 1997, Nucl. Phys. A, 621, 467c

[23]. Ohkubo, T., Umeda, H., Maeda, K., Nomoto, K., Suzuki, T., Tsuruta, S., & Rees, M. J. 2006, ApJ, 645, 1352

[24]. Shi, J. R., Gehren, T., Butler, K., Mashonkina, L., & Zhao, G. 2008, A&A, 486, 303

[25]. Shi, J. R., Gehren, T., Mashonkina, L., & Zhao, G. 2009, A&A 503, 533

[26]. Shi, J. R., Gehren, T., & Zhao, G. 2004, A&A 423, 683

[27]. Shi, J. R., Gehren, T., & Zhao, G. 2011, A&A in press

[28]. Takeda, Y., Takada-Hidai, M. 2011a, PASJ, 63, 537

[29]. Takeda, Y., Takada-Hidai, M. 2011b, PASJ, 63, 547

[30]. Thielemann, F. K., Argast, D., Brachwitz, F., Martinez-Pinedo, G., Rauscher, T., Liebend"orfer, M., Mezzacappa, A., H"oflich, P., & Nomoto, K. 2002, ApSS, 281, 25

[31]. Timmes, F. X., Woosley, S. E., Weaver, T. A. 1995, ApJS, 98, 617

[32]. Tokunaga, A. T., et al. 1998, Proc. SPIE, 3354, 512

[33]. Tsujimoto, T., Nomoto, K., Yoshii, Y., Hashimoto, M., Yanagida, S., & Thielemann, F.-K, 1995, MNRAS, 277, 945

[34]. Wang, X., Shi, J.R., Li, J., Gehren, T., & Zhao G. 2001, in prepareration

[35]. Woosley, S. E., Weaver, T. A., 1995, ApJS, 101, 181

Table 2: Stellar silicon LTE and NLTE (for each star, the first and the second row, respectively) abundances given relative to the iron LTE abundances derived from the Fe II lines[*].

Name	T_{eff}	log g	[Fe/H]	ξ	[Si I $_{\text{LTE}}$/Fe] (ir)	[Si I $_{\text{NLTE}}$/Fe] (ir)	[Si I $_{\text{LTE}}$/Fe] (opt)	[Si I $_{\text{NLTE}}$/Fe] (opt)
G 29-23	6140	4.04						
G 64-37	6390	4.27						
HD 6582	5387	4.45	-0.83	0.89	0.37±0.040	0.31 ± 0.020	0.26± 0.033	0.25 ± 0.031
HD 10700	5373	4.54	-0.53	0.80	0.19±0.044	0.10 ± 0.024	0.18± 0.036	0.17 ± 0.032
HD 19445	5985	4.39	-1.96	1.50	0.29±0.050	0.22 ± 0.037	0.16± 0.005	0.24 ± 0.020
HD 122563	4600	1.50	-2.53	1.90	0.46±0.060	0.20 ± 0.011	0.34± 0.005	0.22 ± 0.050
HD 131156	5502	4.55	-0.15	0.78	0.12±0.040	0.06 ± 0.027	±	±
HD 140283	5773	3.66	-2.38	1.50	0.42±0.035	0.23 ± 0.016	0.34± 0.005	0.29 ± 0.030
HD 141004	5864	4.09	-0.03	1.05	0.14±0.046	0.05 ± 0.024	0.06± 0.034	0.04 ± 0.026
HD 142373	5841	3.84	-0.57	1.24	0.27±0.056	0.11 ± 0.020	0.14± 0.018	0.13 ± 0.023
HD 148816	5880	4.07	-0.78	1.20	0.40±0.019	0.27 ± 0.013	0.25± 0.042	0.25 ± 0.043
HD 161797	5596	3.93	+0.23	1.17	0.21±0.072	0.07 ± 0.023	0.10± 0.033	0.09 ± 0.038
HD 182572	5610	4.19	+0.37	1.01	0.27±0.044	0.17 ± 0.026	0.12± 0.024	0.10 ± 0.025
HD 194598	5980	4.27	-1.16	1.60	0.30±0.039	0.20 ± 0.030	0.24± 0.027	0.23 ± 0.026
HD 201891	5900	4.22	-1.07	1.20	0.43±0.041	0.32 ± 0.024	0.27± 0.026	0.26 ± 0.027
HD 224930	5480	4.45	-0.66	0.90	0.24±0.036	0.14 ± 0.027	0.13± 0.029	0.12 ± 0.029

[*] Our NLTE calculations for Fe I/II based on the advanced atomic model (Mashonkina et al. [21]) support the earlier conclusion of Korn et al. ([19]) that the NLTE effects for Fe II lines are negligible.

Table 3: Stellar silicon LTE and NLTE (for each star, the first and the second row, respectively) abundances given relative to the iron LTE abundances derived from the Fe II lines[*].

Name	10288	10371	10585	10603	10627	10661	10689	10694	10727	10749	10784	10786	10827	10843	10882	10979
G 29-23																
G 64-37																
HD 6582	0.30	0.36	0.49	0.38	0.33	0.36	0.38	0.36	0.40	0.39	0.30	0.32	0.46	0.34	0.33	
	0.30	0.32	0.38	0.29	0.28	0.29	0.34	0.31	0.32	0.32	0.30	0.28	0.31	0.27	0.32	
HD 10700	0.10	0.20	0.31	0.13	0.18	0.23	0.20	0.21	0.22	0.20	0.12	0.12	0.22	0.15		
	0.08	0.10	0.12	0.07	0.11	0.12	0.15	0.14	0.11	0.06	0.12	0.07	0.10	0.06		
HD 19445		0.33	0.28	0.24	0.28	0.23		0.23		0.40		0.24	0.36			
		0.28	0.20	0.19	0.26	0.18		0.22		0.28		0.18	0.18			
HD 122563		0.39	0.56	0.44		0.40						0.41	0.53			
		0.21	0.21	0.20		0.20						0.18	0.18			
HD 131156	0.04	0.19	0.24	0.11	0.06	0.16	0.14	0.14	0.11	0.11	0.04	0.11	0.12	0.06		0.10
	0.02	0.09	0.10	0.05	0.03	0.09	0.09	0.08	0.03	0.03	0.03	0.06	0.08	0.01		0.08
HD 140283		0.43	0.46	0.36		0.40							0.47			
		0.26	0.22	0.22		0.24							0.21			
HD 141004	0.06	0.19	0.14	0.12	0.09	0.16	0.20	0.20	0.20	0.12	0.03	0.12	0.19	0.19		
	0.05	0.08	0.09	0.06	0.00	0.05	0.06	0.09	0.06	0.02	0.01	0.02	0.08	0.08		
HD 142373	0.12	0.26	0.34	0.26	0.26	0.33	0.32	0.31	0.31	0.26	0.10	0.23	0.36	0.31		
	0.12	0.10	0.14	0.10	0.12	0.12	0.15	0.14	0.11	0.06	0.08	0.06	0.11	0.11		
HD 148816		0.39	0.40	0.36	0.35	0.44	0.41	0.40	0.40	0.42		0.38	0.40			
		0.27	0.30	0.26	0.28	0.25	0.29	0.26	0.28	0.26		0.26	0.26			
HD 161797	0.00	0.20	0.31	0.13	0.19	0.26	0.25	0.24	0.29	0.26	0.02	0.20	0.26	0.30		
	0.00	0.05	0.12	0.06	0.06	0.12	0.10	0.06	0.07	0.06	0.02	0.06	0.08	0.06		
HD 182572	0.21	0.35	0.31	0.31	0.26	0.34	0.28	0.26	0.25	0.24	0.18	0.18	0.31	0.24		
	0.21	0.21	0.22	0.16	0.14	0.20	0.19	0.16	0.16	0.16	0.15	0.14	0.14	0.13		
HD 194598		0.31	0.38	0.26	0.24	0.26	0.28	0.30	0.32	0.26		0.29	0.44	0.30		
		0.25	0.16	0.18	0.18	0.18	0.22	0.24	0.21	0.15		0.16	0.23	0.22		
HD 201891		0.46	0.50	0.40	0.39	0.38	0.38	0.46	0.45	0.38		0.40	0.49			
		0.36	0.31	0.30	0.34	0.31	0.33	0.36	0.35	0.29		0.29	0.30			
HD 224930		0.25	0.35	0.23	0.19	0.21	0.20	0.24	0.30	0.24		0.18	0.25	0.19		
		0.15	0.17	0.13	0.10	0.10	0.15	0.16	0.20	0.13		0.10	0.15	0.10		

[*] Our NLTE calculations for Fe I/II based on the advanced atomic model (Mashonkina et al. [21]) support the earlier conclusion of Korn et al. ([19]) that the NLTE effects for Fe II lines are negligible.

Statistical equilibrium of silicon in the atmospheres of nearby metal-poor stars

J.R. Shi[1,2], T. Gehren[2] & G. Zhao[1]

[1]*National Astronomical Observatories, Chinese Academy of Sciences, Beijing 100012, P. R. China*
[2]*Universitäts-Sternwarte München, Scheinerstrasse 1, D-81679 München, Germany*

(To be published in Astronomy & Astrophysics)

We discuss the statistical equilibrium of neutral and ionized silicon in the atmospheres of nearby metal-poor stars. We investigated the effects of non-local thermodynamic equilibrium (NLTE) and determined the silicon abundances.

We used high resolution, high signal-to-noise ratio spectra from the FOCES spectragraph at the DSAZ telescope. Line-formation calculations of Si I and Si II in the atmospheres of nearby metal-poor stars are presented. All abundance results are derived from local thermodynamic equilibrium (LTE) and NLTE statistical equilibrium calculations and spectrum synthesis methods. We find that NLTE effects for Si II optical lines are important for warm stars, and that they depend on effective temperature. The Si abundances of thin and thick disc stars follow distinct trends, as in the case of Mg. We find that [Si/Fe] gradually increases as [Fe/H] decreases in thin disc stars, while it remains around at ∼ +0.30 dex for halo and thick disc stars, the halo stars showing larger scatter. The derived dependence between [Si/Fe] and [Fe/H] is inconsistent with the theoretical predictions of published model calculations for the chemical evolution of the Galaxy. The nearly constant [Si/Mg] ratio with some scatter for halo and thick disc stars suggests that the nucleosynthesis of silicon is closely coupled to that of Mg. In addition, our results do not support the suggestion that type Ia supernove produce significant amounts of silicon.

Keywords: Line: formation - Line: profiles - Stars: abundances - Stars: late-type – Galaxy: evolution

1   Introduction

In a similar way to the ^{24}Mg nucleus, ^{28}Si is an important α element, and the abundance ratio Si/Fe in stars can provide valuable insight into the history of Galactic nucleosynthesis. From a stellar nucleosynthesis point of view, this element should have very similar properties to those found in Mg in metal-poor stars (Woosley & Weaver [50]). The central question with respect to silicon is whether ^{28}Si is synthesized by type Ia supernove. The current paradigm is that silicon is produced during oxygen and neon burning in massive stars, hence subsequently ejected by type II supernove (Woosley & Weaver [50]; Umeda et al. [49]; Ohkubo et al. [38]). Type Ia supernove also produce significant amounts of silicon (Tsujimoto et al. [48]; Iwamoto et al. [28], Thielemann et al. [46], Maeda et al. [31]).

Previous abundance determinations of Si have been carried out under the assumption of local thermodynamic equilibrium (LTE). The corresponding results for metal-poor stars have been similar to those for Mg in that both element abundances have a few typical features:

- As found for Mg, there is a clear distinction between [Si/Fe] for thin- and thick disc stars, namely, the thick-

disc is, at a given [Fe/H], more enhanced in [Si/Fe] than the thin disc (Bensby et al. [10], [11]; Reddy et al. [42], [41]).

- The thick disc [Si/Fe] ratios smoothly merge with the halo ratios in the overlapping metallicity range (Fulbright [20]).

In present work, we study a sample of metal-poor stars to explore their [Si/Fe] abundance ratios by applying a full spectrum synthesis based on level populations calculated from the statistical equilibrium equations, and to investigate whether ^{28}Si is contaminated substantially by synthesis in Type Ia supernovae. In Sect. 2, we present the observational technique and the atmospheric models. Stellar parameters are discussed in Sect. 3. NLTE line formation follows in Sect. 4. Our results and comparison with other work are shown in Sec. 5. Our discussion is presented in Sect. 6, and the conclusions are given in Sect. 7.

2   Observations

The high-resolution spectra analysed in our present investigation were obtained with the FOCES fiber optics échelle

spectrograph fed by the 2.2 m telescope of the DSAZ at Calar Alto Observatory during August 2001 and January 2003. The observations cover a spectral range from 3700 Å to 9800 Å in a total of 97 spectral orders. The spectra were exposed on a 2048^2 CCD chip with 24 μm pixel size, providing a spectral resolving power of R ~ 40 000. All stars were observed at least twice with S/N ~ 100 to 200.

Data extraction followed the standard automatic IDL program environment designed for the FOCES spectrograph (Pfeiffer et al. 1998). All échelle images including flat field and ThAr were corrected for bias and scattered light background. Objects and ThAr exposures were extracted and corrected for the flat-field response. Bad pixels were detected and as far as possible removed by comparing two or more single exposures (see Gehren et al. [23], [24] for details).

3   Method of calculation

3.1   Model atmospheres

We use line-blanketed LTE model atmospheres, generated as discussed by Fuhrmann et al. ([18]). The main characteristics are: (1) the iron opacity, which was calculated with the improved meteoritic value log ε_{Fe} = 7.51 (Anders & Grevesse [3]); (2) opacities for metal-poor stars with [Fe/H] < −0.6, which were calculated using α-element (O, Mg, Si, and Ca) abundances enhanced by 0.4 dex; and (3) the mixing-length parameter l/H_p, which was adopted to be 0.5, in order to determine consistent temperatures for Hα and the higher Balmer lines (see Fuhrmann et al. [17]).

3.2   Stellar parameters

We aim to remain consistent with the whole series of our earlier NLTE studies from Baumüller & Gehren ([8]), Zhao et al. ([51]), Zhao & Gehren ([52]) to the most recent paper of Shi et al. ([45], hereafter paper II) and Bergemann & Cescutti ([12]). We therefore adopt the stellar parameters for the sample stars determined by Gehren et al. ([23], [24]), where the effective temperatures are derived from the wings of the Balmer lines based on the hydrogen resonance broadening calculated with the Ali & Griem (1966) theory. We note that two papers of Barklem et al. ([6]) and Allard et al. ([2]) obtain larger values of the hydrogen self-broadening cross-sections. An impact of using the self-broadening formalism of Barklem et al. ([6]) on effective temperature determinations for metal-poor stars is discussed by Mashonkina et al. ([34]). The surface gravities are based on the HIPPARCOS parallaxes. Iron abundances are obtained from Fe II lines, and the microturbulence velocities are estimated by requiring that the iron abundance derived from Fe II lines should not depend on equivalent width. The estimated uncertainties in the temperature, surface gravity, metal abundance, and microturbulence velocity are for most stars ±80 K, 0.10 dex, 0.05 dex, and 0.2 kms^{-1}, respectively.

3.3   Atomic line data

Table 1 lists the relevant line data with their final solar fit values (Shi et al. [44], hereafter paper I). Collisional broadening caused by the van der Waals interaction with hydrogen atoms is important only for strong Si lines. As already pointed out by Gehren et al. ([22], [23]), the resulting values of the van der Waals damping constants are almost always close to those calculated according to tables of Anstee & O'Mara's ([4], [5]) and Barklem et al.'s ([7]). In our analysis, the absolute value of the oscillator strengths is unimportant because the abundances are evaluated in a fully differential way with respect to the Sun.

Table 1: Atomic data of silicon lines*.

λ [Å]	Transition	log gf	log C_6
Si I 3905.53	$3p^1S_0 - 4s^1P_1^o$	-1.10	-30.917
Si I 4102.93	$3p^1S_0 - 4s^3P_1^o$	-2.99	-30.972
Si I 4947.61	$4s^1P_1^o - 6p^1S_0$	-2.25	-30.287
Si I 5645.61	$4s^3P_1^o - 5p^3P_2$	-2.03	-30.294
Si I 5665.55	$4s^3P_0^o - 5p^3P_1$	-1.99	-30.294
Si I 5684.48	$4s^3P_0^o - 5p^3P_1$	-1.58	-30.294
Si I 5690.43	$4s^3P_1^o - 5p^3P_1$	-1.74	-30.294
Si I 5701.11	$4s^3P_1^o - 5p^3P_0$	-1.96	-30.294
Si I 5772.15	$4s^1P_1^o - 5p^1S_0$	-1.62	-30.287
Si I 5793.07	$4s^3P_1^o - 5p^3D_2$	-1.86	-30.287
Si I 5948.54	$4s^1P_1^o - 5p^1D_2$	-1.09	-30.294
Si I 6125.02	$3p^3\ ^3D_1^o - 5f^3D_2$	-1.53	-29.869
Si I 6142.49	$3p^3\ ^3D_3^o - 5f^3D_3$	-1.48	-29.869
Si I 6145.05	$3p^3\ ^3D_2^o - 5f^3G_3$	-1.39	-29.869
Si I 6155.14	$3p^3\ ^3D_3^o - 5f^3G_4$	-0.78	-29.869
Si I 6237.32	$3p^3\ ^3D_1^o - 5f^3F_2$	-1.08	-29.869
Si I 6243.82	$3p^3\ ^3D_2^o - 5f^3F_3$	-1.29	-29.869
Si I 6244.47	$3p^3\ ^3D_2^o - 5f^1D_2$	-1.29	-29.869
Si I 6741.63	$4p^3D_2^o - 8s^3P_2$	-1.57	-29.853
Si I 6976.51	$4p^3D_1^o - 6d^3F_2$	-0.74	-29.895
Si I 7003.57	$4p^3D_2^o - 6d^3F_3$	-0.90	-29.434
Si I 7005.88	$4p^3D_3^o - 6d^3F_4$	-0.56	-29.090
Si I 7034.90	$3d^1D_2^o - 5f^3G_3$	-0.78	-29.027
Si I 7405.79	$3p^3\ ^3D_2^o - 4f^3F_2$	-0.62	-29.869
Si I 7415.36	$3p^3\ ^3D_2^o - 4f^3F_2$	-1.60	-29.869
Si I 7415.95	$3p^3\ ^3D_2^o - 4f^3F_3$	-0.65	-29.969
Si I 7680.26	$4p^1P_1^o - 5d^1D_2$	-0.56	-29.656
Si I 7800.00	$3d^3F_2^o - 6f^3F_2$	-0.68	-29.125
Si I 7849.97	$3d^3F_3^o - 6f^3F_2$	-0.59	-29.125
Si I 7918.38	$4p^3D_1^o - 5d^3F_2$	-0.52	-29.663
Si I 7932.34	$4p^3D_2^o - 5d^3F_3$	-0.31	-29.663
Si I 7944.00	$4p^3D_3^o - 5d^3F_4$	-0.20	-29.663
Si I 8728.01	$3d^3F_2^o - 5f^3F_3$	-0.38	-29.241
Si I 8742.45	$3d^1D_2^o - 5f^3F_3$	-0.36	-30.916
Si I 8752.01	$3d^1D_2^o - 4f^1F_3$	-0.19	-30.751
Si II 6347.10	$4s^2S_{1/2} - 4p^2P_{3/2}^o$	0.26	-30.200
Si II 6371.36	$4s^2S_{1/2} - 4p^2P_{1/2}^o$	-0.06	-30.200

*log gf values have been determined from NLTE solar spectrum fits, and damping constants log C_6 for Si I and Si II lines are computed according to the Anstee & O'Mara (1991, 1995) interpolation tables and Barklem et al.'s ([7]) table.

4 NLTE calculations
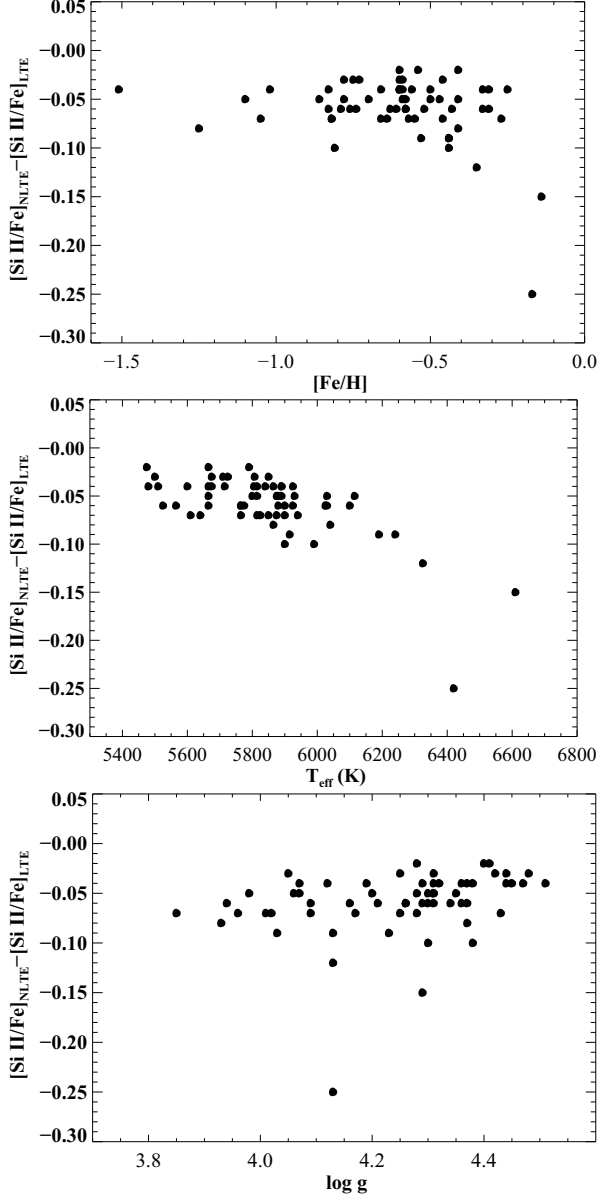
Figure 1: Difference of [Si II/Fe] abundance ratios calculated under the assumptions of NLTE and LTE as a function of metal abundance (a), temperature (b), and surface gravity (c).

4.1 Atomic model

The silicon model atom includes the most important levels of Si I and Si II and comprises 132 terms of Si I, 41 terms of Si II, and the Si III ground state. The atomic properties are documented in Shi et al. (Paper I and II).

All calculations are carried out with a revised version of

the DETAIL program (Butler & Giddings [13]) using accelerated lambda iteration (see Gehren et al. [22], [23] for details).

4.2 NLTE effects

The abundance analyses of both Si I and Si II lines clearly display the NLTE effects. We note that the NLTE effects differ from line to line, as we discussed in Paper II the strong Si I lines at 3905 and 4102 Å are quite strongly affected by NLTE effects for warm metal-poor stars, while the abundances measured for weak lines are the least affected by NLTE effects (< 0.02 dex), although the NLTE effects are slightly larger for the weak infrared lines (~ 0.05 dex).

Similar to the Ca II lines, the NLTE abundance corrections for the two Si II lines are negative (Mashonkina et al. [33]). We find that the NLTE correction is large for high temperature stars, and even larger than 0.2 dex for warm stars. For our program stars, the abundance differences between the LTE and NLTE analyses of the Si II lines are plotted in Fig. 1 as a function of metallicity ([Fe/H]), effective temperature, and surface gravity, respectively. There is a clear trend where the NLTE effects increase with increasing temperature.

5 Results
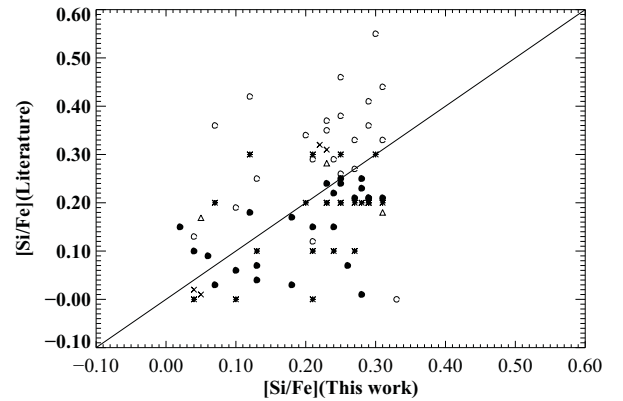
Figure 2: Comparison of derived [Si/Fe] (NLTE) for stars in common with other studies. Open triangles (Δ) are from Bensby et al. (2003,2005), crosses ($\times$) are from Decauwer et al. (2005), open circles ($\circ$) are from Fulbright (2000,2002), asterisks ($*$) are from Gratton et al. (2003), and filled circles ($\bullet$) are from Reddy et al. (2003,2006)

5.1 Stellar silicon abundances

We determinate the silicon abundances of our program stars using spectral synthesis. The synthetic spectra are convolved with macroturbulence, rotational, and instrumental broadening profiles, in order to match the observed spectral lines.

Our NLTE abundance results do not show a large abundance discrepancy between different lines; the final abundance scatter of single lines is between 0.01 and 0.1. The derived abundances are presented in Table 2, which is available in the electronic version of this paper.

5.2   Comparison with other work

Silicon abundances for metal-poor stars have been determined by several groups based on LTE analyses. By comparing the abundances of stars in common, we have verified that the different studies are consistent. In Fig.2, we compare the [Si/Fe] values (assuming NLTE) determined in this paper with those from the literature. Some systematic differences can be seen from this figure, which in the remaining part of this section, we briefly try to explain.

Using high resolution, high signal-to-noise ratio spectra of 168 F to K dwarf stars, Bensby et al. ([10], [11]) confirmed the overabundance ratio [Si/Fe] of thick-disc stars. Their results were determined using the weak Si I lines. Their gf values were adopted from the laboratory work of Garz ([21]) and its revision by Becker et al. ([9]), and are very similar to ours. We have four stars in common with this work, the mean difference between them and us is $\overline{\Delta[\text{Si/Fe}]} = 0.03 \pm 0.06$.

Decauwer et al. ([16]) analysed a sample of moderately metal-poor stars of which three were analysed by ourselves. They used weak Si I lines to determine their Si abundances, and the gf values adopted in their study are nearly the same as those used here. The difference is $\overline{\Delta[\text{Si/Fe}]} = 0.01 \pm 0.096$ between their and our measurements. In paper II, we proposed that the optical Si I lines are very weak in metal-poor stars, so the determination of the continuum is difficult. The large scatter is mostly due to the uncertainty in determining the continuum.

The analysis of Fulbright ([19], [20]) deals with 168 metal-poor stars of which 22 stars are in common with our sample. For the 22 stars in common with our list, we find that $\overline{\Delta[\text{Si/Fe}]} = 0.09 \pm 0.086$. They used weak Si I lines to determine the silicon abundances, and took the $\log gf$ values from the laboratory work of Garz ([21]), thus their gf values are about 0.1 dex lower then ours, and this difference in gf might explain the discrepancies.

Gratton et al. ([26]) determined the silicon abundances of 150 field subdwarfs and subgiants. They used the weak optical Si I lines, and adopted the gf values of Garz's ([21]). Our results mostly agree with theirs. For the 23 stars in common, the average difference is 0.003 ± 0.09.

Reddy et al. ([42], [41]) analysed a large sample of nearby thin- and thick-disc stars based on the optical Si I lines. The gf values adopted in this study are nearly the same as the values we adopted. The results of Reddy et al. are in agreement with ours. For the 24 common stars from Reddy et al., the average difference between their measurements and ours is -0.05 ± 0.059.

6   Discussion

6.1   Si I/Si II ionization equilibrium in metal-poor stars

Our discussion is based on the stars with Si abundances determined from both Si I and Si II lines in our present sample and the nine stars from paper II, and excellent agreement between the two ionization stages is achieved when NLTE effects are included. The average difference of $\overline{\Delta[\text{SiI/Fe}] - [\text{SiII/Fe}]}$ is -0.03 ± 0.019. The difference in the [Si/Fe] abundance ratios calculated under LTE and NLTE as a function of surface gravity for these stars is plotted in Fig. 3. The conclusion that the NLTE leads to consistent Si abundances derived from the two ionization stages is obviously supported by this figure.
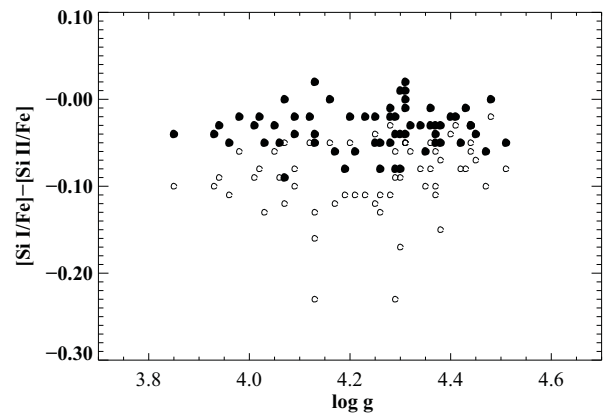
Figure 3: Difference of [Si/Fe] abundance ratios calculated under NLTE and LTE assumptions as a function of $log\ g$. Filled circles (●) represent data derived from a NLTE analysis, while open circles (○) are those for LTE analysis.

6.2   Silicon abundance and nucleosynthesis in the early Galaxy

The variation in [Si/Fe] as a function of [Fe/H] contains information about the chemical evolution of the Galaxy. Fig.4 displays the dependence of [Si/Fe] (calculated for NLTE) on the metal abundance for all stars considered in both this paper and paper II. The important features that can be seen from Fig.4 are that, although there is scatter, the bulk of the [Si/Fe] ratios are around +0.3 for our halo and thick disc program stars, while the [Si/Fe] ratios decrease with increasing [Fe/H] for thin disc stars. The exceptions are the five moderately metal-poor stars, namely, BD +20° 2594, CD −51° 4628, G 170-56, HD 122196, and HD 224930, which have relatively low [Si/Fe] values. We note that the first four stars also have lower values of magnesium. Such type stars were also found and discussed by Nissen & Schuster ([36], [37]) and Cohen et al. ([15], [14]). The star HD 224930 is in fact a spectroscopic binary, whose Ca II H+K lines show evidence

of core emission (see Gehren et al. [23]). We also found that one thick disc star HD 46341 has a slightly low Si abundance ([Si/Mg]=0.07). We note that its Mg abundance is higher than 0.25 ([Mg/Fe]=0.26), while the Ca abundance is also low ([Ca/Fe]=0.11). According to its rotational velocity (V $> -62\,km\,s^{-1}$) it is more likely to be part of the thin disc population (Ibukiyama & Arimoto [27]).

Several groups (e.g. Timmes et al. [47]; Samland [43]; Goswami & Prantzos [25]; Kobayashi et al. [29]) have modelled the Galactic chemical evolution of silicon. Goswami & Prantzos ([25]) and Kobayashi et al. ([29]) predicted that the [Si/Fe] ratios decrease from [Fe/H]~ -4 to [Fe/H] ~ 0, while Samland ([43]) presented a nearly flat [Si/Fe] ratio for metal-poor stars. However, Timmes et al. ([47]) showed that [Si/Fe] increases from [Fe/H] ~ -3 to ~ -2, while it decreases from [Fe/H] ~ -2 to ~ -0.8, with a nearly flat ratio (~ 0.2) for thin disc stars (see their Fig. 21). Our observational results for disc and halo stars are consistent with the theoretical predictions of Samland ([43]), the flat [Si/Fe] trend of the thick disc and halo stars not being predicted by the other three theoretical models.

Usually magnesium is used as the main tracer for assessing the metallicity dependence. It has been suggested that nearly all magnesium is produced in massive stars (Timmes et al. [47]), hence using magnesium instead of iron as the reference can help us to disregard type Ia SNe. The overall behaviour of the [Si/Mg] ratios versus [Fe/H] is shown in Fig.5, where NLTE magnesium abundances are taken from Gehren et al. ([23], [24]) and Mashonkina et al. ([34]). Although there is some scatter, our result shows that the [Si/Mg] ratio is around -0.1 for halo and thick disc stars, and the thin disc [Si/Mg] ratios smoothly merge with the thick disc ratios in the overlapping metallicity range.
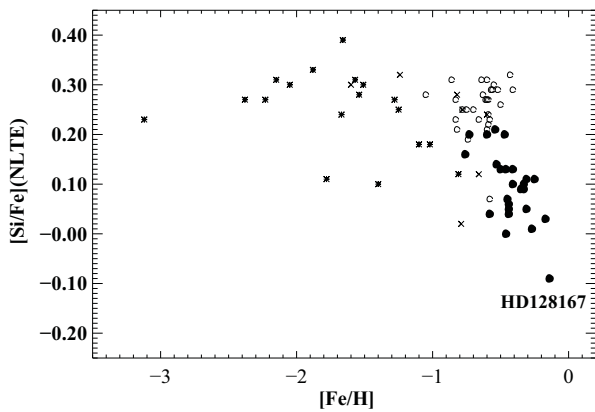
Figure 4: Abundance ratios [Si/Fe] as a function of [Fe/H]. Filled circles (•) represent thin disc stars, open circles (∘) thick disk stars, the asterisks (∗) halo stars, and cross(×) peculiar stars.

Nearly all oxygen is proposed to be produced in type II SNe (Timmers et al. [47]), and oxygen abundances ap-

pear to be overabundant for metal-poor stars (Nissen et al. [35], Ramírez et al. [40]). In contrast most of the silicon is assumed to be synthesized in moderate-mass type II SNe (Woosley & Weaver [50]), and type Ia SNe should also produce some silicon (Tsujimoto et al. [48]; Iwamoto et al. [28], Thielemann et al. [46], Maeda et al. [31]). The nearly constant [Si/Mg] ratio that has a small scatter for thick disc and halo stars suggests that the nucleosynthesis of silicon is closely coupled to that of the magnesium. The prediction, that type Ia SNe produce some amount of silicon, may not be supported by our result, that the thin disc [Si/Mg] ratios smoothly merge with the thick disc ratios in the overlapping metallicity range.
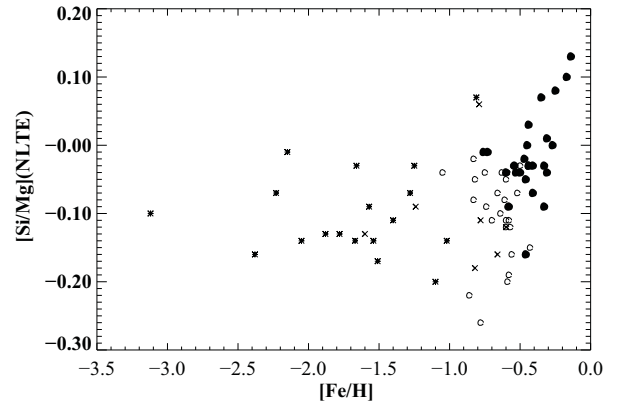
Figure 5: Abundance ratios [Si/Mg] for the NLTE analysis as a function of [Fe/H]. Symbols are the same as in Fig. 4.

7 Conclusions

We have determined silicon abundances for 67 metal-poor stars, spanning the range -1.9 < [Fe/H] <∼0.0. All abundances are derived from NLTE statistical equilibrium calculations. On the basis of our results, we come to the following conclusions:

1. There is a clear separation between [Si/Fe] for thin- and thick disc stars, the [Si/Fe] ratios are overabundant for thick disc stars. However, the number of thin/thick disc stars with overlapping metallicities needs to be increased to verify these trends. In addition, there is an indication that [Si/Fe] decreases with increasing metallicity for thin disc stars, while the [Si/Mg] ratios are around -0.1 for halo and thick disc stars.

2. The NLTE effects are different from line to line. The weak lines are quite insensitive to NLTE effects, while the infrared lines show small NLTE effects, although these effects are smaller than 0.05 dex. For the two Si II lines, NLTE leads to enhanced absorption in the line cores and negative abundance corrections over the

range of stellar parameters studied here, the effects of which depend on the temperature, hence tends to be large for warm stars.

3. Our results confirm that NLTE largely removes obvious discrepancies between Si I and Si II obtained under the LTE assumption.

4. Our results suggest that, in a similar way to magnesium, silicon is produced by massive type II SNe, while SN Ia should not contribute significantly to Si.

References

[1]. Ali, A. W., Griem, H. R., 1966, Phys. Rev., 144, 366

[2]. Allard, N. F., Kielkopf, J. F., Cayre R., van't Veer-Menneret, C. 2008, A&A, 480, 581

[3]. Anders, E., Grevesse, N. 1989, Geochim. Cosmochim. Acta, 53, 197

[4]. Anstee, S. D., O'Mara, B. J. 1991, MNRAS, 253, 549

[5]. Anstee, S. D., O'Mara, B. J. 1995, MNRAS, 276, 859

[6]. Barklem, P.S., Piskunov, N., O'Mara, B. J. 2000a, A&A, 355, L5

[7]. Barklem, P. S., Piskunov, N., O'Mara, B. J. 2000b, A&AS, 142, 467

[8]. Baumüller, D., Gehren, T. 1996, A&A, 307, 961

[9]. Becker, U., Zimmermann, P., Holweger, H. 1980, Geochim. Cosmochim. Acta 44, 2145

[10]. Bensby, T., Feltzing, S., Lundström, I. 2003, A&A, 410, 527

[11]. Bensby, T., Feltzing S., Lundström, I., Ilyin, I. 2005, A&A 433, 185

[12]. Bergemann, M.; Cescutti, G. 2010 A&A, 522, 9

[13]. Butler, K., Giddings, J. 1985, Newsletter on the analysis os astronomical spectra No. 9, University of London

[14]. Cohen, J. G., Christlieb, N., McWilliam, A., Shectman, S., Thompson, I. et al. 2008, ApJ, 672, 230

[15]. Cohen, J. G., McWilliam, A., Christlieb, N., Shectman, S., Thompson, I. et al. 2007, ApJ, 659, L161

[16]. Decauwer, H., Jehin, E., Parmentier, G., Magain P. 2005, A&A, 433, 285

[17]. Fuhrmann, K., Axer, M., Gehren, T. 1993, A&A, 271, 451

[18]. Fuhrmann, K., Pfeiffer, M., Frank, C. et al. 1997, A&A, 323, 909

[19]. Fulbright, J. P. 2000, AJ, 120, 1841

[20]. Fulbright, J. P. 2002, AJ, 123, 404

[21]. Garz T., 1973, A&A 26, 471

[22]. Gehren, T., Butler, K., Mashonkina, L. et al. 2001, A&A, 366, 981

[23]. Gehren, T., Liang, Y. C., Shi, J. R. et al. 2004, A&A, 413, 1045

[24]. Gehren, T., Shi, J. R., Zhang, H. W., Zhao, G., Korn, A. J. 2006, A&A, 451, 1065

[25]. Goswami, A., Prantzos, N. 2000, A&A, 359, 191

[26]. Gratton, R. G., Carretta, E., Claudi, R. et al. 2003, A&A, 404, 187

[27]. Ibukiyama, A., Arimoto, N. 2002, A&A, 394, 927

[28]. Iwamoto, K., Brachwitz, F., Nomoto, K. et al. 1999, ApJS, 125, 439

[29]. Kobayashi, C., Umeda H., Nomoto, K., Tominaga, N., Ohkubo, T., 2006, ApJ, 653, 1145

[30]. Korn, A., Shi, J. R., Gehren, T. 2003 A&A, 407, 691

[31]. Maeda K., Röpke F.K., Fink M., Hillebrandt W., Travaglio C., Thielemann F.-K. 2010, ApJ, 712, 624

[32]. Mashonkina, L., Gehren, T., Shi, J. R., Korn, A., Gruup, F. 2011, A&A, accepted

[33]. Mashonkina, L., Korn, A., Przybilla, N. 2007, A&A, 461, 261

[34]. Mashonkina, L., Zhao, G., Gehren, T., Aoki, W., Bergemann, M. et al. 2008, A&A, 478, 529

[35]. Nissen, P. E., Primas, F., Asplund, M., Lambert, D. L. 2002, A&A, 390, 235

[36]. Nissen, P. E., Schuster, W. J. 1997, A&A, 326, 751

[37]. Nissen, P. E., Schuster, W. J. 2010, A&A, 511, L10

[38]. Ohkubo, T., Umeda, H., Maeda, K., Nomoto, K., Suzuki, T. et al. 2006, ApJ, 645, 1352

[39]. Pfeiffer, M.J., Frank, C., Baumüller, D. et al. 1998, A&AS, 130, 381

[40]. Ramírez, I., Allende Prieto, C., Lambert, D.L. 2007, A&A, 465, 271

[41]. Reddy, B. E., Lambert, D. L., Allende Prieto, C. 2006, MNRAS, 367, 1329

[42]. Reddy, B. E., Tomkin, J., Lambert, D. L., Allende Prieto, C. 2003, MNRAS, 340, 304

[43]. Samland, M. 1998, ApJ, 496,155

[44]. Shi, J. R., Gehren, T., Butler, K., Mashonkina, L., Zhao, G. 2008, A&A, 486, 303 (Paper I)

[45]. Shi, J. R., Gehren, T., Mashonkina, L., Zhao, G. 2009, A&A 503, 533 (paper II)

[46]. Thielemann, K. K., Argast, D., Brachwitz, F. et al. 2002, ApSS, 281, 25

[47]. Timmes, F. X., Woosley, S. E., Weaver, T. A. 1995, ApJS, 98, 617

[48]. Tsujimoto, T., Nomoto, K., Yoshii, Y. et al. 1995, MNRAS, 277, 945

[49]. Umeda, H., Nomoto, K., Nakamura, T. 2000, in The first Stars, eds. A. Weiss, T. Abel & V. Hill, Heidelberg, Springer, p. 150

[50]. Woosley, S. E., Weaver, T. A., 1995, ApJS, 101, 181

[51]. Zhao, G., Butler, K., Gehren, T., 1998, A&A, 333, 219

[52]. Zhao, G., Gehren, T., 2000, A&A, 362, 1077

Table 2: Stellar silicon LTE and NLTE (for each star, the first and the second row, respectively) abundances given relative to the iron LTE abundances derived from the Fe II lines. Our NLTE calculations for Fe I/II based on the advanced atomic model (Mashonkina et al. [32]) support the earlier conclusion of Korn et al. ([30]) that the NLTE effects for the Fe II lines are negligible.

Name	T_{eff}	log g	[Fe/H]	ξ	[Si I/Fe](LTE)	[Si I/Fe](NLTE)	[Si II/Fe](LTE)	[Si II/Fe](NLTE)	
HD 17948	6325	4.13	-0.35	1.9	0.09±0.026	0.09 ± 0.024	0.25± 0.005	0.13 ± 0.015	D
HD 22309	5900	4.29	-0.31	1.3	0.06±0.021	0.05 ± 0.019	0.15± 0.000	0.09 ± 0.005	D
HD 22879	5775	4.26	-0.83	1.1	0.24±0.035	0.23 ± 0.032	0.37± 0.010	0.31 ± 0.010	T
HD 30649	5765	4.26	-0.58	1.1	0.23±0.045	0.23 ± 0.045	0.34± 0.005	0.28 ± 0.005	T
HD 241253	5850	4.25	-1.05	1.2	0.28±0.037	0.28 ± 0.036	0.40± 0.000	0.33 ± 0.000	T
HD 243357	5675	4.38	-0.59	1.1	0.27±0.034	0.27 ± 0.033	0.34± 0.005	0.30 ± 0.000	T
HD 36283	5475	4.28	-0.41	0.8	0.30±0.027	0.29 ± 0.030	0.33± 0.015	0.31 ± 0.015	T
G 99-21	5525	4.30	-0.63	1.0	0.29±0.030	0.28 ± 0.026	0.38± 0.000	0.32 ± 0.000	T
HD 250792	5600	4.32	-1.02	1.1	0.19±0.039	0.18 ± 0.039	0.25± 0.000	0.21 ± 0.000	H
HD 46341	5880	4.36	-0.58	1.8	0.08±0.020	0.07 ± 0.023	0.16± 0.005	0.10 ± 0.000	T
HD 56513	5630	4.53	-0.45	1.2	0.07±0.018	0.07 ± 0.019			D
HD 58551	6190	4.23	-0.53	1.8	0.14±0.026	0.14 ± 0.028	0.25± 0.000	0.16 ± 0.005	D
HD 59374	5840	4.37	-0.83	1.4	0.28±0.031	0.27 ± 0.032	0.34± 0.000	0.30 ± 0.000	T
HD 59984	5925	3.94	-0.74	1.2	0.19±0.027	0.19 ± 0.025	0.28± 0.005	0.22 ± 0.005	T
HD 60319	5875	4.17	-0.82	1.4	0.22±0.030	0.21 ± 0.027	0.34± 0.025	0.27 ± 0.015	T
HD 233511	6015	4.29	-1.57	1.4	0.27±0.050	0.31 ± 0.003			H
G 235-45	5500	4.25	-0.59	1.1	0.25±0.039	0.24 ± 0.032	0.29± 0.015	0.26 ± 0.015	T
HD 88446	5915	4.03	-0.44	1.6	0.07±0.020	0.06 ± 0.014	0.20± 0.020	0.11 ± 0.000	D
HD 88725	5665	4.35	-0.70	1.2	0.26±0.037	0.25 ± 0.032	0.36± 0.010	0.31 ± 0.010	T
HD 91784	5890	4.47	-0.33	1.3	0.09±0.020	0.09 ± 0.017	0.19± 0.005	0.15 ± 0.000	D
G 119-32	5715	4.39	-1.88	1.2	0.27±0.000	0.33 ± 0.000			H
HD 94028	5925	4.19	-1.51	1.5	0.31±0.059	0.30 ± 0.057	0.42± 0.000	0.38 ± 0.000	H
HD 96094	5900	4.01	-0.46	1.7	0.14±0.028	0.13 ± 0.020	0.23± 0.005	0.16 ± 0.000	D
HD 97855A	6240	4.13	-0.44	1.8	0.06±0.025	0.05 ± 0.017	0.19± 0.005	0.10 ± 0.000	D
BD +20 2594	5900	4.30	-0.81	1.4	0.13±0.054	0.12 ± 0.048	0.30± 0.000	0.20 ± 0.000	H
HD 101177	5890	4.30	-0.47	1.8	0.20±0.044	0.20 ± 0.043	0.24± 0.010	0.19 ± 0.005	D
HD 104056	5875	4.31	-0.41	1.3	0.13±0.028	0.13 ± 0.023	0.18± 0.000	0.13 ± 0.005	D
HD 107582	5565	4.34	-0.61	1.0	0.28±0.035	0.27 ± 0.029	0.36± 0.005	0.30 ± 0.000	T
HD 108076	5725	4.44	-0.73	1.2	0.21±0.020	0.20 ± 0.019	0.26± 0.005	0.23 ± 0.005	D
HD 114606	5610	4.28	-0.57	1.2	0.30±0.027	0.29 ± 0.025	0.41± 0.010	0.34 ± 0.010	T
HD 118659	5510	4.36	-0.60	1.0	0.27±0.029	0.27 ± 0.025	0.32± 0.010	0.28 ± 0.000	T
HD 119288	6420	4.13	-0.17	1.9	0.03±0.019	0.03 ± 0.017	0.26± 0.010	0.01 ± 0.005	D
HD 123710	5790	4.41	-0.54	1.4	0.22±0.025	0.21 ± 0.024	0.25± 0.000	0.23 ± 0.005	D
HD 126512	5825	4.02	-0.64	1.6	0.32±0.034	0.31 ± 0.031	0.40± 0.000	0.33 ± 0.000	T
HD 128167	6610	4.29	-0.14	1.3	-0.09±0.021	-0.09 ± 0.024	0.14± 0.015	-0.01 ± 0.010	D
HD 134169	5930	3.98	-0.86	1.8	0.32±0.037	0.31 ± 0.031	0.38± 0.005	0.33 ± 0.010	T
HD 142267	5807	4.42	-0.46	1.0	0.00±0.044	-0.00 ± 0.049	0.08± 0.000	0.05 ± 0.000	D
HD 144061	5815	4.44	-0.31	1.2	0.12±0.035	0.11 ± 0.041	0.18± 0.025	0.14 ± 0.020	D
HD 148816	5880	4.07	-0.78	1.2	0.25±0.042	0.25 ± 0.043	0.30± 0.000	0.25 ± 0.005	?
HD 149996	5665	4.09	-0.52	1.2	0.29±0.029	0.29 ± 0.025	0.37± 0.000	0.31 ± 0.005	T
BD +68° 901	5715	4.51	-0.25	1.4	0.12±0.041	0.11 ± 0.048	0.20± 0.005	0.16 ± 0.005	D

Table 2 (continued)

Name	T_{eff}	log g	[Fe/H]	ξ	[Si I/Fe](LTE)	[Si I/Fe](NLTE)	[Si II/Fe](LTE)	[Si II/Fe](NLTE)	
HD 157089	5800	4.06	-0.59	1.2	0.23±0.040	0.22 ± 0.046	0.32± 0.005	0.27 ± 0.010	T
HD 157466	5990	4.38	-0.44	1.1	0.04±0.036	0.04 ± 0.040	0.19± 0.005	0.09 ± 0.005	D
HD 158226	5805	4.12	-0.56	1.1	0.30±0.027	0.29 ± 0.032	0.35± 0.000	0.31 ± 0.000	T
G 170-56	6030	4.31	-0.79	1.3	0.04±0.031	0.02 ± 0.031	0.09± 0.015	0.03 ± 0.010	?
HD 160933	5765	3.85	-0.27	1.2	0.02±0.030	0.01 ± 0.029	0.12± 0.035	0.05 ± 0.020	D
HD 160693	5850	4.31	-0.60	1.2	0.26±0.031	0.24 ± 0.039	0.31± 0.010	0.28 ± 0.010	?
HD 170357	5665	4.07	-0.50	1.2	0.27±0.040	0.26 ± 0.037	0.39± 0.025	0.35 ± 0.015	T
HD 171620	6115	4.20	-0.50	1.4	0.15±0.033	0.13 ± 0.027	0.20± 0.005	0.15 ± 0.005	D
G 142-2	5675	4.48	-0.75	1.1	0.26±0.036	0.25 ± 0.039	0.28± 0.005	0.25 ± 0.005	T
HD 182807	6100	4.21	-0.33	1.4	0.11±0.025	0.10 ± 0.028	0.22± 0.030	0.16 ± 0.020	D
HD 184448	5765	4.16	-0.43	1.2	0.33±0.038	0.32 ± 0.044	0.38± 0.035	0.32 ± 0.015	T
HD 186379	5865	3.93	-0.41	1.2	0.12±0.027	0.10 ± 0.033	0.22± 0.020	0.14 ± 0.015	D
HD 198300	5890	4.31	-0.60	1.2	0.22±0.028	0.21 ± 0.032	0.23± 0.000	0.19 ± 0.010	T
HD 200580	5940	3.96	-0.82	1.4	0.29±0.032	0.28 ± 0.031	0.40± 0.015	0.33 ± 0.015	?
G 188-22	6040	4.37	-1.25	1.5	0.27±0.045	0.25 ± 0.046	0.38± 0.005	0.30 ± 0.000	H
HD 201889	5710	4.05	-0.78	1.1	0.25±0.043	0.25 ± 0.042	0.31± 0.005	0.28 ± 0.000	T
HD 204155	5815	4.09	-0.66	1.2	0.24±0.030	0.23 ± 0.027	0.34± 0.000	0.27 ± 0.010	T
HD 208906	6025	4.37	-0.76	1.4	0.16±0.031	0.16 ± 0.034	0.26± 0.005	0.20 ± 0.000	D
G 242-4	5815	4.31	-1.10	1.2	0.18±0.032	0.18 ± 0.033	0.22± 0.025	0.17 ± 0.015	H
HD 215257	6030	4.28	-0.58	1.4	0.05±0.021	0.04 ± 0.022	0.10± 0.000	0.05 ± 0.005	D
HD 218209	5665	4.40	-0.60	1.1	0.31±0.037	0.31 ± 0.039	0.35± 0.015	0.33 ± 0.010	T
HD 221876	5865	4.29	-0.60	1.2	0.20±0.023	0.20 ± 0.026	0.26± 0.005	0.22 ± 0.000	D
HD 224930	5480	4.45	-0.66	0.9	0.13±0.029	0.12 ± 0.029	0.20± 0.000	0.16 ± 0.005	?
G 69-8	5640	4.43	-0.55	1.1	0.30±0.035	0.30 ± 0.036	0.38± 0.005	0.31 ± 0.005	T

New evaluation of the ^{13}C(α,n)^{16}O reaction rate and its influence on s-process nucleosynthesis in AGB stars

B. Guo(郭冰)[1], Z. H. LI(李志宏)[1], Y. J. LI(李云居)[1], J. Su(苏俊)[1], S. Q. Yan(颜胜权)[1], X. X. Bai(白希祥)[1],

Y. S. Chen(陈永寿)[1], Q. W. Fan(樊启文)[1], S. J. Jin(金孙均)[1], E. T. Li(李二涛)[1], Z. C. Li(李志常)[1],

G. Lian(连钢)[1], J. C. Liu(刘建成)[1], X. Liu(刘鑫)[1], N. C. Shu(舒能川)[1], B. X. Wang(王宝祥)[1],

Y. B. Wang(王友宝)[1], S. Zeng(曾晟)[1], W. P. Liu(柳卫平)[1], D. Y. Pang(庞丹阳)[2],

M. Lugaro[3], J. Buntain[3], A. I. Karakas[4] & J. R. Shi(施建荣)[5]

[1]*China Institute of Atomic Energy, P.O. Box 275(10), Beijing 102413, China*
[2]*School of Physics and State Key Laboratory of Nuclear Physics and Technology, Peking University, Beijing 100871, China*
[3]*Centre for Stellar and Planetary Astrophysics, Monash University, Clayton 3800, Victoria, Australia*
[4]*Research School of Astronomy & Astrophysics, Mount Stromlo Observatory, Weston Creek ACT 2611, Australia*
[5]*National Astronomical Observatories, Chinese Academy of Science, Beijing 100012, China*

(To be submitted)

We present a reevaluation of astrophysical S-factor and reaction rate of ^{13}C(α,n)^{16}O based on the determination of the 6.356 MeV $1/2^+$ subthreshold resonance from α partial width for the $1/2^+$ state of ^{17}O by measuring the ^{13}C(^{11}B,^{7}Li)^{17}O angular distribution. Our result supports the conclusion that the $1/2^+$ subthreshold resonance dominates the ^{13}C(α,n)^{16}O reaction within Gamow window. The present rate is used as input for the simulation of asymptotic giant branch (AGB) stars by considering four models, to study its influence on the abundance of selected s-process elements and isotopic ratios through the comparison with those using the other available rates. The significant differences of up to 60%, which are produced in s-process abundances and ratios, were found by varying the ^{13}C burning rate.

Keywords: nuclear reactions, nucleosynthesis, abundances — stars: AGB and post-AGB

PACS: 25.70.Hi, 23.20.En, 21.10.Jx,25.40.Lw

1 Introduction

Approximately half of the elements heavier than iron in the universe are produced via a series of *slow* neutron capture reactions and competing β decay (so-called s-process). During the s-process, the neutron number density is relatively low (of the order of 10^7 n cm^{-3}) so that when the flux reaches an unstable nucleus, it typically decays rather than capture another neutron [4, 40]. Therefore, the s-process proceeds via the isotopes around the valley of β stability. The astrophysical site of s-process is the "He intershell" of asymptotic giant branch (AGB) stars with initial masses lower than roughly $9M_\odot$ in the final phases of their evolution, when both H and He have been exhausted in the core leaving C and O in electron degenerate conditions. Production of nuclear energy occurs in the H and He shells, which are located between the core and the extended convective envelope and are separated by a thin He intershell layer. AGB stars experience thermal pulses (TPs) when the usually dormant He-burning shell is suddenly activated. A large amount of energy is released, which drives convection in the He intershell. The star expands and cools. As a consequence, the H-burning shell is disactivated during TPs. While He burning turns from the convective to the radiative regime, and eventually switches off, the convective envelope can penetrate the underlying He intershell and carry to the surface the products of He burning, in particular carbon, fluorine, and the elements heavier than iron made by s-process. This mixing process is known as the "third dredge-up" (TDU). After the TDU is ended, the star contracts and heats up again and H burning resumes until another TP occurs and the cycle is repeated. This sequence of events can occur from a few times to hundreds of times, depending on the stellar mass and the choice of mass loss. In fact, AGB stars suffer from very strong stellar winds, which erode the envelope roughly within a million years and shred the newly synthesized material mixed to the surface by the TDU into the intershellar medium. Eventually, the C-O degenerate core is left as a cooling white dwarf [22].

According to the current standard model [17, 5, 18, 37, 11], some protons must diffuse from the convective envelope into the He intershell at the end of each TDU in order to produce enough ^{13}C to account for the observed abundances of

the s-process elements at the surface of AGB stars [6]. A thin layer is then produced, known as the ^{13}C "pocket", which is rich in ^{13}C made via ^{12}C(p,γ)^{13}N($\beta^+\nu$)^{13}C in its lower layers, where the number of proton diffused is larger. When in this region the temperature reaches about 8×10^7 K, the ^{13}C(α,n)^{16}O reaction is activated, and plays the major role as the neutron source in AGB stars [24, 16, 27].

To date, considerable effort has been devoted to the direct measurement of the ^{13}C(α,n)^{16}O cross sections [44, 12, 3, 31, 15, 7, 20, 21]. These measurements have been performed down to 270 keV, whereas the Gamow window is 190 ± 40 keV corresponding to the temperature of 10^8 K in AGB stars. Since this energy is far below the Coulomb barrier, the reaction cross section is so extremely small that its direct measurement is sensitively limited by background signals and thus very difficult to perform [10]. Consequently, the measured cross sections presently have to be extrapolated below 270 keV. This extrapolation was suggested to be significantly affected by the $1/2^+$ subthreshold resonance in ^{17}O ($E_x =$ 6.356 MeV, just 3 keV below the α decay threshold) through a microscopic cluster model analysis of the ^{13}C(α,n)^{16}O and ^{13}C(α,α) reactions [14]. The contribution from this resonance strongly depends on the α partial width of this state in ^{17}O, which can be derived from its α spectroscopic factor (S_α) or the asymptotic normalization coefficient (ANC).

The α spectroscopic factor can be determined from the angular distribution of the direct α transfer reaction based on distorted wave Born approximation (DWBA) analysis. Although three indirect measurements [32, 26, 42] have been performed to study the S_α or ANC, there still exists a significant discrepancy up to a factor of ~30. A very small spectroscopic factor ($S_\alpha \sim 0.011$) for the $1/2^+$ state was found by the measurement of the ^{13}C(^{6}Li,d)^{17}O angular distribution with an incident energy of 60 MeV [32]. This result showed that the contribution from the $1/2^+$ subthreshold resonance was negligible. However, a reanalysis of the same experimental data deduced a large spectroscopic factor ($S_\alpha \sim 0.4$) [30]. Recently, the ^{6}Li(^{13}C,d)^{17}O angular distribution has been measured at sub-Coulomb energies and the square of ANC was derived to be 0.89 ± 0.23 fm^{-1} [26], which approximately corresponds to S_α of 0.06. Most recently, the angular distribution of ^{13}C(^{7}Li,t)^{17}O has been measured with two incident energies (28 and 34 MeV), and S_α was found to be 0.29 [42]. One can see that three previous results disagree with each other by a factor of 5-30. Therefore, it seems that a new measurement of S_α via a different transfer reaction is desirable as an independent examination to the existing discrepancies. In addition, the effect of available ^{13}C(α,n)^{16}O rates on s-process nucleosynthesis in AGB stars has not been explored so far. Thus, a detailed study of their influence is also highly needed.

In this paper we aim to determine the $1/2^+$ subthreshold resonance contribution in the ^{13}C(α,n)^{16}O reaction through the measurement of the α transfer reaction ^{13}C(^{11}B,^{7}Li)^{17}O, and then to evaluate the ^{13}C(α,n)^{16}O reaction rate. This rate

is used as input for the simulation of asymptotic giant branch (AGB) stars by considering four models, to study its influence on the abundance of selected s-process elements and isotopic ratios through the comparison with those using the other available rates.

2 Experiment and data analysis

The measurement was performed at the HI-13 tandem accelerator of CIAE in Beijing. The ^{11}B beam with an energy of 50 MeV was delivered and utilized to measure the angular distribution of ^{13}C(^{11}B,^{7}Li)^{17}O* (6.356 MeV) and the elastic scattering of its entrance channel (^{11}B+^{13}C). A self-supporting ^{13}C target with a thickness of 77(6) μg/cm^2 and an initial purity of 87% was used in the present experiment. In addition, the 26 MeV ^{7}Li beam was delivered for the measurement of the exit channel (^{7}Li+^{17}O) elastic scattering. The natural silicon monoxide of 86(7) μg/cm^2 was prepared onto a 40(3) μg/cm^2 carbon foil, serving as the oxygen target. In addition, a self-supporting ^{12}C target of 79(6) μg/cm^2 was used for the calibration of the focal plane and background subtraction in the whole experiment.

In order to monitor the possible buildup of ^{12}C, the ^{11}B elastic scattering on ^{13}C target was measured respectively at the start and the end of the experiment. It was shown that the ^{12}C buildup was negligibly small compared with the initial impurity in ^{13}C target, which could be owing to the rather low gas pressure ($\leqslant 10^{-6}$ mb) in the reaction chamber. To determine the absolute amount of ^{12}C in ^{13}C target, we measured the angular distribution of the ^{11}B+^{12}C elastic scattering with both natural ^{12}C target and enriched ^{13}C target. Consequently, the absolute amount of ^{12}C and ^{13}C in the ^{13}C target were found to be 10 and 67 μg/cm^2, respectively.

The beam current was measured by a Faraday cup covering an angular range of $\pm 6°$. The reaction products were focused and separated by Q3D magnetic spectrograph, and then recorded by a two-dimensional position sensitive silicon detector (PSSD, 50×50 mm) fixed at the focal plane of spectrograph. The two-dimensional position information from PSSD enabled the products emitted into the acceptable solid angle to be completely recorded, and the energy information was used to remove the impurities with the same magnetic rigidity.

Due to the presence of ^{12}C in the ^{13}C target, the ^{7}Li events from ^{13}C(^{11}B,^{7}Li)^{17}O* (6.356 MeV) were mixed with those from the ^{12}C(^{11}B,^{7}Li)^{16}O* (6.917 MeV) reaction. To evaluate this background, the (^{11}B,^{7}Li) reactions were measured for both ^{13}C and ^{12}C targets at each angle with the same experimental setup. After the background subtraction and beam normalization, the angular distributions of the elastic scattering and the transfer reaction are obtained, as presented in Figs. 1 and 2.
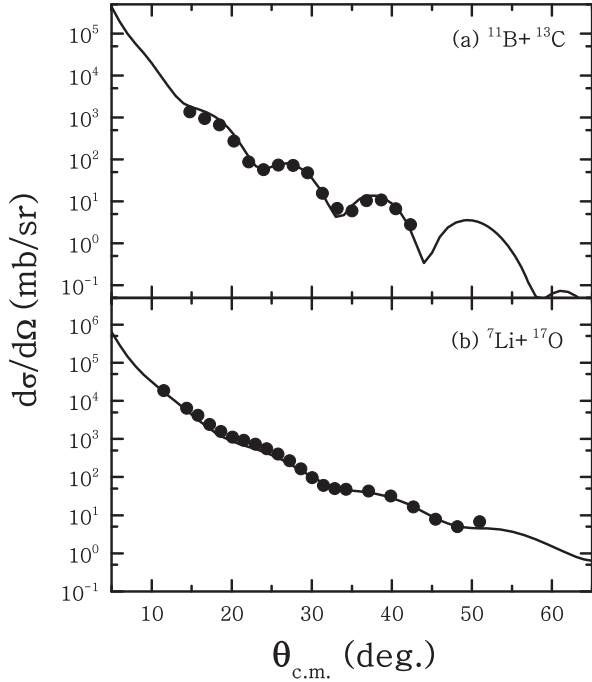
Figure 1: Angular distributions of the ^{11}B+^{13}C and the ^{7}Li+^{17}O elastic scattering. The solid lines stand for the calculations with the fitted OMP parameters.

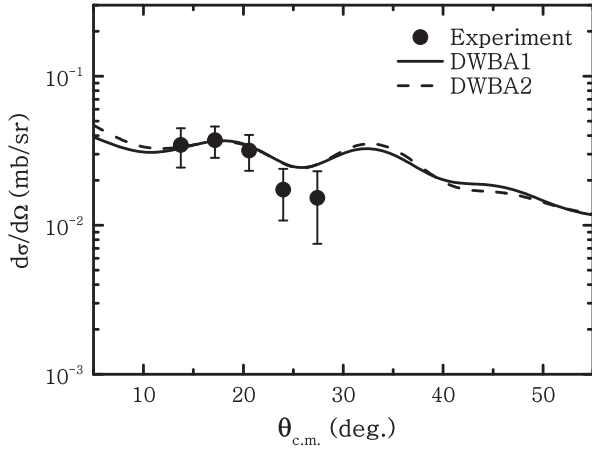Figure 2: Angular distribution of ^{13}C(^{11}B,^{7}Li)^{17}O* (6.356 MeV). The lines stand for the DWBA calculations with the fitted OMP parameters. DWBA1 and DWBA2 respectively represent the calculations using the spectroscopic amplitudes of ^{11}B from [33] and [43].

The finite-range distorted wave Born approximation (DWBA) code FRESCO [45] was used to analyze the experimental angular distribution. The optical model potential (OMP) parameters for entrance and exit channels were obtained by fitting the present ^{11}B+^{13}C and ^{7}Li+^{16}O angular distributions. The theoretical angular distributions of the elastic scattering with the fitted parameters are shown in Fig.

1, together with the experimental data. In general, the remnant term may be neglected for single-nucleon transfer reactions, but it was found that the remnant term has important effect on α transfer cross sections for the (^{6}Li,*d*) reaction [30]. Thus, two sets of parameters for the core-core (^{7}Li+^{13}C) potential [9], where they gave the similar elastic scattering of ^{7}Li from ^{13}C at 34 MeV, were taken to study the remnant term in the (^{11}B,^{7}Li) reaction. All the parameters used in DWBA calculations are listed in Table 1.

Table 1: Optical potential parameters used in DWBA calculation. E_{in} denotes the incident energy with the unit of MeV for the relevant channels, where V and W are in MeV, r and a in fm.

Channel	E_{in}	V	r_v	a_v	W	r_w	a_w
^{11}B+^{13}C	50.0	182.64	0.788	0.740	8.193	1.250	0.740
^{7}Li+^{17}O	26.0	114.20	0.737	0.719	34.602	0.997	0.764
^{7}Li+^{13}C	31.8	159.00	0.630	0.810	8.160	1.330	0.780
		156.40	0.666	0.763	9.100	1.196	0.950

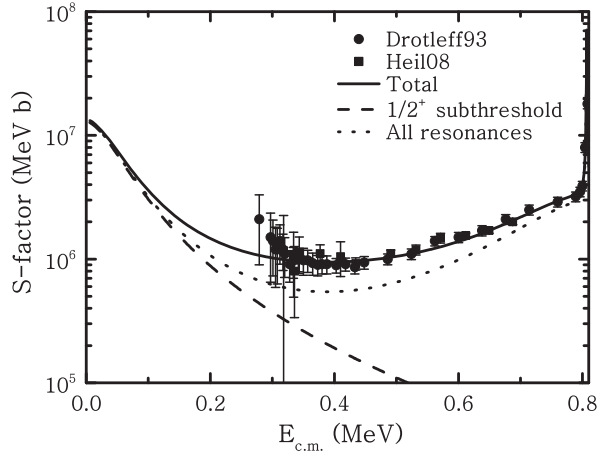Figure 3: Astrophysical S-factors for the ^{13}C(α,n)^{16}O reaction. Dots and squares respectively represent the data from [15] and [21]. The contribution from the 1/2$^+$ subthreshold resonance is displayed as the dashed line, while the solid curve presents total S-factors (see text for detail).

In order to study S_α of the 6.356 MeV 1/2$^+$ state in ^{17}O, the spectroscopic amplitudes of the ^{11}B ground state were required. There are two components in the single-particle wave function which describes the relative motion between ^{4}He and ^{7}Li in the ^{11}B ground state with quantum numbers (NL_j) of 3S_0 and 2D_2, where N is the number of radial nodes that include the origin but not the infinity, L and j are respectively the orbital and total angular momenta. The spectroscopic amplitudes of these two states (3S_0 and 2D_2) were derived to be -0.509 and 0.629 for the 3S_0 and 2D_2 states based on a shell-model calculation [33], while they were also extracted to be -0.638 and -0.422 based on the translationally invariant shell model and reproduced the experimental angular distribution of the ^{7}Li+^{11}B elastic scattering [43]. In the present analysis, the spectroscopic amplitudes given by [33]

and [43] were both used and the difference between them was included into total uncertainty.

The ^{4}He-cluster single-particle wave functions were calculated with conventional Woods-Saxon potentials with the depths adjusted to reproduce the binding energies of ^{4}He-cluster in the ^{11}B ground state (E_b = 8.665 MeV) and the $1/2^+$ state in ^{17}O (E_b = 0.003 MeV). The geometry parameters (radius r_0 and diffuseness a) of the Woods-Saxon potential for ^{4}He in ^{11}B were adjusted to give the root-mean-square (RMS) radius (r) of the ^{4}He-cluster wave function. The RMS radius of 3.204 fm was obtained by realizing the relation between the mean square radii of ^{4}He ($\langle r_{He}^2 \rangle$), ^{7}Li ($\langle r_{Li}^2 \rangle$) and ^{11}B ($\langle r_B^2 \rangle$),

$$\langle r_B^2 \rangle = \frac{m_{He}}{m_B}\langle r_{He}^2 \rangle + \frac{m_{Li}}{m_B}\langle r_{Li}^2 \rangle + \frac{m_{He}m_{Li}}{m_B^2}\langle r^2 \rangle. \quad (1)$$

The RMS radii of ^{4}He, ^{7}Li and ^{11}B were derived to be 1.47, 2.384 and 2.605 fm by [36] and used in the present calculation. We also investigated the dependence of our calculations on the geometry parameters of the Woods-Saxon potential for ^{4}He in ^{11}B. With the diffusenesses of 0.65-0.75 fm, the radius was adjusted to reproduce the RMS radius (3.204 fm). Their impact on the spectroscopic factor of ^{17}O was then found to be less than 2%. For the 6.356 MeV $1/2^+$ state in ^{17}O, the RMS radius has remained unknown so far. Therefore, the geometry parameters of the Woods-Saxon potential for ^{4}He in this state of ^{17}O can not be constrained by using Eq. 1. The effect of the geometry parameters for ^{17}O was scrutinized previously [42], where the parameters (r_0=0.914 fm, a=0.76 fm) provided the best fit for the angular distributions of ^{13}C(^{7}Li,t)^{17}O leading to the four states in ^{17}O at two incident energies. In our calculation, these geometry parameters were utilized to derive the spectroscopic factor and ANC for the $1/2^+$ state in ^{17}O. In addition, the quantum numbers (NL_j) for ^{4}He-cluster in the $1/2^+$ state of ^{17}O were fixed to be $4P_1$ by the oscillatory energy conservation relation $2(N-1) + L = \sum_{i=1}^{4} 2(n_i - 1) + l_i$, where ($n_i, l_i$) are the corresponding single-nucleon shell quantum numbers.

The S_α for the 6.356 MeV $1/2^+$ state in ^{17}O was derived to be 0.40 ± 0.12 by the normalization of DWBA calculations to the first three data on the ^{13}C(^{11}B,^{7}Li)^{17}O* (6.356 MeV) angular distribution. The uncertainty results from the statistics (27%), the target thickness (8%), the uncertainty of the spectroscopic amplitudes (9%) and the geometry parameters (2%) for the ^{11}B ground state. It should be noted that the effect on S_α of the remnant term for the ^{13}C(^{11}B,^{7}Li)^{17}O reaction is negligible, contrary to the (^{6}Li,d) system. The normalized DWBA angular distributions are displayed in Fig. 2, together with the experimental data. The shape of the experimental angular distribution is reasonably well reproduced by the DWBA calculation. The present S_α is in agreement with the one (0.29 ± 0.11) given by [42] but about 40 times larger than the one (0.011) by [32]. The Coulomb modified ANC ($\tilde{C}^2$) was then extracted to be 4.9 ± 1.5 fm^{-1} by the relation, $\tilde{C}^2 = S_\alpha R^2 \phi(R)^2 / \tilde{W}(R)^2$. Here, $\phi(R)$ is the radial

single-particle wave function for ^{4}He-cluster in the $1/2^+$ state of ^{17}O, while $\tilde{W}(R) = W(R)\Gamma(L+1+\eta)$ is the Coulomb modified Whittaker function where $\Gamma(L+1+\eta)$ is gamma function and η is Coulomb parameter. The present ANC is 5.5 times larger than that (0.89 ± 0.23 fm^{-1}) given by [26].
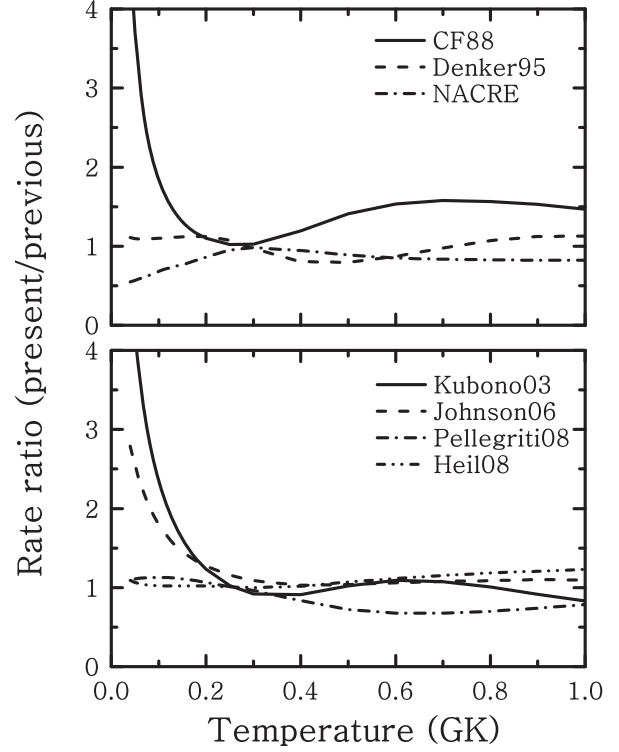

Figure 4: The ratios of the present rates to the previous compilations (top panel) [8, 13, 1] and the other available rates (bottom panel) [32, 26, 42, 21].

3 The ^{13}C(α,n)^{16}O reaction rate

The astrophysical S-factors of the ^{13}C(α,n)^{16}O reaction via the resonances can be calculated with the Breit-Wigner single-level formula,

$$S(E) = \pi \frac{(\hbar c)^2}{2\mu c^2} \frac{(2J_R + 1)}{(2J_p + 1)(2J_t + 1)}$$
$$\frac{\Gamma_\alpha(E)\Gamma_n(E + Q)}{(E - E_R)^2 + (\Gamma_{tot}/2)^2} \exp(\frac{E_G}{E})^{1/2}, \quad (2)$$

where μ is the reduced mass of the α+^{13}C system; E_R represents the resonance energy; J_R, J_p and J_t are the spins of the $1/2^+$ subthreshold state in ^{17}O, α and ^{13}C, respectively; Γ_α, Γ_n and Γ_{tot} denote the α-, neutron- and total widths; Q is the reaction Q value of ^{13}C(α,n)^{16}O; $E_G = 0.978Z_1^2Z_2^2\mu$ MeV is the Gamow energy. For the resonances above the α threshold, the energy dependence of these widths was given by [25]

$$\Gamma_\alpha(E) = \Gamma_\alpha(E_R)\frac{P_{l_i}(E)}{P_{l_i}(E_R)}, \quad (3)$$

and

$$\Gamma_n(E + Q) = \Gamma_n(E_R)(\frac{E + Q}{E_R + Q})^{l_f + 1/2}, \quad (4)$$

where $\Gamma_\alpha(E_R)$ and $\Gamma_n(E_R)$ stand for the experimental partial α- and neutron-widths, $P_{l_i}(E)$ is the α penetrability, l_i and l_f are respectively the orbital angular momenta for α and neutron in the $1/2^+$ state of ^{17}O. For the subthreshold resonance, the energy dependence of the neutron-width can be also obtained by Eq. 4, while the dependence of the α-width was expressed as

$$\Gamma_\alpha(E) = 2\gamma_\alpha^2 P_{l_i}(E). \quad (5)$$

Here the reduced α-width γ_α^2 can be given by

$$\gamma_\alpha^2 = \frac{\hbar^2 R}{2\mu} S_\alpha \phi(R)^2. \quad (6)$$

Based on the S_α of 0.40 ± 0.12 in this work, the reduced α-width γ_α^2 was extracted to be 14.8 ± 4.4 keV at $R = 7.5$ fm. This large radius was chosen to reach the Coulomb asymptotic behavior of $\phi(R)$, as suggested by [42].

The astrophysical S-factors from the contribution of the $1/2^+$ subthreshold resonance were then obtained by using the present γ_α^2, as indicated with the dashed line in Fig. 3. In addition, we evaluated total S-factors of ^{13}C(α,n)^{16}O by using the present γ_α^2 and the properties of the resonances up to 7.558 MeV from the compilation [46]. The contribution of all these resonances to astrophysical S-factor is shown as the dotted line in Fig. 3. One can see that this curve does not fully agree with the data from the direct measurements [15, 21]. Two approaches were suggested to deal with this problem [26, 42]. A constant nonresonance contribution of 4×10^5 MeV b was introduced to fit the data from direct measurements by [26], while the α- and neutron-widths for the 7.201 MeV $3/2^+$ state were adjusted to fit the experimental data at lowest energies by assuming there is no nonresonant contribution by [42], resulting in $\Gamma_\alpha = 0.09$ keV and $\Gamma_n = 400$ keV which slightly differ from the recommended values ($\Gamma_\alpha = 0.07$ keV, $\Gamma_n = 280$ keV) of [46]. In this work, we tested these two methods and found that both of them well reproduced the data below 0.8 MeV but the first way better reproduced the ones between 0.8 to 1.0 MeV. Thus, we adopted the first method to calculate total S-factors for the ^{13}C(α,n)^{16}O reaction, as shown with solid curve in Fig. 3. At Gamow peak ($E_{\rm c.m.} = 0.19$ MeV), the contribution of the $1/2^+$ subthreshold resonance to the total S-factor is dominant ($\approx 63\%$).

The astrophysical ^{13}C(α,n)^{16}O reaction rates were calculated with the present S-factors,

$$N_A\langle\sigma v\rangle = N_A(\frac{8}{\pi\mu})^{1/2}\frac{1}{(kT)^{3/2}}$$
$$\int_0^\infty S(E)\exp\left[-(\frac{E_G}{E})^{1/2} - \frac{E}{kT}\right]dE, \quad (7)$$

where N_A is Avogadro's number.

The total reaction rates were then derived and fitted as

$$\begin{aligned}
N_A\langle\sigma v\rangle = {} & \exp[13.5818 - 0.245402T_9^{-1} - 8.02471T_9^{-1/3} + \\
& 13.2152T_9^{1/3} - 15.3415T_9 + 2.15301T_9^{5/3} \\
& + 13.5332\ln(T_9)] + \exp[26.2574 - 0.251350T_9^{-1} \\
& - 20.7058T_9^{-1/3} + 0.836440T_9^{1/3} - 3.04077T_9 \\
& + 0.449386T_9^{5/3} + 4.36433\ln(T_9)].
\end{aligned} \quad (8)$$

The fitting errors are less than 7% in a range from $T_9 = 0.04$ to $T_9 = 1$. This function also behaves reasonably over a wider range from $T_9 = 0.01$ to $T_9 = 10$.

In Figure 4 we compare the present rate with the previous compilations [8, 13, 1] and the other available rates [32, 26, 42, 21]. In Figure 5 we also compare the present rate with the previous results at a temperature of 10^8 K. There is a large discrepancy of up to a factor of 3 at $T_9 = 0.1$ between the present rates and CF88's, Kubono's and Johnson's rates since either the contribution of the $1/2^+$ subthreshold resonance has not been taken into account [8], or the smaller contributions were found by [32] and [26]. In addition, our rate agrees with Denker95 compilation within 10% but about two times smaller than NACRE's compilation, and it is noted that these two compilations were both derived from an extrapolation of the experimental data of [15]. Our rate is consistent with the ones [42] where a similar contribution of the subthreshold resonance was found, and is in good agreement with the result of [21] where a multichannel R-matrix analysis was used to constrain the possible contribution from subthreshold resonances by taking into account all open reaction channels for the ^{13}C + α and ^{16}O + n systems.
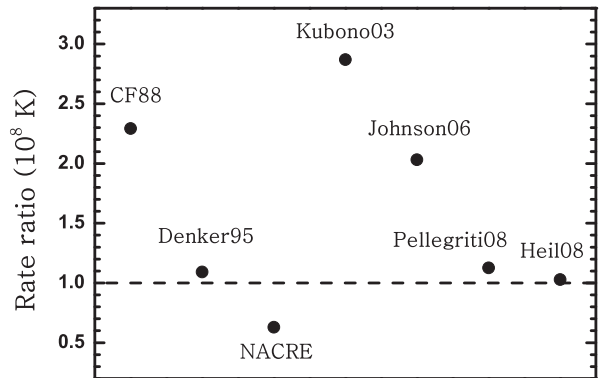

Figure 5: The ratios of the present rate to the previous compilations and the other available rates at a temperature of 10^8 K.
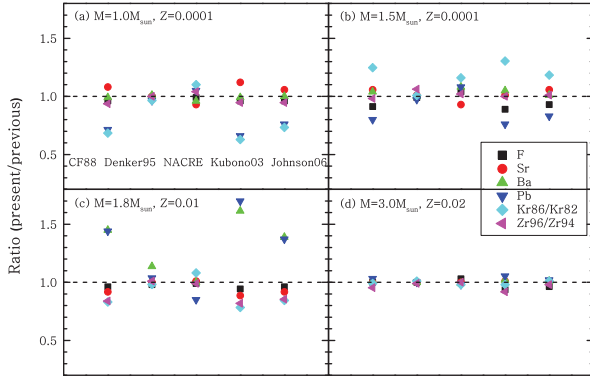
Figure 6: Effect of the different choices of the $^{13}C(\alpha,n)^{16}O$ reaction rate on the s-process nucleosynthesis in AGB stars. Panels (a)-(d) respectively show the results for the models of $M =1.0M_\odot$, $M =1.5M_\odot$, $M =1.8M_\odot$, and $M =3.0M_\odot$. In a panel, the five groups of symbol from left to right correspond to the results using the rates of CF88, Denker95, NACRE, Kubono03, and Johnson06. The Pellegritti08 and Heil08 results agree with those with the present rate within 10% for all the models, and thus are not plotted here. (A color version of this figure is available in the online journal.)

4 Astrophysical implication to s-process nucleosynthesis in AGB stars

We used a post-processing code where a nuclear network of 320 species (from H to Bi) and 2,336 reactions is solved simultaneously with mixing within the star when convective regions are present, and used stellar structure inputs, such as temperature, density, and convective velocity, calculated previously by the Stromlo stellar structure code [35] and including mass loss on the AGB phase using the prescription of [47]. We included the formation of the ^{13}C pocket by artificially allowing a proton profile to form just below the base of the convective envelope at the end of each TDU episode over a mass of 0.002 $M_\odot$ (roughly 1/10th of the mass of the He intershell). The details of this procedure and the codes used to compute the models have been described previously [39, 28].

We considered four models: a $M =3M_\odot$ model of metallicity $Z =0.02$ similar to the one discussed by [37], a $M =1.8M_\odot$ model of $Z =0.01$ [29], and $M =1M_\odot$ and $M =1.5M_\odot$ models of $Z =0.0001$ [41]. We chose these models for three reasons. (1) Models of higher masses probably do not experience the ^{13}C neutron source as protons will burn while being ingested in the intershell, preventing the formation of the ^{13}C pocket [19]. It is still not clear what the effect of this burning is on the whole stellar structure and the s-process, but it seems reasonable to us for the time being to not include a ^{13}C pocket for masses larger than $\sim 4M_\odot$. In these massive AGB stars, the temperature in the TPs exceeds 300 MK so that the $^{22}Ne(\alpha,n)^{25}Mg$ reaction is acti-

vated and likely plays the role of the main neutron source. (2) The ^{13}C in the pocket normally burns before the onset of the following TP, however, in some cases the temperature may not be high enough for this to happen and ^{13}C could be left over to burn in the following TP [11]. In our models, the ^{13}C pocket is ingested in the following TP while the abundance of ^{13}C is still higher than 10^{-4} for the first five ^{13}C pockets in the $M =1.8M_\odot$ model, for the first three ^{13}C pockets in the $M =1.5M_\odot$ model, and for both the two ^{13}C pockets included in the $M =1M_\odot$ model. These models are thus qualitatively different from the $M =3M_\odot$ model where ^{13}C always burns before the onset of the next TP. (3) In low-mass and low-metallicity stars (such as our $1M_\odot$ and $1.5M_\odot$ $Z=0.0001$ models), proton-ingestion episodes occur in the first few TPs during which protons are ingested directly inside the TPs and thus some extra ^{13}C is produced and burnt inside these convective regions.

Table 2: Abundance of the selected s-process elements and the isotopic ratios at stellar surface at the end of the evolution obtained from our $M =1.0M_\odot$ model when using the present $^{13}C(\alpha,n)^{16}O$ rate, together with the comparison using other available rates. The sign of (%) denotes the percent of variations respect to the present result.

Work	F	Sr	Ba	Pb	$^{86}Kr/^{82}Kr$	$^{96}Zr/^{94}Zr$
Present	5.07×10^{-9}	5.30×10^{-11}	9.01×10^{-11}	1.29×10^{-10}	23.5	0.838
CF88 (%)	4	-8	1	40	46	7
Denker95 (%)	1	0	-1	4	4	0
NACRE (%)	1	8	4	-5	-9	-4
Kubono03 (%)	4	-11	1	51	59	6
Johnson06 (%)	4	-5	0	31	36	6
Pellegriti08 (%)	0	-1	0	1	2	0

Table 3: Same as Table 2, but for the $M =1.5M_\odot$ model.

Work	F	Sr	Ba	Pb	$^{86}Kr/^{82}Kr$	$^{96}Zr/^{94}Zr$
Present	1.27×10^{-7}	1.66×10^{-10}	1.97×10^{-10}	6.95×10^{-10}	19.9	0.377
CF88 (%)	10	-5	-4	25	-20	2
Denker95 (%)	1	-1	0	3	-1	-6
NACRE (%)	-4	8	-7	-7	-14	-2
Kubono03 (%)	13	-1	-5	31	-23	0
Johnson06 (%)	8	-5	-1	20	-16	-1
Pellegriti08 (%)	2	-2	0	3	-2	-5

In Tables 2 to 5, we list the numerical results on the abundance of the selected s-process elements and the isotopic ratios at stellar surface at the end of the evolution obtained from our models using the present $^{13}C(\alpha,n)^{16}O$ rate, together with the percent of variations respect to the present result when using other available rates. In Fig. 6 we also display the variations of these results by plotting a ratio of the present one to others. The Pellegritti08 and Heil08 results agree with the results of the present rate within 10% for all the models, and thus are not presented in the figure. We chose to plot the elements representing the first s-process peak (Sr), the second s-process peak (Ba), and the third s-process peak (Pb). These provide a description of the overall s-process distribution, which is a function of the total time-integrated neutron flux, and they can be observed in stars. We further plot two isotopic ratios: $^{96}Zr/^{94}Zr$ and $^{86}Kr/^{82}Kr$. These are sensitive to the activation of the branching points at ^{85}Kr and ^{95}Zr, respectively, and thus to the local value of the neutron density.

These ratios can be measured in meteoritic stardust silicon carbide (SiC) grains that originated in AGB stars. We also report on the production of fluorine, however, we find that its production is not significantly sensitive (by $\simeq$10% at most) to the choice of the $^{13}C(\alpha,n)^{16}O$ reaction [39].

In the $M =3M_\odot$ model we do not find any variations in the resulting abundances within 10%. This is because in this model ^{13}C always burns before the onset of the next TP. The total integrated neutron flux is thus determined only by the initial amount of ^{13}C in the pocket and not by how fast it burns. We expect the same behavior for more massive AGB model if a ^{13}C pocket was to be considered in these cases. The isotopic ratios in this model are also not sensitive to the $^{13}C(\alpha,n)^{16}O$ rate as they depend mainly on the neutrons released in the TPs when the ^{22}Ne neutron source is marginally activated.

Table 4: Same as Table 2, but for the $M =1.8M_\odot$ model.

Work	F	Sr	Ba	Pb	$^{86}Kr/^{82}Kr$	$^{96}Zr/^{94}Zr$
Present	5.09×10^{-8}	4.39×10^{-9}	1.96×10^{-9}	4.28×10^{-10}	1.30	0.0505
CF88 (%)	4	9	-31	-31	20	19
Denker95 (%)	2	0	-12	-4	2	-1
NACRE (%)	1	-1	0	18	-7	1
Kubono03 (%)	6	13	-38	-41	28	22
Johnson06 (%)	4	9	-28	-27	19	17
Pellegriti08 (%)	0	-1	-6	6	0	3

Table 5: Same as Table 2, but for the $M =3.0M_\odot$ model.

Work	F	Sr	Ba	Pb	$^{86}Kr/^{82}Kr$	$^{96}Zr/^{94}Zr$
Present	1.12×10^{-7}	1.39×10^{-8}	1.76×10^{-9}	4.93×10^{-10}	0.409	0.0165
CF88 (%)	0	0	-1	-3	1	5
Denker95 (%)	0	0	0	0	-1	1
NACRE (%)	-3	0	1	2	2	0
Kubono03 (%)	7	-1	-2	-5	2	9
Johnson06 (%)	4	-1	-1	-2	-1	2
Pellegriti08 (%)	0	-1	-1	-1	-1	2

For the $M =1.8M_\odot$ model we find that the overall *s*-process distribution changes when different $^{13}C(\alpha,n)^{16}O$ rates are used. With rates slower than the present rate (such as CF88, Kubono03, and Johnson06) more Sr and less Ba and Pb are produced. On the other hand, using the NACRE rate, which is faster than the present rate, results in a higher abundance of Pb. These behaviors are related to the efficiency of the *s*-process because a lower efficiency produces less Ba and Pb than Sr, since for the neutron-capture flux to reach Ba and Pb higher number of neutrons per Fe seed are required. Slower rates result in more ^{13}C in the pocket left to be engulfed in the following TPs. The *s*-process with ^{13}C engulfed in the TP is less efficient than with ^{13}C burning radiatively for two reasons: (i) In the radiative ^{13}C pocket there is no mixing among the different layers of the pocket and thus ^{14}N nuclei do not mix with ^{13}C nuclei. This produces the highest *s*-process efficiency because ^{14}N is a neutron poison via the $^{14}N(n,p)^{14}C$ reaction, which removes neutrons from being captured by Fe seeds and their progeny. In the convective TP instead ^{13}C nuclei are mixed with the ^{14}N present in the pocket as well as in the H-burning ashes. (ii) The neutrons in the radiative ^{13}C pocket are released over a very small mass ($0.002M_\odot$ in our models), and thus there are more neutrons present per initial Fe seed and the flux of

neutron captures can reach to the heaviest elements up to Pb. In the convective TP instead the neutrons are released over a large mass ($\sim$ 0.01-0.02$M_\odot$ in our models) and thus there are less neutrons per Fe seed resulting in the production of the lighter *s*-process elements like Sr. The plotted isotopic ratios behave in the opposite way of Pb because the local neutron density is higher, and thus branching points are more activated, when ^{13}C is ingested in the TPs due to the higher temperature and thus the shorter burning timescale.

Interestingly, the low-metallicity $Z = 0.0001$ models present the opposite result to the $Z = 0.01$ model. In these stellar models a much larger fraction of ^{13}C burns while ingested in the TP, together with ^{14}N, due to incomplete burning of the ^{13}C pocket before the next TP as well as to the proton-ingestion episodes. As mentioned above, ^{14}N acts a neutron poison via the (n,p) channel, but at the same time it is also destroyed by α captures in the TP. Hence, the timescale of ^{13}C ingestion and burning with respect to the timescale of ^{14}N ingestion and burning has an impact on the final neutron flux and thus on the heavy element abundances. Slower $^{13}C(\alpha,n)^{16}O$ rates produce more free neutrons since if neutrons are released at later times there is less ^{14}N to capture them. In these conditions, one should also consider the effect of recycling of the protons made by the $^{14}N(n,p)^{14}C$ reaction. These protons can be captured by the abundant ^{12}C to make more ^{13}C, but also by ^{13}C itself. It is difficult to evaluate analytically the final outcome of all these combined effects. Our numerical models, which solve simultaneously mixing and nuclear burning, indicate that a slower rate results in a higher overall neutron flux (up to 50% more Pb) as well as a higher neutron density (up to 60% higher $^{86}Kr/^{82}Kr$ ratio) when considering low-metallicity low-mass AGB stars.

5 Discussion

It is interesting to compare the results of our models with the observations. There are significant differences up to 60% ($\sim$0.2 dex), which are produced in *s*-process abundances and ratios, by varying the ^{13}C burning rates. However, the main problem is that spectroscopic abundances in *s*-process-enhanced stars are currently determined with typical uncertainties around 80%, and thus larger than the differences found here. The other problem is that the formation of the ^{13}C pocket itself is very uncertain and there is no agreement on exactly which mechanisms drive it, and on the impact of processes such as rotation and magnetic fields. Also the details of the proton-ingestion episodes found in our low-metallicity models depend on the treatment of convective borders in stars, one of the largest uncertainty in stellar modeling. Hence, the future observations with high resolution and high signal to noise ratio spectra of low-metallicity stars, and the accurate gf values, and further understanding of the formation of the ^{13}C pocket and the proton-ingestion episodes are important for constraining the yield of *s*-process elements.

The situation is much better for the isotopic ratios, such as ^{96}Zr/^{94}Zr and ^{86}Kr/^{82}Kr. In the case of ^{96}Zr/^{94}Zr, the ratios can be determined from both meteoritic stardust SiC grains and S-type stars. The data of ^{96}Zr/^{94}Zr from meteoritic grains and S-type stars are much more precise with uncertainties as low as 5%-10% [38, 34]. Isotopic ratios affected by branching points may be indicative of the rate of ^{13}C burning, even though also in this case, the other uncertainties including the neutron-capture cross section of the unstable nucleus at the branching point may have a more important effect. The differences about 20% found here do not change significantly the interpretation of the data, which mostly indicate strong deficits in ^{96}Zr, with respect to solar, and are typically matched by AGB models [38].

In the case of ^{86}Kr/^{82}Kr, stardust SiC data range from $\sim$0.5 to 2 of the solar ratio of 1.52, and stardust high-density graphite reaches ^{86}Kr/^{82}Kr $\simeq$3 of the solar ratio, the value is increasing with the grain size. Our AGB models of metallicity around solar (Z = 0.01, 0.02), which are believed to well represent the parent stars of this stardust, only produce ^{86}Kr/^{82}Kr ratios lower than solar. However, [48] showed that the ^{86}Kr atoms are probably implanted in SiC by the high-velocity winds experienced during the evolution that follows the AGB, the post-AGB and the planetary nebula nucleus phases. Hence, the effect of the ^{13}C(α,n)^{16}O reaction rate needs to be evaluated with regards to the composition of Kr in the deep stellar layers that are exposed to the surface during these final phases of the evolution. In this context the possibility of a proton ingestion in the very late TP occurring during the post-AGB evolution also has to be taken into account. First simulations of this proton-ingestion event by [23] have shown that the rate of ^{13}C(α,n)^{16}O reaction plays a main role in determining the final abundances (see their Fig. 12). These models needs to be further investigated in relation to the ^{13}C(α,n)^{16}O reaction and its uncertainties, and the ^{86}Kr/^{82}Kr ratios in SiC grains.

6　Summary and conclusion

In summary, we have determined the contribution of the 6.356 MeV 1/2$^+$ subthreshold resonance in the ^{13}C(α,n)^{16}O reaction and then evaluated its rate, based on the measurement of α partial width for the 1/2$^+$ state of ^{17}O through the angular distribution of α transfer reaction ^{13}C(^{11}B,^{7}Li)^{17}O. Our result supports the conclusion that this resonance dominates the ^{13}C(α,n)^{16}O reaction within Gamow window at the typical temperature of 10^8 K in AGB stars. The present rate is used as input for the simulation of AGB star by considering four models, to study its influence on the abundance of selected s-process elements and isotopic ratios through the comparison with those using the other available rates. The significant differences of up to 60%, which are produced in s-process abundances and ratios, were found by varying the ^{13}C burning rate.

References

[1]. Angulo, C., Arnould, M., Rayet, M. et al. 1999, nphysa, 656, 3

[2]. Aoki, W., Norris, J. E., Ryan, S. G., Beers, T. C., Ando, H. 2000, apjl, 536, 97

[3]. Bair, J., & Haas, F. 1973, prc, 7, 1356

[4]. Burbidge, E. M., Burbidge, G. R., Fowler, W. A., Hoyle, F. 1957, Rev. Mod. Phys., 29, 547

[5]. Busso, M., Gallino, R., Wasserburg G. J. 1999, araa, 37, 239

[6]. Busso, M. et al. 2001, apj, 557, 802

[7]. Brune, C. R., Licot, I., Kavanagh, R. W. 1993, prc, 48, 3119

[8]. Caughlan, G., Fowler, W. 1988, At. Data Nucl. Data Tables, 40, 291

[9]. Cook, J., Stephens, M. N., Kemper, K. W. 1987, nphysa, 466, 168

[10]. Costantini, H., Formicola, A., Imbriani, G. et al. 2009, Rep. Prog. Phys., 72, 086301

[11]. Cristallo, S. et al. 2009, apj, 696, 797

[12]. Davids, C. N. 1968, nphysa, 110, 619

[13]. Denker, A. et al. 1995, in Proc. Int. Symp. Nucl. Astrophys., Nuclei in the Cosmos III, 327, 255

[14]. Descouvemont, P. 1987, prc, 36, 2206

[15]. Drotleff, H. W., Denker, A., Knee, H., Soine, M., Wolf, G., Hammer, J. W., Greife, U., Rolfs, C., Trautvetter, H. P. 1993, apj, 414, 735

[16]. Gallino, R., Busso, M., Picchio, G., Raiteri, C. M., Renzini, A. 1988, apjl, 334, 45

[17]. Gallino, R., Arlandini, C., Busso, M., Lugaro, M., Travaglio, C., Straniero, O., Chieffi, A., Limongi, M. 1998, apj, 497, 388

[18]. Goriely, S., Mowlavi, N. 2000, aap, 362, 599

[19]. Goriely, S., Siess, L. 2004, aap, 421, L25

[20]. Harissopulos, S., Becker, H. W., Hammer, J. W., Lagoyannis, A., Rolfs, C., Strieder, F. 2005, prc, 72, 062801

[21]. Heil, M., Detwiler, R., Azuma, R. E., Couture, A., Daly, J., Görres, J., Käppeler, F., Reifarth, R., Tischhauser, P. 2008, prc, 78, 025803

[22]. Herwig, F. 2005, araa, 43, 435

[23]. Herwig, F. 2011, apj, 727, 89

[24]. Hollowell, D., Iben, I., Jr. 1988, apjl, 333, 25

[25]. Iliadis, C. 2007, Nuclear Physics of Stars (Weinheim: WILEY-VCH Verlag GmbH Co. KGaA)

[26]. Johnson, E. D., Rogachev, G. V., Mukhamedzhanov, A. M., Baby, L. T., Brown, S., Cluff, W. T., Crisp, A. M., Diffenderfer, E., Goldberg, V. Z., Green, B. W., Hinners, T., Hoffman, C. R., Kemper, K. W., Momotyuk, O., Peplowski, P., Pipidis, A., Reynolds, R., Roeder, B. T. 2006, prl, 97, 192701

[27]. Käppeler, F., Gallino, R., Busso, M., Picchio, G., Raiteri, C. M. 1990, apj, 354, 630

[28]. Karakas, A. I. et al. 2009, apj, 690, 1130

[29]. Karakas, A. I. et al. 2010, apj, 713, 374

[30]. Keeley, N., Kemper, K. W., Khoa, Dao T. 2003, nphysa, 726, 159

[31]. Kellogg, S., Vogelaar, R., Kavanagh, R. 1989, Bull. Am. Phys. Soc., 34, 1192

[32]. Kubono, S., Abe, K., Kato, S., Teranishi, T., Kurokawa, M., Liu, X., Imai, N., Kumagai, K., Strasser, P., Tanaka, M. H., Fuchi, Y., Lee, C. S., Kwon, Y. K., Lee, L., Ha, J. H., Kim, Y. K. 2003, prl, 90, 062501

[33]. Kurath, D. 1973, prc, 7, 1390

[34]. Lambert, D. L. 1995, apj, 450, 302

[35]. Lattanzio, J. C. 1986, apj, 311, 708

[36]. Liatard, E., Bruandet, J. F., Glasser, F. et al. 1990, Europhys. Lett., 13, 401

[37]. Lugaro, M. et al. 2003, apj, 586, 1305

[38]. Lugaro, M. et al. 2003, apj, 593, 486

[39]. Lugaro, M. et al. 2004, apj, 615, 934

[40]. Lugaro, M., Raai, M. 2008, J. Phys. G, 35, 014007

[41]. Lugaro, M. et al. 2011, in preparation

[42]. Pellegriti, M. G., Hammache, F., Roussel, P. et al. 2008, prc, 77, 042801

[43]. Rudchik, A. A., Rudchik, A. T., Kozeratska, G. M. et al. 2005, prc, 72, 034608

[44]. Sekharan, K. K., Divatia, A. S., Metha, M. K., Kerekatte, S. S., Nambiar, K. B. 1967, Phys. Rev., 156, 1187

[45]. Thompson, I. J. 1988, Comput. Phys. Rep., 7, 167

[46]. Tilley, D. R., Weller, H. R., Cheves, C. M. 1993, nphysa, 565, 1

[47]. Vassiliadis, E., Wood, P. R. 1993, apj, 413, 641

[48]. Verchovsky, A. B. 2004, apj, 607, 611

Nuclear Physics Department
China Institute of Atomic Energy